Numerical Modeling of Extreme Flow Impacts on Structures

Nora Asadollahi Shahbaboli

Thesis submitted to the
Faculty of Graduate and Postdoctoral Studies
in partial fulfillment of the requirements for the degree of

Master of Applied Science in Civil Engineering

Department of Civil Engineering
Faculty of Engineering
University of Ottawa, Canada

August 2016

© Nora Asadollahi Shahbaboli, Ottawa, Canada 2016

Abstract

Recent tsunami disasters caused devastating damages to well-engineered coastal infrastructures. In fact, the current design guidelines are not able to provide realistic estimations of tsunami loads in order to design structures to withstand tsunamis. Tsunami hydrodynamic forces are estimated using the drag coefficient. This coefficient is traditionally calculated based on a steady flow analogy. However, tsunami bores behave like unsteady flows. The present work aims at investigating the tsunami forces for different structure geometries to provide realistic guidelines to estimate drag coefficients considering unsteady flows. In the present paper, the dam-break approach is used to investigate the tsunami-like bore interaction with structures. A three-dimensional multiphase numerical model is implemented to study the tsunami induced forces on rectangular shape structures with various aspect ratios (width/depth) and orientations. The numerical model results are validated using measured forces and bore surface elevations of the physical experiments. A scaled-up domain is modeled in order to eliminate the effects of domain sidewalls in the simulation results. The drag coefficient relations with structure geometries and bore depths are provided. The obtained hydrodynamic forces and drag coefficients are compared with existing data in the literature and design codes.

For the second topic, a multi-phase three-dimensional numerical reproduction of a large scale laboratory experiment of tsunami-like bores interaction with a surface-piercing circular column is presented. The numerical simulation is conducted in OpenFOAM. The dam-break mechanism is implemented in order to generate tsunami-like bores. The numerical model is validated using the experimental results performed at Canadian Hydraulics Center of the National Research Council (NRC-CHC) in Ottawa. The unsteady Reynolds Averaged Navier-Stokes equations (RANS) are used in order to treat the turbulence effects. The Shear Stress Transport (SST) k-ω turbulence model showed high level of accuracy in replication of the bore-structure interaction. Further, a scaled-up domain is used to investigate the influence of the bed condition in terms of various downstream depths and roughness. Finally, a broad investigation on the bore propagation characteristics is performed. The resulting stream-wise forces exerted on the structural column as well as the bore velocity are compared and analyzed for smooth, rough, dry and wet beds with varying depths.

Preface

This thesis is an integrated, manuscript-based thesis as defined Thesis Preparation, Examination Procedures and Regulations of the University of Ottawa. It consists of the following peer-reviewed journal articles (submitted):

1. Asadollahi, N., Nistor, I., Mohammadian, M., 2016, "Numerical Investigation of Tsunami Bore on Drag Coefficient of structures using OpenFOAM", submitted.

2. Asadollahi, N., Nistor, I., Mohammadian, M., 2016, "Numerical modeling of circular structures impacted by Tsunami forces and the effects of bed condition using OpenFOAM", submitted.

The body of this thesis consists of Chapters 3 and 4, in which the above-listed papers are reproduced.

Acknowledgment

I would like to express my appreciation to my supervisors, Dr. Ioan Nistor and Dr. Majid Mohammadian, for their supports during my master's studies. Their kind help and consultation paved the jagged research path for me and shed light on the dark and obscure research areas which led to real meaningful academic and industrial contributions. In my opinion, the bed rock of any master's thesis is casted in the first days when the thesis topic is going to be defined by a supervisor. Their deep knowledge about technology boundaries, which led to their wise choice of my master's thesis topic, was the most important component in my studies. In addition, his constant feedbacks and suggestions about every step in my thesis helped me to compensate myself to be on the right path.

Finally, I am a debtor to my family who always provide me with their unconditional supports throughout my undergraduate and graduate studies. I would like to thank them for their patience and kindness.

Nora Asadollahi

24th June, 2016

Contents

List of Figures

List of Tables

List of Symbols

Latin characters

C	Wave front celerity (m/s)
C_α	Compression coefficient
Co	Courant number
C_d	Drag coefficient
C_R	Resistance coefficient
d	Distance (m)
$\boldsymbol{f}$	Darcy-Weisbach friction factor
$\boldsymbol{F}$	Momentum source term (kg/s)
Fr	Froude number
g	Acceleration of gravity
h_u	Impounded water depth of dam-break problem (m)
h_d	Downstream water depth of dam-break problem (m)
k	Turbulent kinetic energy (m^2/s^2)
KC	Keulegan–Carpenter number
$\boldsymbol{n}$	Unit vector normal to the surface
p	Pressure (Pa)
p^*	Pseudo-dynamic pressure (Pa)
R_{ij}	Reynolds stress (N/m^2)
Re	Reynolds number
Re_o	Object Reynolds number
Re_f	Flow Reynolds number
$\boldsymbol{S_f}$	Cell face surface normal vector (m^2)
t	Time (seconds)
U	Bore front velocity (m/s)
U	Velocity vector (m/s)

$\mathbf{U_c}$	Compression velocity vector (m/s)
X	Position vector (m)
x	X component of position vector $\boldsymbol{x}$ (m)
y	Y component of position vector $\boldsymbol{x}$ (m)
z	Z component of position vector $\boldsymbol{x}$ (m)

Greek letter symbols

α	Phase fraction
κ	Curvature (1/m)
ε	Turbulent dissipation (m^2/s)
μ	Dynamic viscosity (Ns/m^2)
μ_t	Turbulent dynamic viscosity (Ns/m^2)
$\mu_{\,eff}$	Effective dynamic viscosity (Ns/m^2)
ν_{turb}	Turbulent kinematic viscosity (m^2/s)
ν	Kinematic viscosity of laminar flow (m^2/s)
$\emptyset$	Generalized conservative physical quantity
ρ	Water density (kg/m^3)
ρ_s	Fluid density including sediment (kg/m^3)
τ	Viscosity stress tensor (N/m^2)
σ	Surface tension coefficient (N/m)
λ	Damping factor
ω	Specific turbulent dissipation (m^2/s)

Mathematical operators

∇	Gradient
∇_i	Gradient taken with respect to the coordinates of particle i
$\nabla\cdot$	Divergence
$\cdot$	Vector dot product
$\otimes$	Tensor product
$\lvert\ \rvert$	Absolute value
$\partial/\partial x$	Partial derivative with respect to a variable x

Abbreviations

AR	Aspect Ratio
BC	Boundary condition
BR	Blockage Ratio
CFD	Computational Fluid Dynamics
DOF	Degrees Of Freedom
FEMA	Federal Emergency Management Agency
FVM	Finite Volume Method
NSE	Navier-Stokes Equation
OpenFOAM	Open Field Operation And Manipulation
PDE	Partial Differential Equation
PT	Pressure Transducer
PVC	Polyvinyl Chloride
RANS	Reynolds-Averaged Navier-Stokes
RC	Reinforce Concrete
RMS	Root Mean Square
RMSE	Root Mean Square Error
SPH	Smoothed Particle Hydrodynamics
URANS	Unsteady Reynolds-Averaged Navier–Stokes
VOF	Volume Of Fluid
WCSPH	Weakly Compressible Smoothed Particle Hydrodynamics
WG	Wave Gauge

Chapter 1. Introduction

1.1. Background

Tsunamis are mostly generated in deep water by sudden vertical displacement of water triggered by submarine earthquakes. Other phenomena such as landslides, asteroid impacts and explosive volcanisms can also cause large tsunamis. The sudden seabed uplift in subduction zone transfers its energy to the column of water above it and changes the sea level locally. This generates tsunami waves propagating in all directions from its source. Tsunami can propagate in the deepest water at the speed of 970 km/hr, carrying massive amount of energy. Their wavelengths in deep water can reach several kilometers however; their amplitudes are usually less than a meter. As these waves reach shallow water areas, their velocities are reduced and their amplitudes are increased due to the shoaling effect. During this transformation, these waves still preserve their huge amount of energy which makes them one of the most destructive natural disasters.

Basically, when a long period tsunami wave propagating over a mild slope bathometry or sudden discontinuities in the seabed, it will break and transforms into a steep turbulent tsunami bore. The breaking wave will propagate toward inland in the form of turbulent hydraulic bore. As it can be seen in Figure 1.1, the highly turbulent tsunami bore-front, which contains large amount of debris, is advancing across the inland area during 2011 Tohoku tsunami. The 2011 Tohoku great Tsunami as well as 2004 Indian Ocean tsunami brought extensive fatal casualties and devastating damages on costal infrastructures. The Indian Tsunami was generated by Mw 9.3 subduction earthquake at the northern coasts of Indonesia caused over 220,000 fatalities (FEMA P-646, 2012). The 2011 Tohoku great Tsunami generated by Mw 9.0 subduction earthquake in northeast Japan, had occurred 130 km off the coast of Miyagi Prefecture (Mori et al., 2012). The coastal buildings, bridges, seawalls and break waters were destructed extensively and the death toll over 19,000 was reported (FEMA P-646, 2012). The economic loss was estimated over $217 B by the government of Japan (EERI, 2011). Most of these buildings were designed to withstand tsunami loadings.

Figure 1.1: Hydraulic bore sweeping across a residential area a mile from the bay front, Tohoku 2011 tsunami in Rikuzentakata, Iwate Prefecture, Japan. (Photo by local police from helicopter, www.extremeplanet.me)

Figure 1.2: Destruction of port infrastructures by the 2011 Tohoku Tsunami a) Failure of breakwater at Takenoura, Onagawa Town.(Mikami et al., 2012) b) Damage of wharf at Soma Port.(Mikami et al., 2012) c) Scour around the quay support sheet pile. (EERI, 2011)

Tsunami loads that should be considered for design of coastal structures consist of: hydrostatic force, hydrodynamic force, debris and debris damming impacts, scouring effects, buoyant and uplift forces.

Some evidences of damage due to hydrodynamic force and scouring effects on port infrastructures are depicted in Figure 1.2. During 2011 great Tohoku Japan tsunami, the light-frame buildings located in residential areas were almost collapsed and 75% to 95% of low-rise buildings were destroyed in industrial areas as shown in Figure 1.3 (EERI, 2011).

Figure 1.3: Extensive devastation of inland buildings during 2011 Tohoku Tsunami in Onagawa city, [Courtesy of Dr. I. Nistor].

Figure 1.4: Destruction of inland building due to tsunami-induced hydrodynamic forces and overturning moments (a) Steel-frame building [Courtesy of Chock] (b) Reinforced concrete building [Courtesy of Koshimura].2011 Tohoku Tsunami, Onagawa city, Miyagi prefecture, Japan

As shown in Figure 1.4, many buildings failures were subjected to the global stability failure. In this type of failure, either buoyancy and hydrodynamic forces or combinations of both may cause the

damage. The buildings were overtopped by high tsunami inundation depth and lifted due to buoyancy forces and overturned when exposed to large hydrodynamic forces.

Based on these evidences, the insufficient design considerations in the current building codes for designing coastal structures against tsunami loadings are brought into attention (Nistor et al., 2009). Moreover, major reasons of global failures of structures in 2011 Tohoku Japan tsunami was unprecedented inundation depth and high flow velocity (Yeh, 2013).

Yeh (2015) reported that most of current design formulas do not consider the buoyancy force caused by pore-water pressure at the foundation. According to FEMA P-646 (2012), available guidelines and standards are not directly focusing on tsunami-induced loads. Most of these guides were targeting storm surges and riverine flooding while these types of floods are completely different from tsunami bores. One significant difference is that higher flow velocities are associated with the tsunami bore. Due to these observations, the necessity of developing new design recommendations and revising current guidelines for tsunami loading is revealed. Since the occurrence of a tsunami is infrequent, the field survey seems impractical. Therefore, in order to improve and establish new design guidelines, more comprehensive research on tsunami-induced bores interactions with structures seems necessary using physical and numerical modeling.

1.2. Study Objectives

The current study is mainly focused on flow characterises and tsunami-induced loads during bore-structure interactions. This research work provides two major different objectives to investigate bore-structure interactions, which are presented as follows:

1.2.1. Drag coefficient of structures induced by tsunami-bores

- The efficiency of the numerical model is assessed quantitatively and qualitatively by replicating physical experiments of tsunami bore-structure interaction performed by Al-Faesly et al. (2012). The numerical model was based on a three-dimensional multi-phase volume of fluid method using OpenFOAM.
- A scaled-up domain is implemented in order to investigate how the sidewalls affect resulting tsunami-induced forces and other flow characteristics and eliminating these effects.
- The drag coefficient of the different geometrical structures and different structural orientations subject to tsunami-induced loads for closer to prototype scale is calculated.

- New values of drag coefficient for new establishing tsunami design guidelines are suggested.

1.2.2. Bore-structure interaction over different bed conditions

- The efficiency of the numerical model is assessed quantitatively and qualitatively by replicating physical experiments of tsunami bore-structure interaction performed by Nouri et al. (2010). The numerical model was based on a three-dimensional multi-phase volume of fluid method using OpenFOAM.
- A scaled-up domain is implemented in order to investigate how the sidewalls affect resulting tsunami-induced forces and other flow characteristics and eliminating these effects.
- Influences of the bed conditions on propagation characteristics and resulting tsunami-induced forces are investigated.

1.3. Scope

In the present study, the aforementioned physical experiments were first numerically reproduced in order to evaluate the capability of the numerical model. The large-scale experiments are concerned with the dam-break generated bore advancing the surface-piercing structure. This mechanism of the tsunami-like bore generation was performed by abrupt releasing of impounded water column into the channel with a structural column positioned further in the downstream. The numerical and physical results are compared which include: (i) time-histories of the net stream-wise force exerted on the structures, (ii) time-histories of pressure exerted on the upstream side of the column, (iii) temporal variation of water surface elevations for the different locations of the flume. The scaled-up domain is used in order to perform further investigations on the bore-structure interaction process.

In the case of tsunami-induced drag coefficient, the time history of drag coefficient of different aspect ratio's (column width to depth) of rectangular columns and walls are obtained. The influence of structural orientations is also considered. Finally, an average drag coefficient is suggested which depends on column geometry, flow depth and flow velocity.

In the case of bore-structure interactions over varying bed conditions, the presence of varying water depth and bottom roughness over the channel's downstream floor is investigated for circular columns with dam-break bore. The presence of various downstream to upstream water depths in channel have

a significant influence on bore propagation characteristics and values of the resulting impulsive and hydrodynamic forces.

1.4. Contributions

Since tsunamis are infrequently happening, the field survey is not feasible. However, the numerical modeling provides an important tool to investigate the nature of tsunamis in a feasible way. The numerical models are able to accurately simulate the real physical problems. There is not much information on the accurate values of some bore parameters (i.e. bore depth or velocity near structure) in the tsunami-related problems. This could be achieved by accurate numerical simulations using fine mesh resolutions (FEMA P-646, 2012). The investigation of the interaction of tsunami-like bores with surface-piercing structures has been brought into attention in the last decade. Some experimental investigation has been performed in this regards. One approach is the Smooth Particle Hydrodynamic (SPH) which has been widely used in the application of wave interaction with coastal structures. Many of these numerical studies were performed for single phase SPH model with the application of the tsunami-like bore interaction with structures. The other alternative is Reynolds-Averaged Navier–Stokes (RANS) equations. The RANS equations have been broadly used in modeling of the wave-structure interaction. These equations are accessible through open source and free codes for extensive fluid-structure interaction applications. Moreover, a two-phase numerical model which simulates the effects of air entrainment in the bore-structure interaction problems is used.

The novelty of the present study is the better understanding of the bore-structure interaction and predicting the resulting hydrodynamic forces by examining different structural geometries using the two-phase large scale numerical models. Further, associated drag coefficients of these structures subjected to tsunami-like bore are suggested. The recommended values of drag coefficients which are available in the literature are only limited to aerodynamic applications and steady flows around columns. However, the nature of the tsunami-induced bore is significantly different with the aforementioned flows. Moreover, although the large-scale experimental model is replicated numerically for the purpose of application, for further investigation on the hydrodynamic force and relevant drag coefficient, a scaled-up domain (close to the real prototype) is implemented here in order to obtain more realistic results of force ratio between the numerical model and prototype.

In addition, the effects of the bed conditions (i.e. dry or wet and roughness) on the propagation characteristics of tsunami-like bore and hydrodynamic forces exerted on the structures have been comprehensively investigated for higher downstream depth of the bed and different bottom friction. To the knowledge of the author, most of the available studies in this regard have not provided much information about tsunami induced hydrodynamic forces. The resulting hydrodynamic forces and water surface elevation variation are estimated using the same aforementioned scaled-up model. Finally, these findings can be used in establishing new design codes for tsunami loading or as a preliminary design recommendation.

1.5. Outline

Chapter 1 presents a brief introduction on the topics of the study as well as the objectives, motivations and novelty of the work. In chapter 2, an extensive literature review is provided on the realm of bore-structure interaction as well as drag coefficient of structures. In order to model the tsunami-like bores, different approaches are introduced. Furthermore, a number of numerical and experimental studies with respect to the impact of tsunami-like bore on structures are discussed. Afterwards, some relevant studies on the influence of bed conditions on tsunami bore characteristics are reviewed.

In chapters 3 and 4 the first and second papers are presented respectively. In the first paper, the drag coefficient of the structures subjected to the tsunami bore is investigated using a scaled-up numerical model. In the second paper, the impact of circular structures with the tsunami bores is investigated over varying bed conditions. The governing equations and numerical model approach is described in both papers. Moreover, the sensitivity analysis and further validation results of the numerical model using a large-scale experiment are also described. Lastly, the research conclusions and suggestions for future works are presented in chapter 5.

Chapter 2. Literature review

In this chapter, a brief review of the past studies on tsunami-like bore-structure interactions is presented. First, different methods to reproduce tsunami-like bores experimentally and numerically are introduced. Second, a background on studies related to drag coefficient of structures are presented. Next, some related experimental and numerical works dealing with bore-structure interaction mechanism are discussed. Finally, research works on the effects of bed conditions on bore propagation are described.

2.1. Experimental Modeling of Tsunami Bores and Dam-Break Waves

In order to model tsunami wave, different approaches have been employed experimentally. The solitary wave is a classical method to study the tsunami waves since they are capable of modeling important aspects of tsunami waves. Many studies have been implemented the solitary wave method in coastal processes. Synolakis (1987) performed a series of laboratory experiments to model the maximum run-up of solitary waves for non-breaking waves.

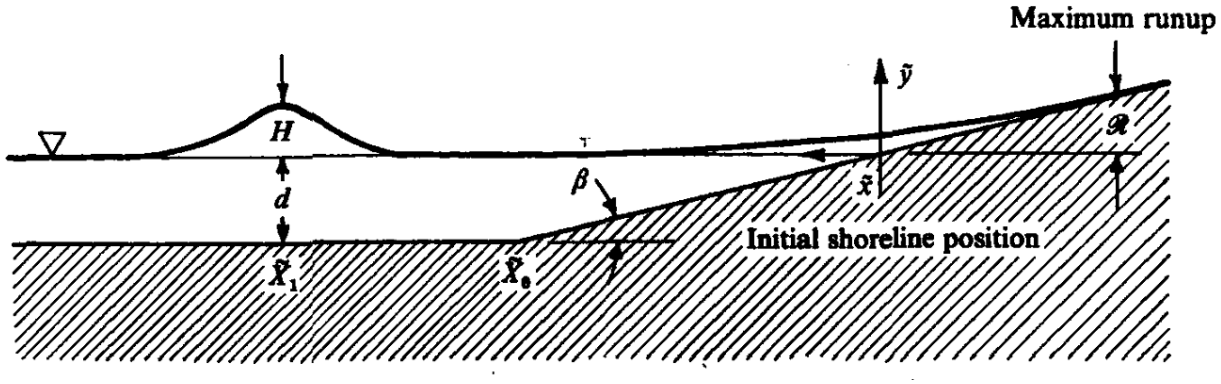

Figure 2.1: Definition sketch of a solitary wave approaching a sloping beach [Synolakis,(1987)]

The author derived the "Run-up law" which can predict the maximum run-up of a non-breaking solitary wave. The value of maximum run-up ($\mathcal{R}$) is defined as ,

$$\frac{\mathcal{R}}{d} = 2.831(\cot\beta)^{\frac{1}{2}}\left(\frac{H}{d}\right)^{\frac{5}{4}} \qquad (2\text{-}1)$$

The variables are shown in Figure 2.1. The assumption of $\left({}^{H}/_{d}\right)^{\frac{1}{2}} \gg 0.288tan\beta$ should be implied whilst using Eq.2-1. He also indicated that the maximum run-up value is varying for breaking and non-breaking solitary waves and "run-up law" is only giving accurate results for estimation of run-up values of non-breaking waves.

Briggs et al. (1995) performed large-scale laboratory experiments to analyze three-dimensional tsunami run-up. The authors aimed to verify and modify the numerical model using the experimental data. The experiments were conducted in a flat bottom basin (30m wide× 25m long ×0.6m deep) where a 7.2m diameter conidial shape island with 1 to 4 side slopes was located in its center. The generated solitary waves were ranged from 0.05 to 0.20 (height to depth). Figure 2.2 shows the general configuration of the experimental basin. The wave shoaling and refracting around the island is evident in this figure.

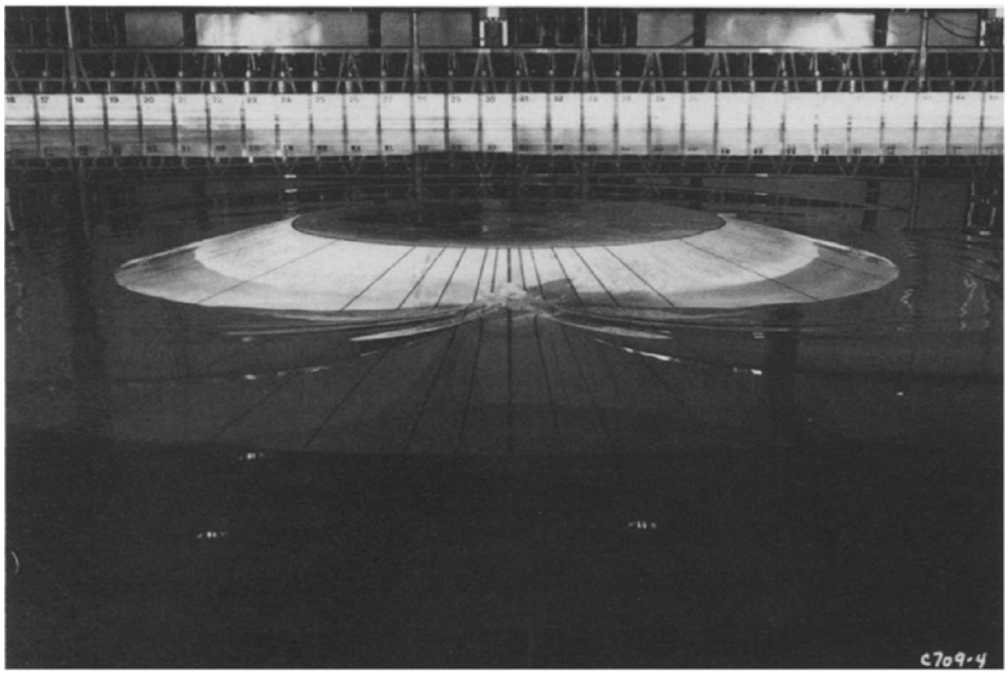

Figure 2.2: Run-up around island.[Briggs et al., 1995]

The authors observed a relatively uniform run-up configuration around the island. However, the symmetrical island and source configuration resulted in a larger run-up height at the back side of the island. This is caused by the waves were wrapped around the island due to diffraction and refraction. Liu et al. (1995) replicated their experimental work numerically using shallow water equations. They observed fairly similar run-up patterns. Many other experimental works were developed by Ramsden, (1993), Robertson et al., (2011), Linton et al., (2013) and etc. to investigate tsunami waves. However, Madsen et al. (2008) demonstrated that the solitary waves are not capable of replicating geophysical characteristics of real tsunamis. The authors argued that the transition of tsunami wave front into undular bore during shoaling impossible as there is not enough time and distance provided for them in the shallow water region. Based on their discussion, the distance required for real-world tsunami to evolve into solitary wave is exceeded from the width of any ocean basins.

Later, Madsen and Schäffer (2010) developed Synolakis (1987) work and suggested an analytical solution for run-up of general incident waves. Chan and Liu (2012) used free surface field records during Japan Tohoku tsunami and indicated that the leading edge of these waves differ from solitary wave. They observed that the leading tsunami wave is larger than solitary waves in a continental shelf. The observed wave period (T) by the field data is far more than the wave period obtained by the solitary wave (T=17min Vs. T=3min). The authors finally supported the statement mentioned by Madsen et al. (2008). They also found that the Madsen and Schäffer's (2010) aforementioned analytical solution gave a satisfactory approximation for leading tsunami waves.

Dam-break is another alternative to model tsunamis. A dam-break wave induces a hydraulic bore similar to the typical tsunami broken wave. This approach is based on suddenly releasing of the impounded water (h_u) into the channel downstream. In some cases the downstream of the channel may also contain a layer of water (h_d) as shown in Figure 2.3. Stoker (1957) proposed an analytical solution based on shallow water equations both the dry ($h_d = 0$) and wet ($h_d > 0$) bed conditions. The effects of turbulence and viscosity weren't considered in his analytical solution. Cross (1967) identified a relation between the tsunami surge and the dam-break wave. Afterwards, Ritter (1982) proposed a bore generation formulation using the dam-break approach in a wide frictionless channel by solving nonlinear shallow water equations. However, Ritter's (1982) was not considered the flow characteristics at the wave tip region. Due to similar characteristics of the dam-break wave with tsunami waves, this method has been widely used in the tsunami interaction with coastal structures.

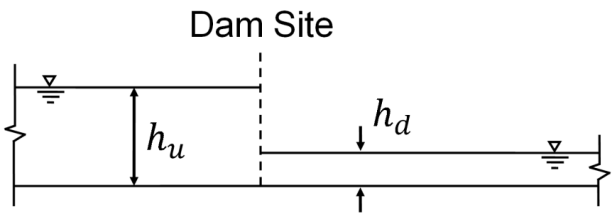

Figure 2.3: Schematic view of the dam-break wave generation. [St-Germain et al. 2012]

Chanson (2006) developed a theatrical model based on the analogy between tsunami bore and dam-break wave by analyzing the images of 2004 Indian ocean tsunami. The author finally demonstrated that the dam-break wave is similar to a broken tsunami wave intruding the inland areas (Figure 2.4). As shown in Figure 2.4, the leading wave tip is not similar to Ritter's theory. Based on experimental observations, the wave tip has rounded shape and the velocity of bore front (U) is less than the celerity of wave front ($C = 2\sqrt{gd_0}$) for an ideal flow due to bottom friction.

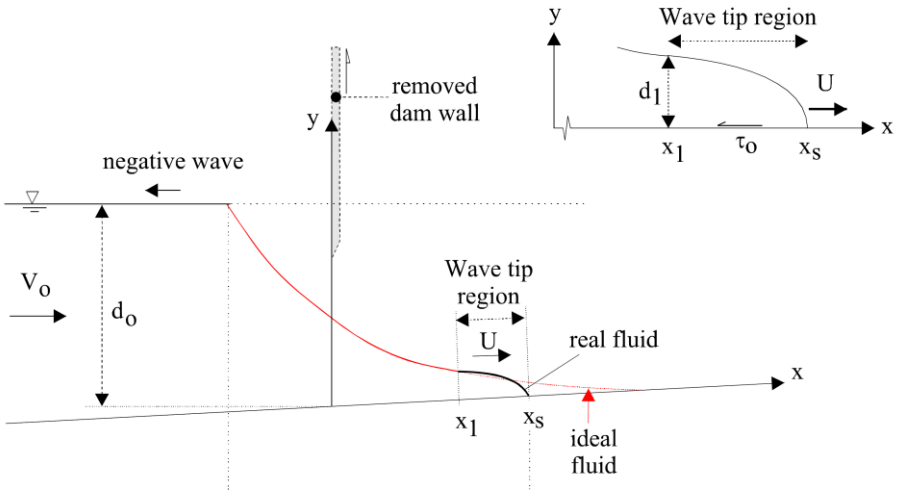

Figure 2.4: Definition sketch Dam break wave in a sloping channel [Chanson, 2006]

Later, Chanson (2009) developed an analytical solution to obtain free-surface profile equations of both frictionless or friction dominated bore-fronts for dam-break waves using shallow water equations (SWEs). The author validated the analytical results with experimental and theoretical models. The Darcy–Weisbach friction factor was assumed non-constant. The analytical solution gives expressions of wave front celerity, wave front location and free-surface profile.

2.2. Investigation of Drag coefficient of structures

2.2.1 Drag

In fluid mechanics, drag forces act on a solid in the direction of the relative fluid flow velocity. Drag is the component of force on a body acting parallel to the relative motion direction. The total drag force consists of the sum of friction drag and pressure drag. However, the drag coefficient is a function solely of the Reynolds number.

Pressure drag is created because of the form of the solid. This drag is a force caused by pressure differences across an obstacle in a flow field. For instance, in oceans, pressure drag takes place when currents flow over and around an object. The most important factors in pressure drag are the general size and shape of a solid; solids with a larger apparent cross-section have a higher drag than thinner solids. In the drag equation, the drag rises with the square of speed and pressure drag follows the drag equation, therefore, pressure drag is important for a high speed object. Friction drag is created by the friction of the fluid against the 'skin' of the object that is moving through the fluid. This drag force is because of the tangential forces which are created when a fluid flows over a surface. Hence, a rough surface gives more frictional drag. Friction drag also uses the drag equation and is increased by the square of the velocity (Fox et al., 2004).

2.2.2 Literature review on drag coefficient

Based on FEMA P-646 (2012), when water flows around a structure, hydrodynamic forces are employed to the structure as a whole and to individual structural elements. This force is a function of fluid density, flow velocity and structure geometry. It is also known as drag force. They are a combination of the lateral forces instigated by the pressure forces from the moving mass of water and the friction forces produced as the water flows around the structure or component. Hydrodynamic force (F_D) can be calculated as

$$F_D = \frac{1}{2} C_D \rho_s B h u^2, \quad (2\text{-}2)$$

where ρ_s, C_d, B, h and u are the fluid density including sediment, the drag coefficient, the breadth of the structure in the plane normal to the direction of flow (i.e. the breadth in the direction parallel to the shore), the flow depth and the flow velocity at the location of the structure, respectively. It is suggested that the drag coefficient should be taken as C_d= 2.0. The leading edge of a surge of water

impacting a structure brings about impulsive forces. Impulsive forces will affect members at the leading edge of the tsunami bore while hydrodynamic forces will have an effect on all members that have already been passed by the leading edge, as illustrated in Figure 2.5.

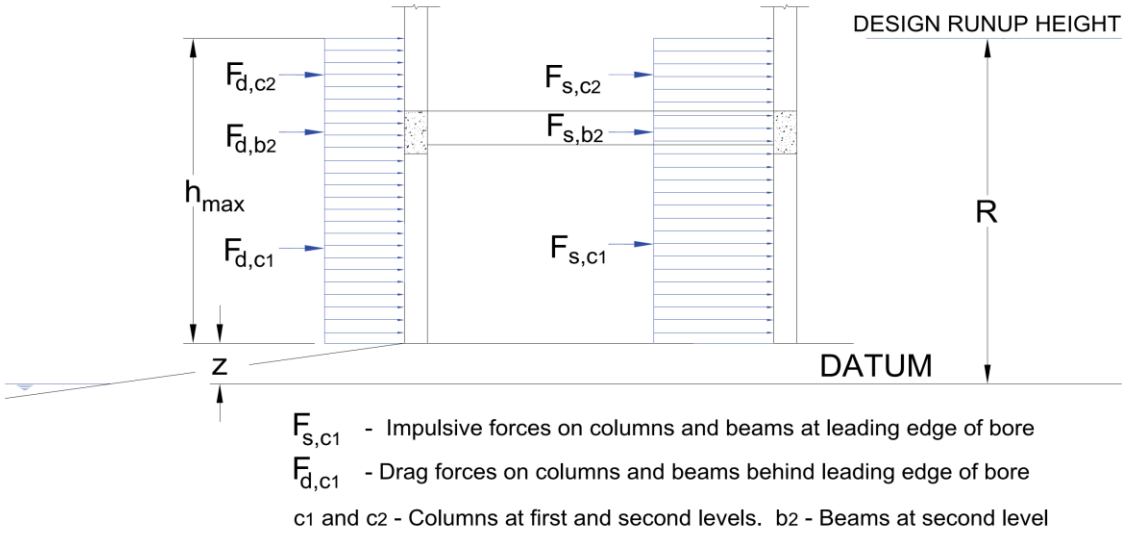

Figure 2.5: Impulsive and drag forces on components of a building subjected to inundation by a tsunami bore. [FEMA P-646,2012]

Generally, the tsunami force will not occur at the same time and on the same structural component. For example, as shown in Figure 2.6, the distribution of drag and impulsive on the structural compontents are presented in the plan view. In this case, the total horizontal hydrodynamic force on the structure is a combination of impulsive and drag force on the members at the leading edge of the bore and all other submerged members behind it, respectively.

One of the main contributing factors in the drag force is the drag coefficient. In the current design guidelines, recommended values for the drag coefficients are mostly obtained for the steady or unsteady flow in other applications such as flow around bluff bodies. Extensive experimental and numerical works have been carried out in the literature for high Reynolds turbulent flows.

Sohankar (2008) conducted numerical simulations using large eddy simulation (LES) to investigate the unsteady three-dimensional flow over rectangular cylinders with varying side ratios (R, defined as width to depth) ranging from R=0.4 to R=4 and Reynolds number $Re=10^5$.

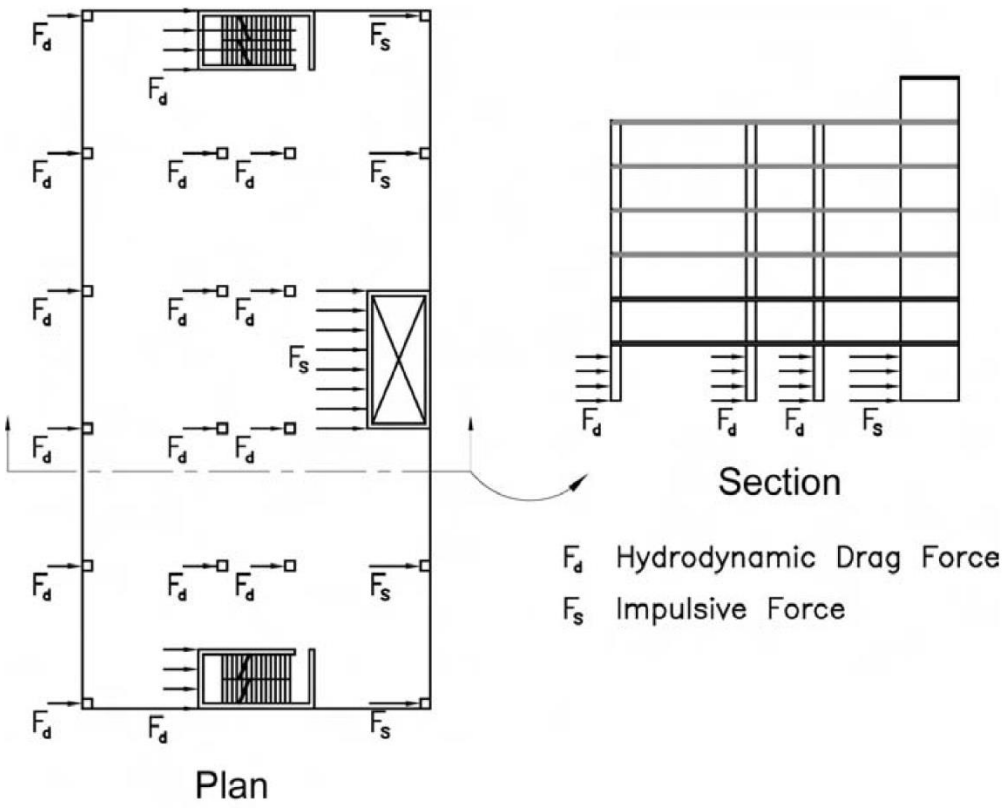

Figure 2.6: Impulsive and drag forces applied on an example building [FEMA P-646,2012].

Based on his study, a peak in the mean and Root Mean Square (RMS) base pressure and drag coefficients was occurred at R=0.62. Generally, a good agreement was obtained by comparing the resulting force coefficients with accessible experimental results. The effects of Reynolds number was found to be negligible as the side ratios and Reynolds numbers increased. Although, this effect was substantial for lower side ratio and lower Reynolds numbers.

In Vengatesan et al. (2000)'s experimental work, the in-line and transverse forces exerted on surface-piercing rectangular cylinder subjected regular and random waves were obtained in a towing tank with 2.2 m depth. Two different aspect ratios equals to 1:2 and 2:1 of the rectangular columns were considered for the study. At the lower Keulegan–Carpenter number (KC), large values drag coefficients were obtained and these coefficients decreases significantly as KC numbers increased for both examined aspect ratios of the column.

Bruno et al. (2010) studied the aerodynamic features of rectangular column with aspect ratio (defined as width to depth) equal to 5. The three-dimensional turbulent flow around the column was simulated using LES approach. The obtained drag coefficient in their study was consistent with other similar numerical data available in the literature obtained for the same aspect ratio (Figure 2.7).

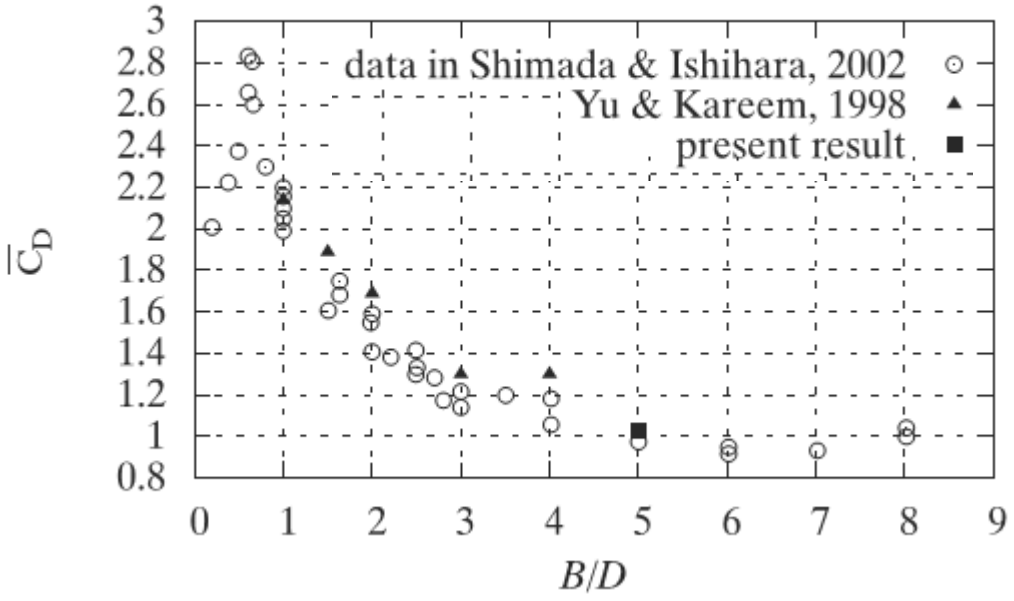

Figure 2.7 Comparison of mean drag coefficients with results from literature [Bruno et al., 2010]

In the case of free surface flows, Tian et al. (2013) investigated the unsteady flow around rectangular-section columns with varying aspect ratios (defined as width to depth) ranging from 0.05 to 1 using two-dimensional Unsteady Reynolds-Averaged Navier–Stokes (URANS) equations. The k–ω SST turbulence model was implemented. The authors observed that the variation of the aspect ratio had no effects on the vortex formation and the subsequent hydrodynamic force for the Reynolds number (Re) equal to 21400. They compared the resulting drag coefficients with the relevant published experimental results and numerical data and obtained a good level of agreement.

Yeh (2006) argued that the tsunami bores behave like unsteady flows rather than steady flow thereby different values of drag coefficient should be considered from them other than those suggested for steady flows or submerged bodies. Arnason (2005) conducted a series of laboratory experiment in order to investigate the drag coefficient of structures subjected to tsunami bore. The author noticed that the pressure difference between the upstream side and leeside of the structure contributes in the

hydrodynamic force for the free-surface gravity controlled flow. Therefore, he introduced the resistance coefficient (C_R) instead of drag coefficients (C_d). The author studied the structure-bore interaction of structures with different orientations, shapes and blockage ratios and measured the hydrodynamic forces and suggested the associated resistance coefficients. The author finally investigated the effects of several factors on the resistance coefficient includes structure shape, dimensions and orientation, flow Froude number (Fr), Reynolds number, the bore depth and blockage effects. The author examined different impounded water depths (h_u) ranging from 100 mm to 300 mm.

Further analysis showed that by increasing the impounded water depth, and subsequently bore depth, the drag coefficient decreases. The author calculated drag coefficients for two square columns with upstream side perpendicular (Figure 2.8 Left) and 45° rotated (Figure 2.8 Right) with respect to the flow direction. As shown in Figure 2.8, the time is normalized based on the propagation speed. The higher value of C_R can be observed during the initial spike (corresponding to the impulsive force) for the square column with the upstream side perpendicular to the flow direction, however, no spike is observed for the 45° rotated column.

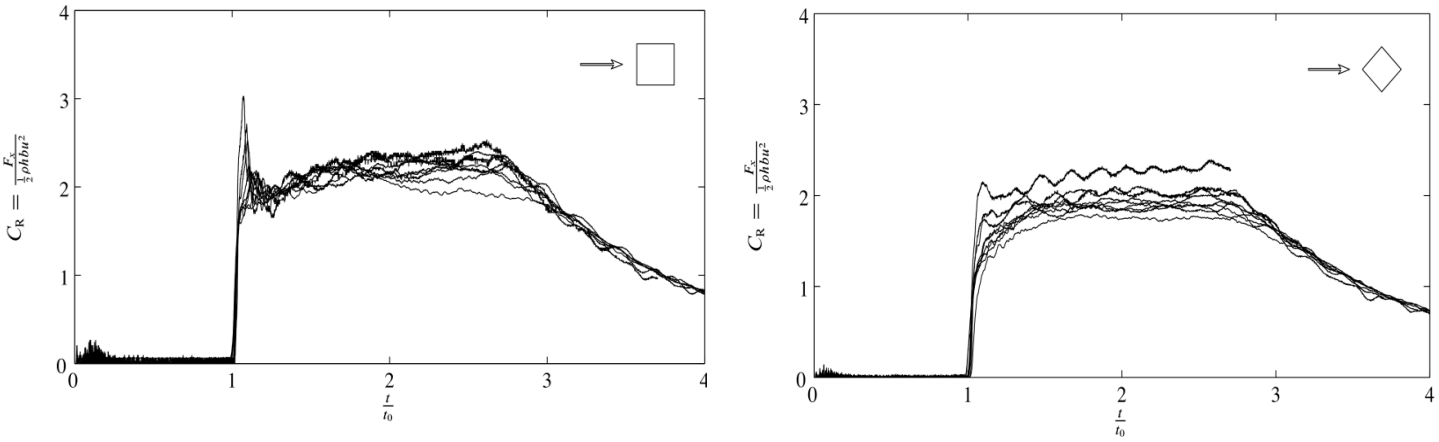

Figure 2.8: Time histories of resistance coefficient for the square column and the diagonally orientated square [Arnason ,2005]

The resistance coefficient during the quasi-steady phase varies between of 1.99 to 2.26 for the square column with the upstream side perpendicular to the flow direction and 1.72 to 2.22 for the 45° rotated square column. This confirms the value of C_d=2.0 stated by FEMA-P646 (2012) for the square column upstream side perpendicular to the flow direction.

Recently, Shafiei et al. (2016) carried out laboratory experiments in a 14 m long, 1.2 m wide and 0.8 m deep channel to study the hydrodynamic force and associated drag coefficients for square column with different orientations. Based on Cross's (1967) assumption, which states that the total stream-wise force is the summation of hydrodynamic and hydrostatic forces, the authors calculated the drag coefficients. The authors subtracted the hydrostatic force from the total measured stream-wise force and consequently the hydrodynamic force was obtained. Afterwards they calculated C_d values based on the obtained hydrodynamic forces. The C_d values were suggested as 1.65, 1.4 and 1.15 for 0°, 30° and 45° rotated squares, respectively, and recommended for preliminary designs.

2.3. Physical Modeling of Bore-Structure Interaction

Many experimental studies have been performed to investigate the tsunami-like bore interactions with free-standing structures. Based on Yeh's (2007) methodology, the maximum hydrodynamic force induced by tsunami loading can be estimated using the maximum momentum flux at any location for an unobstructed flow. Afterwards, FEMA P-646 (2012) adapted this approach for estimating the hydrodynamic force induced by tsunami wave. Lukkunaprasit et al. (2009) verified the aforementioned method employing laboratory experiments based on the field data and topography in Kamala Beach, Thailand during the 2004 Indian Ocean Tsunami. The authors claimed that FEMA P-646 approach provides fairly plausible prediction of the hydrodynamic force.

The laboratory experiment conducted by Ramsden (1993) at two separate wave tanks to study turbulent bore interaction with a vertical wall. The experiments were conducted in a horizontal channel with 36.60 m length × 0.40 m width × 0.61 m height. Bores and surges on dry and wet beds were generated by releasing a water volume using a pneumatic gate with the downstream depths of $h_d = 0$ and $h_d = 0.0028$ m, respectively (Figure 2.9). A comparison between a dry and wet bed conditions demonstrated that the bore depth, run-up and force for the wet bed condition exceeded the dry bed due to steeper bore front for the wet bed. The author also reported that the Cross's (1967) theory underestimated the force exerted on the wall by approximately 20-50%.

Large-scale experiments were conducted by Kihara et al. (2015) to study the tsunami bore interaction with tide walls. The authors observed three distinct phases (impulsive, reflection and quasi-steady) in the time-history of the pressure acting on the wall. The authors reported a distinctive characteristic

for the pressure at each phase. At the higher elevations of the wall higher values of transient pressure were obtained comparing with the hydrostatic pressure at the same elevation.

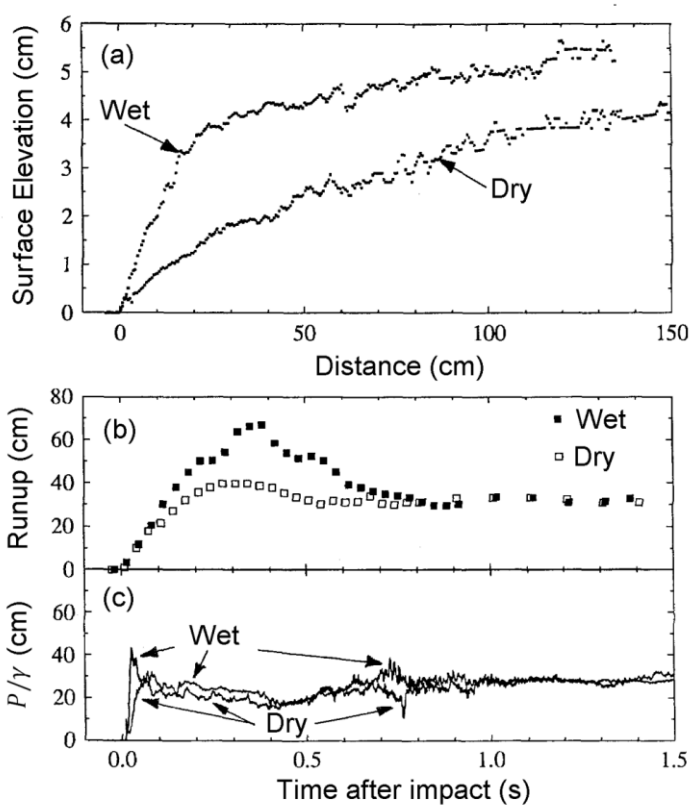

Figure 2.9: Experimental results comparisons (a) bore profile,(b) run-up, and (c) pressure head at an elevation of 0.018m above the channel's bed [Ramsden ,1993]

Linton et al. (2013) preformed large-scale experiments to estimate hydrodynamic forces acting on vertical walls over dry bed condition with different configurations. Their observation was similar to Ramsden (1993) and Kihara et al. (2015) studies which the maximum peak occurred shortly after the initial impact. This occurred during the transient force while the bore collapsed back into the incoming bore. In contrast, Ramsden (1993) had not observed any distinctive peak during reflection phase for the dry bed condition. Robertson et al. (2011) conducted an experimental study and measured tsunami forces exerted on walls. They compared the results with the force design equations in the literature (Cross 1967, Asakura 2000 and Fujima 2009) and reported an average error about 10 percent.

Árnason (2005) investigated the interaction of bores with free-piercing structures of various cross-sections. The experiments were carried out in a 16.60 m long × 0.60 m wide × 0.45 m deep channel. The bore propagated over wet bed with a downstream depth h_d = 0.02 m. The impounded water depth ranging from depths of h_u = 0.10 m to h_u = 0.30 m. As shown in Figure 2.10, the impulsive force exceeded the subsequent hydrodynamic force, however, for higher values of h_u the hydrodynamic force was greater marginally (Figure 2.10).

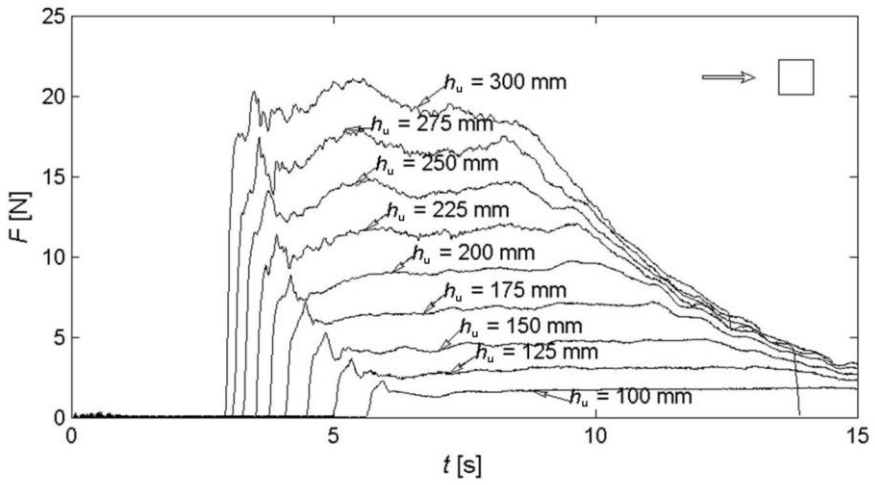

Figure 2.10 Time-history of the stream-wise force exerted on a square column for varying impounded water depths h_u [Arnason ,2005].

Al-Faesly et al. (2012) conducted experimental study in order to investigate the impact of extreme tsunami force with structures. The experiments were performed for both dry and bed condition using dam-break wave. The effects of mitigation walls on hydrodynamic force were also studied. Based on the experimental tests, the authors reported that Structural Design Method of Buildings for Tsunami Resistance (SMBTR) over-predicted the measured hydrodynamic forces by 16% to 136% while FEMA P-646 (2012) underestimates them.

2.4. Numerical Modeling of Bore-Structure Interaction

St-Germain et al. (2014) investigated the bore structure interaction using single-phase 3D weakly compressible smoothed particle hydrodynamics (WCSPH) numerical model. The numerical model was validated with the physical experiment conducted by Al-Faesly et al. (2012). Their numerical model could accurately reproduce the structure-bore interaction mechanism. Furthermore, they

examined the effects of flume geometries on the results. Two different channel widths (W, 1.3 m and 2.6 m) have been chosen for simulations (Figure 2.11). They demonstrated that by increasing the channel width, the measured bore run-up and the net stream-wise force decreased shortly after the initial impact.

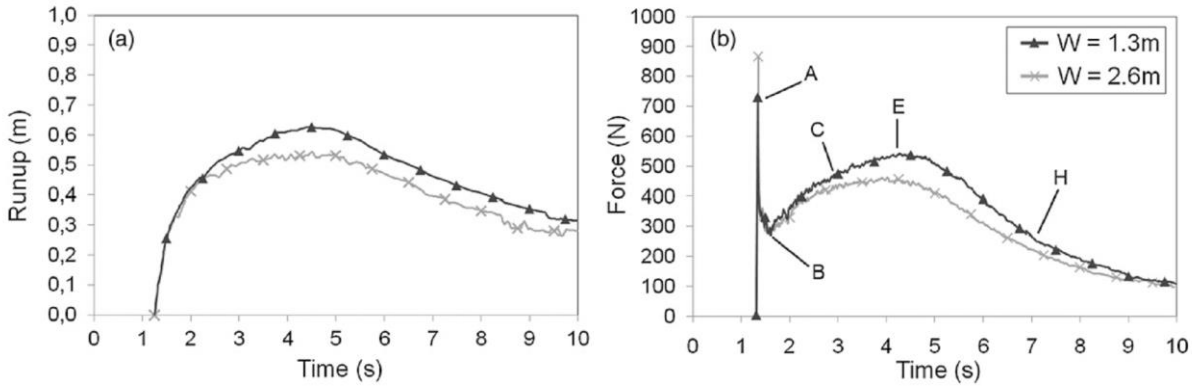

Figure 2.11:Time history of force exerted on the column for channel widths (W) of 1.3 m and 2.6 m:(a) bore run-up; (b) net stream-wise force [St-Germain et al., 2014]

Douglas and Nistor (2014) studied the influence of bed conditions dry ($h_d = 0$) and wet ($h_d > 0$) during the tsunami-like bore interaction with square cylinder using a three-dimensional multiphase numerical model. The results showed a considerable change in bore characteristics as the downstream bore depth (h_d) altered. The authors reported deeper and steeper bore front for wet bed conditions; however, the shape of the bore front was not changed substantially as the downstream depth increased. The hydrodynamic force exerted on the column was marginally reduced as the initial downstream depth increased. The reduction in hydrodynamic force was substantial for the case with downstream depth $h_d = 0.05m$ (Figure 2.12).

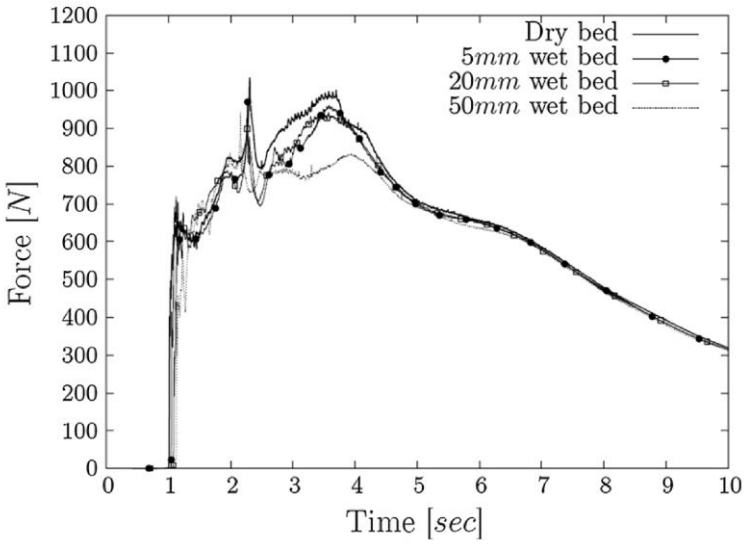

Figure 2.12: Effect of bed condition on the time-history of the stream-wise force exerted on the column, [Douglas and Nistor, 2014]

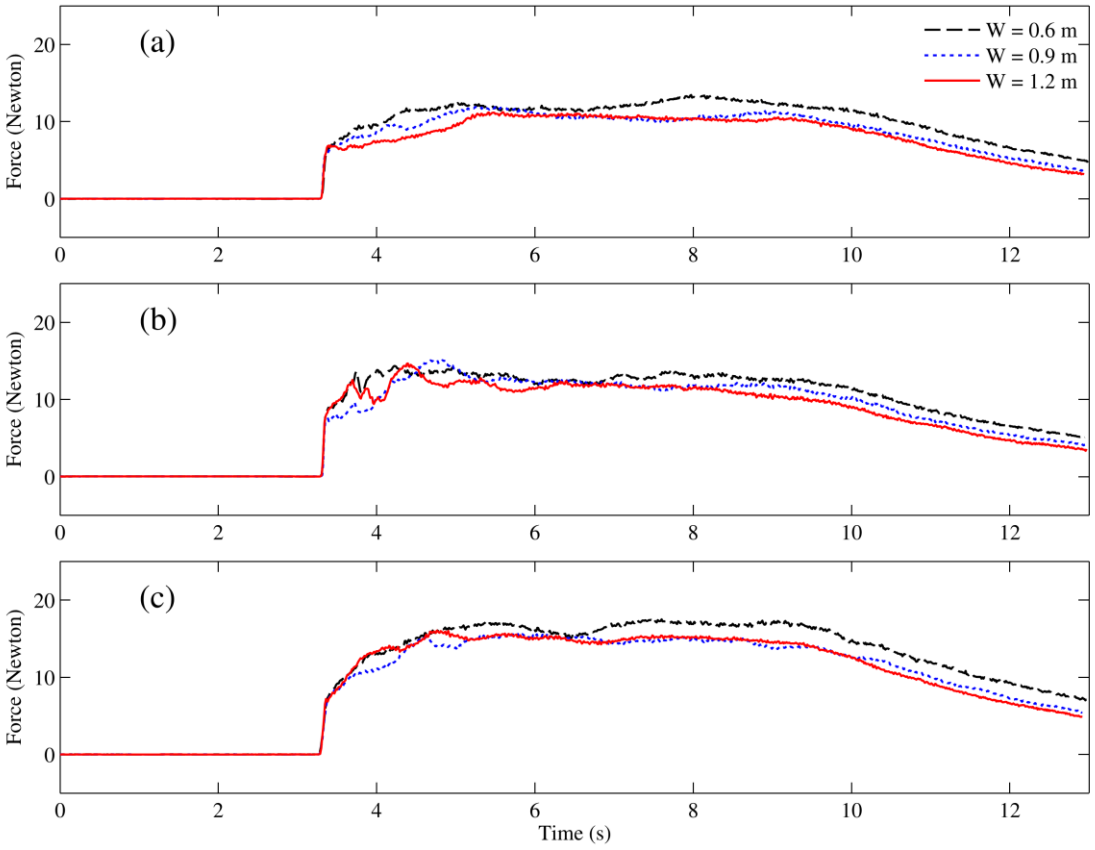

Figure 2.13: Hydrodynamic forces on column for three different channel widths. (a) Circular, (b) square, and (c) diamond [Wei et al., 2015]

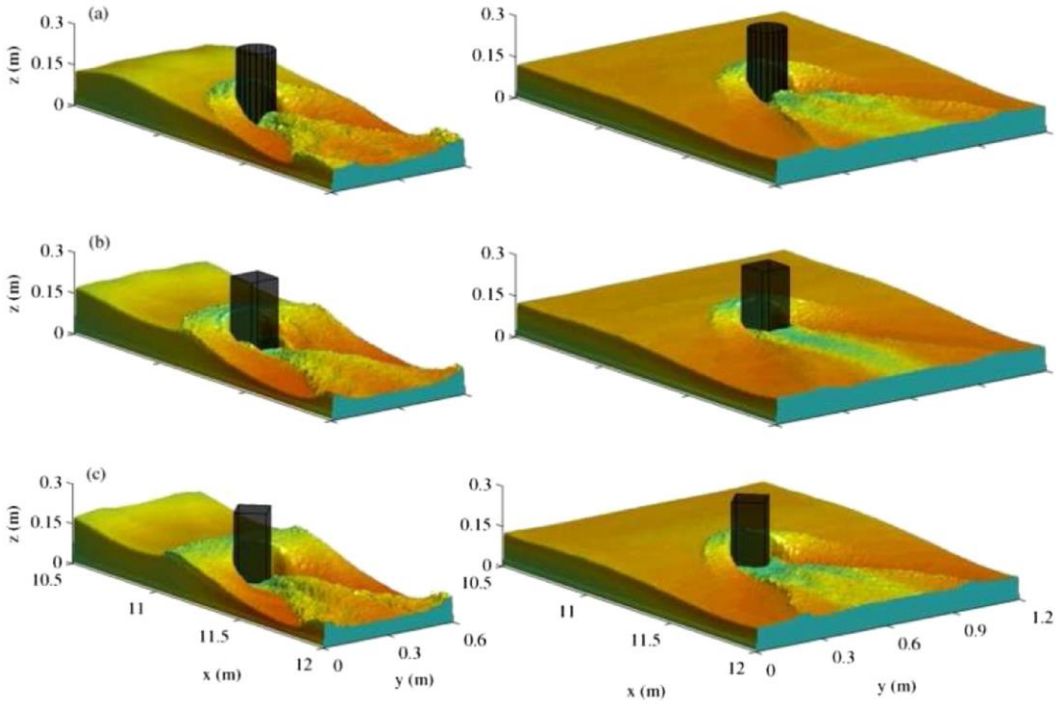

Figure 2.14: Comparison of the bore surface elevation around columns with channel width W= 0.6 m (left panel) and 1.2 m (right panel). (a) Circular, (b) square,and (c) diamond [Wei et al., 2015].

Wei et al. (2015) studied the dynamic interaction of bore with bridge piers using SPH method. The authors replicated Arnason's (2005) experimental study. Further, they extended the width of the channel and investigate the effects of side walls on the resulting forces. The results showed that a reduction in hydrodynamic forces as width of the channel increased (Figure 2.13). The comparison of bore surface elevations for different channel widths demonstrated that the water build-up induced by obstruction was no longer formed for a wider channel (Figure 2.14).

2.5. Influence of Bed Condition on Dam-Break Flow Characteristics

Many numerical studies have investigated the influence of bed condition for impact of tsunami bores on structures. Stansby *et al*. (1998) conducted small-scale experiments concerned with propagation of bores over a wet bed. The authors observed the deeper and steeper bore front for wet beds comparing with the dry bed. Jánosi *et al.* (2004) argued that the bore-front would drastically change for varying downstream water depth due to the resistance of the downstream motionless water.

Gomez-Gesteira and Dalrymple (2004) studied the bore interaction with a tall vertical structure by implementing smooth particle hydrodynamics (SPH) method. The resulting force and velocities were in a good agreement with experimental measurements.

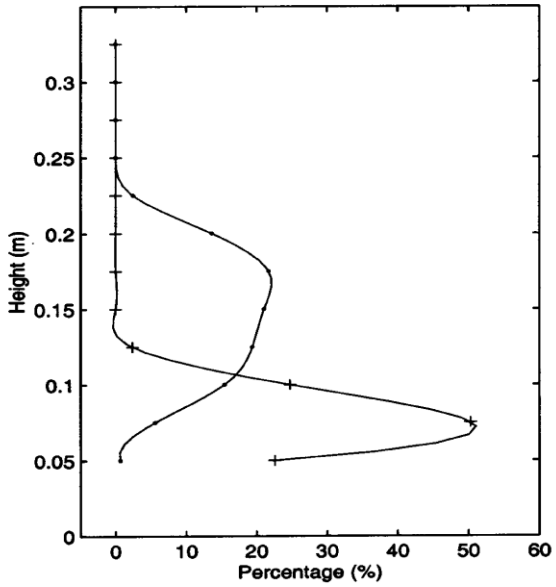

Figure 2.15 Vertical distribution of force acting on the upstream side of the structure. Wet bed (crosses) and dry bed (circles). [Gomez-Gesteira and Dalrymple, 2004]

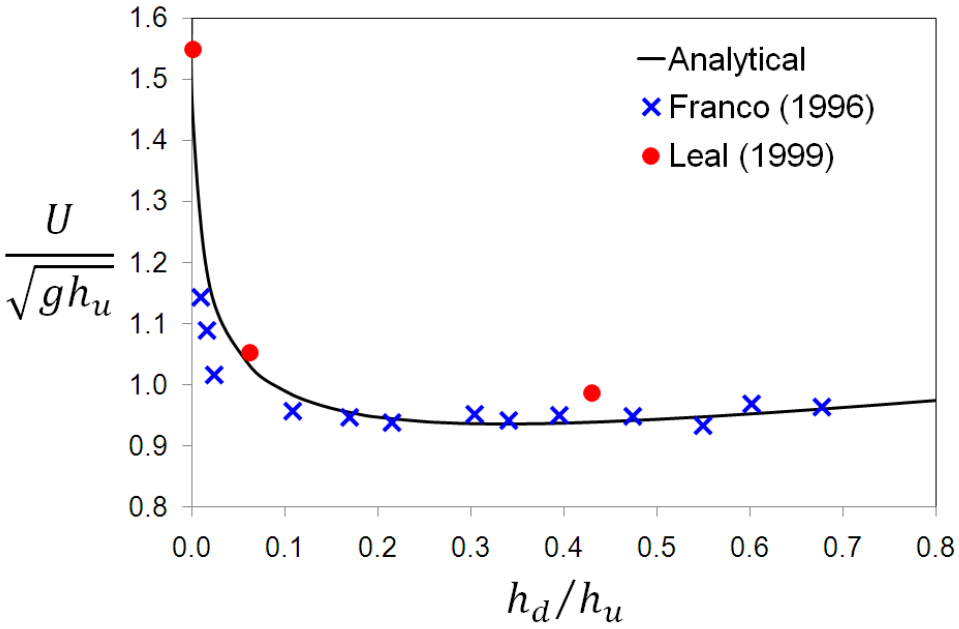

Figure 2.16 Effect of downstream water depth, h_d, on the bore-front velocity, *U* [Leal *et al*, 2006]).

The effects of downstream wet and dry bed conditions on the bore propagation were analyzed. As it can be observed in Figure 2.15, for the dry bed condition, the maximum force exerted on column occurred at the elevation less than 10 cm. On the other hand, for the wet bed condition the maximum force occurred at the elevations between 10 cm and 20 cm.

Leal et al. (2006) conducted a series of experimental tests to study the dam-break bore front celerity magnitude for different bottom frictions and downstream bed conditions (wet or dry). The authors argued that the bore front celerity decreases as the ratio of h_d/h_u increases until the bore front celerity no longer changes as h_d increased (Figure 2.16). Their results also demonstrated a good agreement with the Stoker's (1957) analytical solution.

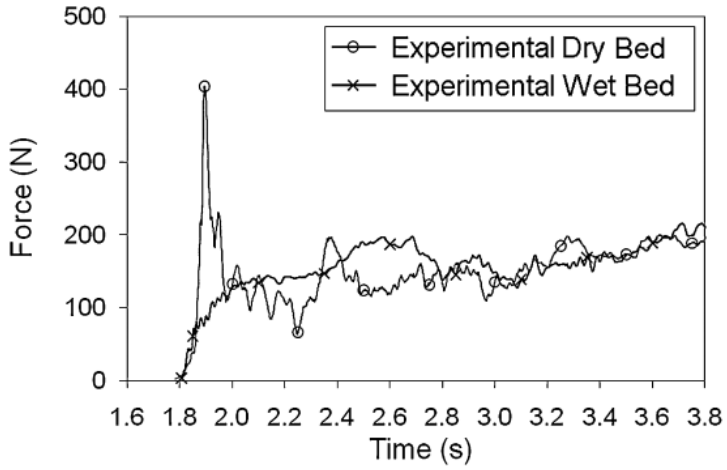

Figure 2.17 Time-history of stream-wise force acting on a structure for $h_u = 550\text{mm}$ impounded water depth [Adapted from Al-Faesly et al. (2012), reprinted from St-Germain et al., 2014]

Crespo et al. (2008) implemented two dimensional SPH method to investigate the dam-break bore evolution over wet and dry beds. Based on their observations two dissipation mechanisms including wave breaking and bottom friction were introduced as major factors causing dissipation over wet and dry bed conditions, respectively. Al-Faesly et al. (2012) conducted a series of large-scale experiments in order to study the influence bed conditions on resulting hydrodynamic forces. Interestingly, the impulsive force obtained was far larger than the subsequent hydrodynamic force for the dry bed condition. The substantial drop in impulsive force for wet bed conditions can be attributed to large amount of entrained air in the bore front which leads to lower impact pressure. St-Germain et al. (2012) used the SPH method to study

the tsunami-like bore structure interactions over the wet and dry bed conditions. Their study aimed to analyze the bore propagation characteristics and measure the resulting hydrodynamic force, velocity field and bore depth for dry ($h_d \cong 0$) and wet bed ($h_d = 0.008\text{m}$) conditions. According to the results, the bore front celerity was considerably smaller for the wet bed condition due to the resistance imposed by a water layer in the channel downstream. However, the resulting stream-wise force acting on the structure was obtained larger for the wet bed condition.

2.6. Conclusion

Based on the available research in the literature, no clear prescription on the drag coefficient of structures induced by tsunami-like bore can be found. Most of the recommended values of drag coefficient were suggested for steady flow or flow around bluff bodies. Based on the unsteady nature of tsunamis, more investigation is required to propose actual values of drag coefficients for designing the coastal structures at tsunami-prone areas. On the other hand, FEMA-P646 (2012) suggested $C_d = 2.0$ conservatively and did not consider any contributing factors on drag coefficients such as structure geometry, orientation, aspect ratio (for rectangular columns and walls defined as width to depth), bore height, blockage ratio (defined as structure width to flume width), Froude number and Reynolds number. Therefore, further investigation in this regards is essential.

Furthermore, to the best knowledge of the author, little information about how bed conditions influence on the hydrodynamic forces during the impact of tsunami-like bore with structures is available in the literature. Most of the available studies have been focused on flow propagation characteristics. This study is performed as a scaled-up two-phase numerical model based on RANS equations to investigate the hydrodynamic forces exerted on columns to calculate forces for a prototype and larger scale models.

Chapter 3. Numerical Investigation of Tsunami Bore on Drag Coefficient of structures using OpenFOAM

3.1. Introduction

Tsunamis are enormous waves mainly caused by a submarine disturbance generated by earthquakes. Other phenomena such as landslides, volcanic eruptions and meteorite can also produce devastating tsunami waves. The 2011 great Japan Tohoku tsunami and the 2004 Indian Ocean tsunami induced extensive devastation through the coastal regions (Yeh et al., 2007; Yeh et al., 2013). Mori et al. (2012), conducted a survey of inundation and run-up height in the northern coast of Japan and reported average 10-15m run-up height and greater than 30m run-up in some areas. According to Yeh et al. (2013), reinforced concrete buildings were failed substantially owing to high velocity and inundation depth. In fact, most of these structures had been designed to withstand tsunami loading. Chock et al (2013) argued that residential light-frame buildings were completely demolished and 75-95% of low-rise buildings in industrial regions were collapsed during Tohoku tsunami.

Due to these destructive tsunami events which caused exclusive human and economic casualties, the inadequacy of the current design guidelines for tsunami induced forces was revealed (Nistor et al., 2009). Most of these design guidelines were targeting storm surges and associated flooding. However, tsunami-induced bores have substantial dissimilarities in terms of their hydrodynamic characteristics and the induced forces. The current study is a part of the ongoing research conducted at the University of Ottawa to improve structural design codes for infrastructure located in tsunami-prone areas. Based on FEMA P-646 (2012) classification of tsunami loading, the hydrodynamic force is one of main factors which could cause significant structural damage. Chock et al. (2013) reported substantial structural damage to ocean facing concrete walls due to maximum hydrodynamic force. These catastrophic observations show vividly the importance of the hydrodynamic force induced by the tsunami bores in the coastal infrastructure designs. Therefore, serious modifications of the current design codes seem vital.

Different approaches have been carried out to model the tsunami generation. The solitary wave is a classical wave generation method to study the tsunami wave interaction with the structure. Numerous studies have employed the solitary wave approach in coastal processes (Synolakis,1987; Ramsden,1993; Liu et al.,1995; Robertson et al., 2011; Linton et al., 2013). However, Madsen et al. (2008) indicated that the solitary waves fail to replicate geophysical tsunami characteristics. They argued that the conversion of the front of tsunami into undular bore during shoaling usually occurs in shallow water therefore there is not enough time and distance for undular bore in the shallow water region to turn into a solitary wave. They finally mentioned that creating a soliton analogous to a real tsunami is impossible because an evolutionary distance more than any existing oceans on the earth is needed. Later, Chan and Liu (2012) utilized free surface field data during Japan Tohoku tsunami and implied that the leading edge of an actual tsunami waves are characterized as small amplitude longwave rather than solitary wave.

Wave generation using dam-break is another approach to model tsunamis. A dam-break wave can produce a highly turbulent hydraulic bore which is identical to the typical tsunami broken wave with long wavelength. The experimental reproduction of dam-break waves can be performed by sudden release of the quiescent volume of water into the flume. The dam-break wave, due to similar characteristics with tsunami waves, can model properly the tsunami interaction with coastal structures propagating onshore. Cross (1967) realized a relation between the tsunami surge and the dam-break wave. Ritter (1982) proposed a bore generation formulation using the dam-break approach in a wide frictionless channel by solving nonlinear shallow water equations. Chanson (2006) developed a theatrical model demonstrated the analogy between the dam break wave and the tsunami run-up on dry coastal areas. Chanson (2009) provided a simple analytical solution using the shallow water equations to obtain free-surface profile equations of either frictionless or friction dominated bore-fronts for dam-break waves.

Generally, the tsunami-induced stream-wise forces exerted on structures are classified into four phases depending on their characteristics (Figure 3.1). First, when the bore strikes the structure, the impulsive force occurs (the impact phase). For this case, significant amount of entrained air bubble mixing in high turbulent bore front results in shock pressure during the impact (Bullock et al., 2007). The second phase, which is called transition (reflection) phase, occurs when the reflected bore resulting from the initial impact collapses back and touches down the incoming bore (Kihara et al.,

2015; Linton et al., 2013). The peak force of this phase is more distinct when a bore impacts a vertical wall. Palermo et al., (2013) showed that the generated force (transient force) from this phase is sometimes higher than the impulsive force. Sometimes right after transient force, a force reduction (secondary transient force) happens due to sudden pressure drop on the upstream side of the column (Bullock et al., 2007). Finally, the quasi-steady phase occurs when both velocity and bore height contribute to produce maximum hydrodynamic force. At this phase, the pressure is close to the hydrostatic pressure and mostly dominant in the total pressure.

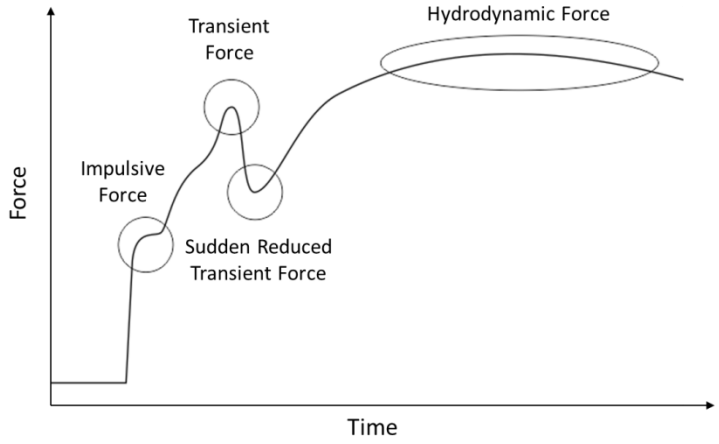

Figure 3.1: Schematic view of typical time history of stream-wise force exerted on structure for tsunami-induced bore

Many numerical and experimental studies investigated the tsunami bore-structure interaction. Yeh (2007) proposed a new method to determine the tsunami design forces. Based on his methodology, the maximum hydrodynamic force can be estimated using the maximum momentum flux at the desired location for a flow without any obstruction. Thereafter, FEMA P464 (2012) adopted the same approach for estimating the hydrodynamic force. Lukkunaprasit et al. (2009) verified the aforementioned method employing laboratory experiments based on the same field data and topography in Kamala Beach, Thailand during the 2004 Indian Ocean Tsunami. According to their results, FEMA P464 approach provides fairly plausible prediction of the hydrodynamic force.

Ramsden (1993) studied the bore interaction with vertical walls and compared wet and dry bed conditions. He asserted that both the initial run-up height and the impulsive pressure were higher for the wet bed case. No impulsive force, in the bore force time-history, was observed during the initial

impact for the both bed conditions. In addition, a transient force rise was observed only for the wet bed condition. Large-scale experiments were conducted by Kihara et al. (2015) to study the impact of tsunami like bores on tide walls. They defined three distinct phases (impulsive, reflection and quasi-steady) in the time-history of the pressure exerted on the wall. They observed that the pressure has distinctive characteristics for each phase. Linton et al. (2013) conducted full-scale experiments to evaluate forces impinging vertical walls with different configurations for the dry bed condition. Similar to Ramsden (1993) and Kihara et al. (2015), they observed that the maximum peak occurred shortly after the initial impact corresponding to the transient force due to the bore reflection onto the incoming bore. In contrast to this observation, Ramsden (1993) had not reported any distinctive peak during reflection phase for the dry bed condition. Robertson et al. (2011) measured tsunami forces exerted on walls and compared the results with the force design equations in the literature (Cross 1967, Asakura 2000 and Fujima 2009) and reported an average error about 10 percent.

St-Germain et al. (2014) investigated the bore-structure interaction using the weakly compressible smoothed particle hydrodynamics (WCSPH) numerical model. The authors validated the numerical model with the physical experiment conducted by Al-Fasely et al. (2012). The employed single-phase 3-D WCSPH numerical model could reproduce successfully the structure-bore interaction mechanism. Furthermore, they examined the effects of flume geometries on the results. Two different channel widths (1.3m and W=2.6m) were chosen for simulations. They demonstrated that by increasing the channel width, the measured bore run-up and the net stream-wise force decreased shortly after the initial impact.

One of the major parameters contributing in the hydrodynamic force equation is the drag coefficient. Currently, available values for the drag coefficients are mostly derived for the steady flow or unsteady flow in other applications. Many experimental and numerical works have been performed in the literature for high Reynolds flow around bluff bodies. Sohankar (2008) investigated the effects of side ratio on flow characteristics moving around bluff bodies with rectangular cross-sections using large eddy simulation (LES) and calculated the relevant drag coefficients. Bruno et al. (2010) studied the aerodynamic behavior of rectangular cylinder for three-dimensional high Reynolds number turbulent flow. For free surface flows, Tian et al. (2013) studied the unsteady flow around rectangular-section cylinders with different aspect ratios using k–ω SST turbulence model and compared the resulting drag coefficients with the relevant published experimental results and

numerical data. Vengatesan et al. (2000) performed an experimental investigation to measure the hydrodynamic coefficients of rectangular-section cylinders subject to random and regular waves.

For the case of tsunami bores which behave like unsteady flows (Yeh 2006), there is no clear prescription for the drag coefficient values. Moreover, these values are attributed to submerged bodies; however, the tsunami bore is categorized as a free-surface unsteady flow. The most relevant laboratory experiments to the present work were performed by Arnason (2005). He introduced the resistance coefficient (C_R) instead of drag coefficients (C_d) for the free-surface gravity controlled flow since the pressure difference between the upstream side and leeside of the structure contributes in the hydrodynamic force. The author investigated the hydrodynamic force and the associated resistance coefficient induced by the structure-bore interaction. Based on his study, the dam-break bore generation was conducted in order to study several contributing factors in the resistance coefficient such as structure geometries (dimensions and orientation), flow Froude number (*Fr*) and the bore depth.

He tested different impounded water depths (h_u) from 100mm to 300mm. Furthermore, analysis showed that by increasing the impounded water depth, and subsequently bore depth, the drag coefficient decreases. He calculated drag coefficients for two square columns with upstream side perpendicular (Figure 3.2 Left) and 45° rotated (Figure 3.2 Right) with respect to the flow direction. As shown in Figure 3.2 , the time is normalized based on the propagation speed.

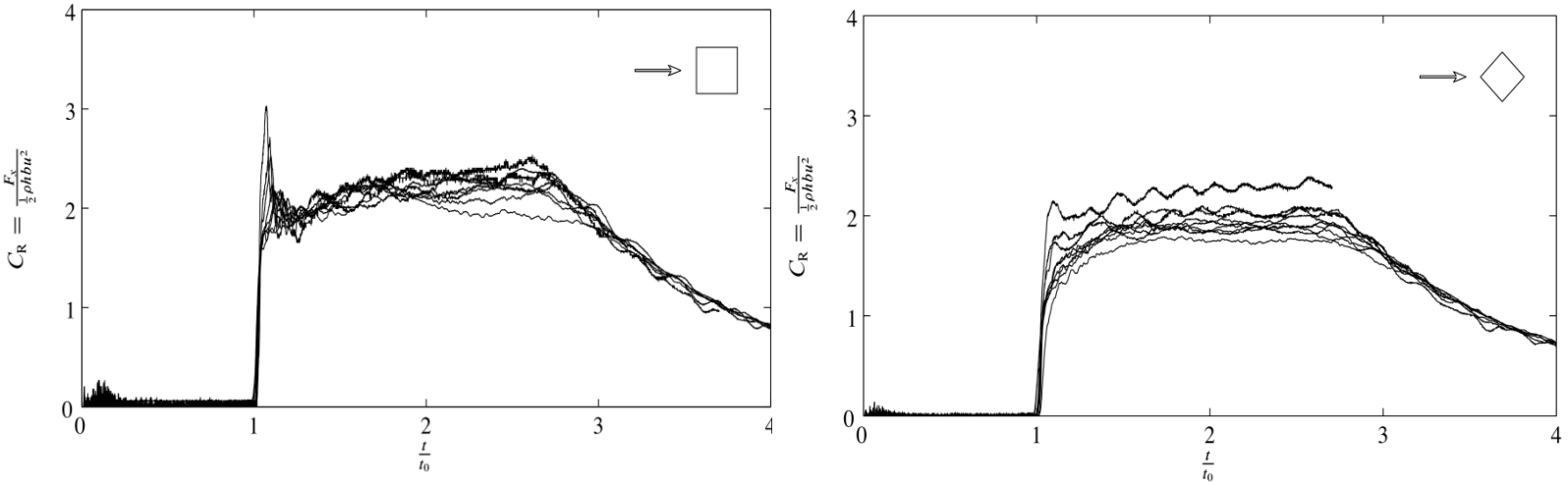

Figure 3.2: Time histories of resistance coefficient for the square column and diagonally orientated square [Arnason (2005)]

The resistance coefficient during the quasi-steady phase varies in the range of 1.99 to 2.26 for the square column with the upstream side perpendicular to the flow direction and 1.72 to 2.22 for the 45° rotated square column. This confirms the value of C_d=2.0 stated by FEMA-P646 (2012) for the square column upstream side perpendicular to the flow direction. However, FEMA-P646 (2012) does not suggest any drag coefficient values for many cases such as walls perpendicular to the flow direction, elongated rectangular columns in the direction of the flow and rotated columns with respect to the flow direction, where the bore-structure interaction mechanisms differ from the simple square column case.

Recently, Shafiei et al. (2016) conducted experiments in a 14m long, 1.2m wide and 0.8m deep flume to determine the maximum stream-wise force and associated drag coefficients for square column with different orientations. The authors measured the drag coefficients based on Cross's (1967) hypostasis which states that the total stream-wise force is the summation of hydrodynamic and hydrostatic forces. Therefore, the contribution of the hydrostatic force was not considered. In order to do so, the hydrostatic force is subtracted from the total stream-wise force and consequently the hydrodynamic force was obtained. The calculated values for C_d were 1.65, 1.4 and 1.15 for 0°, 30° and 45° rotated square, respectively.

The present paper aims at thorough investigations on the variations of the rectangular wall and column aspect ratio (AR=width/depth) and orientation (α°) and their effects on the total stream-wise force and consequently in the drag coefficients. Square-section structures have been studied extensively in the tsunami literature. However, many rectangular-section structures are employed in coastal areas buildings. As mentioned in the literature review, many column geometries have not been studied in research papers and there is no recommendation for their drag coefficients in the existing design codes (such as FEMA-P646, 2012). In the present work, a 3-D numerical model in OpenFOAM is developed and then, the model is validated using the measured experimental data of the square column experiment. Afterwards, many important cases, which do not exist in the literature, such as walls perpendicular to the flow direction (different *AR*), elongated rectangular columns in the direction of the flow (different *AR*) and rotated columns with respect to the flow direction (different α°), are modeled numerically. The results of each numerical simulation are discussed in details and the geometry-dependent drag coefficient is obtained for each case.

3.2. Description of OpenFOAM

3.2.1 General Overview

OpenFOAM (Open Field Operation and Manipulation) is a major CFD tool for simulating several physical phenomena including coastal engineering problems. OpenFOAM consists of numerous utilities, solvers and libraries, applicable in extensive range of problems. OpenFOAM source code can be modified for new problems, applications, boundary conditions and solvers. Therefore, it provides functional approach to solve complicated problems in continuum mechanics.

In the current study, the "interFoam" solver is utilized. This solver is capable of reproducing extreme water and air interactions applicable in free surface and hydraulic interaction problems. The three-dimensional Navier-Stokes equations (NSE) are solved using finite volume method (FMV) discretization for incompressible two phase flow and Volume of Fluid (VOF) method.

3.2.2 Governing equations

In this study, the fluid movement is governed by NSEs. These equations describe conversation of mass and momentum. The fluid can be assumed to be incompressible which demonstrates to be a reasonable assumption in practical coastal engineering problems. Pressure and velocity fields are linked in these equations and should be solved simultaneously. The three-dimensional continuity and momentum equations are expressed as (Rusche, 2002)

$$\nabla \cdot \mathbf{U} = 0, \tag{3-1}$$

$$\frac{\partial \rho \mathbf{U}}{\partial t} + \nabla \cdot (\rho \mathbf{U}\mathbf{U}) = -\nabla P + \nabla . \boldsymbol{\tau} + \rho \mathbf{g} + F, \tag{3-2}$$

where ρ, $\mathbf{U}$ and $\boldsymbol{\tau}$ are the fluid density, velocity vector field and the viscosity stress tensor, respectively. The quantity P, is defined as

$$P = \rho p, \tag{3-3}$$

where P is the pressure. Furthermore, in (2), F is the momentum source term due to surface tension and can be described as

$$F = \int_{S(t)} \sigma\kappa'\mathbf{n}'\delta(x - x')dS, \tag{3-4}$$

where σ, κ and **n** are the surface tension coefficient, the surface curvature and the interface normal vector, respectively. Since the fluid in this study is categorized as a Newtonian fluid, the viscosity stress tensor, **τ,** is given by

$$\boldsymbol{\tau} = \mu\,(\nabla\mathbf{U} + \nabla\mathbf{U}^T), \tag{3-5}$$

where μ is the dynamic viscosity.

3.2.3 Turbulence model

OpenFOAM provides different methods to simulate turbulent flow motion. One broadly practical method in CFD problems is to implement Reynolds-Averaged Navier-Stokes (RANS) equations. In this approach, the flow variables ($\emptyset$) represented in NSEs consists of two terms: time-averaged amount ($\overline{\emptyset}$) and fluctuation ($\emptyset'$). Therefore, the equation of $\emptyset$ can be written as

$$\emptyset = \overline{\emptyset} + \emptyset'. \tag{3-6}$$

By substituting Eq. 3-6 into NSEs, RANS equations can be derived. The additional stress term called Reynolds Stress (R_{ij}) is induced in the momentum equation. In order to model Reynolds Stress, the eddy-viscosity concept can be used. Using this concept, all turbulence properties are described as an increased viscosity. Reynolds Stress is defined based on the eddy viscosity and the mean flow strain rate terms as

$$R_{ij} = -\rho\overline{u_i'u_j'} = \mu_t\left(\frac{\partial\bar{u}_i}{\partial x_j} + \frac{\partial\bar{u}_j}{\partial x_i}\right) - \frac{2}{3}\rho k\delta_{ij}. \tag{3-7}$$

Turbulence models are introduced based on some approximations in the nonlinear terms to obtain a set of closed form equations. Basically, these models are used to determine the eddy viscosity. Moreover, the computational cost is reduced since the number of RANS equations is reduced. One of

the most popular turbulence models is standard k-ε model (Launder and Spaulding, 1974) where k denotes the turbulence kinetic energy and ε denotes the dissipation rate of turbulence energy. Shih et al., (1995) proposed a new turbulence model called as realizable k-ε by adopting an improvement over standard k-ε model. To achieve a correct physics of the complex turbulent flows certain mathematical constraints are adopted on the Reynolds stresses. The turbulent viscosity is derived by the equation below,

$$\mu_t = \rho C_\mu \frac{k^2}{\varepsilon} \tag{3-8}$$

The C_μ=0.09 is considered for the standard k-ε model. This value was observed in experimental and DNS data for boundary layer and inertial sublayer flow. To ensure that the model becomes realizable, the term C_μ must be variable rather than a constant and be related to mean strain rate. For the range of large mean strain rate, the normal stress could become negative and impact the Cauchy–Schwarz inequality assumption of shear stress. The following formulation was proposed by Reynolds (1987) and Shih et al. (1994),

$$C_\mu = \frac{1}{A_0 + A_s \frac{Uk}{\varepsilon}} \tag{3-9}$$

Further information is provided in Shih et al. (1994). The transport equations for realizable k-ε are expressed as

$$\frac{\partial}{\partial t}(\rho k) + \frac{\partial}{\partial x_i}(\rho k u_i) = \frac{\partial}{\partial x_i}\left[\left(\mu + \frac{\mu_t}{\sigma_k}\right)\frac{\partial k}{\partial x_i}\right] + G_k + G_b - \rho\varepsilon - Y_M + S_K \tag{3-10}$$

$$\frac{\partial}{\partial t}(\rho \varepsilon) + \frac{\partial}{\partial x_i}(\rho \varepsilon u_i) = \frac{\partial}{\partial x_j}\left[\left(\mu + \frac{\mu_t}{\sigma_\varepsilon}\right)\frac{\partial \varepsilon}{\partial x_j}\right] + \rho C_1 S\varepsilon - \rho C_2 \frac{\varepsilon^2}{k + \sqrt{v\varepsilon}} + C_{1\varepsilon}\frac{\varepsilon}{k} C_{3\varepsilon} G_b + S_\varepsilon \tag{3-9}$$

The constant values of realizable k-ε model are assigned as $C_{1\varepsilon} = 1.44$, $C_2 = 1.9$, $\sigma_\varepsilon = 4.38$ and $\sigma_k = 0.7179$. Further information regarding Eq.3-9, Eq.3-10 and Eq.3-11 are presented in Shih et al. (1995).

3.2.4 Volume of fluid model (VOF)

VOF method was initially presented by Hirt and Nichols (1981). This technique is capable of capturing complicated free surface elevations using the volume fraction function. Based on this concept, the interFoam solver employs an indicator function (α) to determine the fractional volume of each mesh cell. Since the application of this study is free surface flow, only water and air are considered here. Therefore, whenever the cell is completely filled with water, the corresponding fraction phase volume is 1 while 0 indicates that the cell is occupied with air. The values between 0 and 1 are considered as a free surface. The fluid physical properties can be simply weighted using the VOF method as shown in Eq.3-8 where the dynamic viscosity, μ, is estimated a

$$\mu = \alpha\mu_{water} + (1-\alpha)\mu_{air} \ . \tag{3-10}$$

The fluid movement is described by the advection equation as

$$\frac{\partial \alpha}{\partial t} + \nabla . \mathbf{U}\alpha = 0 \tag{3-11}$$

Weller (2002) proposed an artificial compression term, $\nabla . \mathbf{U_c}\alpha(1-\alpha)$, in order to improve the interface resolution. Therefore, Eq. 3-9 is re-written as

$$\frac{\partial \alpha}{\partial t} + \nabla . (\mathbf{U}\alpha) + \nabla . \mathbf{U_c}\alpha(1-\alpha) = 0 \tag{3-12}$$

where $\mathbf{U_c}$ (defined as $\mathbf{U_c} = \mathbf{U_l} - \mathbf{U_g}$) is the relative velocity between liquid ($\mathbf{U_l}$) and gaseous phase ($\mathbf{U_g}$) , representing water and air, respectively. The term $\mathbf{U}$ in Eq. 3-13 is defined as the effective fluid velocity. This velocity is obtained by weighted average of gas and liquid velocities based on their corresponding phase fraction as

$$\mathbf{U} = \alpha\mathbf{U_l} + (1-\alpha)\mathbf{U_g} \tag{3-13}$$

3.2.5 Time step control

The self-adapting time step is implemented to ensure that a proper stability of the calculations would be achieved. For this reason, the time step is adjusted using the predefined upper limit values for courant number ($Co_{\max}$) and time step ($\Delta t_{\max}$). The courant number is defined as

$$Co = \frac{|U_f . S_f|}{d . S_f}\Delta t \tag{3-14}$$

where d is a vector between the adjacent faces of two control volume. The quantities U_f and Δt in Eq. 3-15 are obtained from previous time step. Based on these values the new time step can be measured (Berberović, 2009).

$$\Delta t^n = \min\left\{\frac{Co_{max}}{Co^0}, \left(1+\lambda_1\frac{Co_{max}}{Co^0}\right)\Delta t^0, \lambda_2\Delta t^0, \Delta t_{max}\right\} \tag{3-15}$$

where Co^0 is the value of maximum local courant number. Berberović (2009) suggested that the maximum value of courant number should not be more than Co_{max}=0.2. The damping factor values $\lambda_1 = 0.1$ and $\lambda_2 = 1.2$ are specified to prevent instability due to time step fluctuation. As long as the maximum local courant number does not exceed the limit value, the stability of time step could be acquired. On the other hand, the intermediate time step (Δt^*_{ini}) is specified at the beginning of the simulation to obtain the initial value for time step as

$$\Delta t^*_{ini} = \min\left(\frac{Co_{max}}{Co^0}\Delta t_{ini}, \Delta t_{max}\right). \tag{3-16}$$

This intermediate value in Eq.3-16 as Δt^0 provides reasonable values for maximum local courant number and subsequent new time step.

3.3. Model validation

3.3.1 Physical experiments of Al-Faesly et al. (2012)

The experiments were carried out at the Canadian Hydraulic Center of the National Research Council (NRC-CHC) flume, located in Ottawa. The high discharge flume was 14.56m long, 2.7m width and

1.4m height constructed from stainless steel cross-section (Al-Faesly et al., 2012). The schematic plan layout of the physical experiment is illustrated in Figure 3.3. Dam break mechanism is used in order to generate tsunami-like bores. Based on this method, by suddenly removing the swinging gate, the water column collapsed and the hydraulic bore advanced into the downstream. The gate removal time provided instantaneous water release due to the Lauber and Hager (1998) criteria. They proposed that the proper duration for the gate removal non-dimensional time should be less than $\sqrt{2}$ in order to create a sudden dam break. According to Al-Faesly (2016), this requirement was met during the experiment (maximum non-dimensional time = 0.484).

The bending part inside reservoir provides a water supply. To avoid bore reflection into the upstream side, a vertical drain is located at the downstream end of the flume discharging flow underneath of the flume. The structural square column fabricated using four 6.3-mm-thick acrylic sheets is located at the proper distance (4.92m) from the gate to ensure that the bore is fully developed. The 0.305x0.305x1m square column was positioned symmetrically inside the flume (Figure 3.3). In order to measure bore depth and observe bore propagation, wave gauges (Capacitance-type) are placed inside the flume. Their configurations are shown in Figure 3.3. The force measurement was conducted through a six-degree-of-freedom dynamometer attached to the column's base. For capturing the pressure, ten pressure transducers (PT), Honeywell 20PC Series, were positioned vertically on the upstream face of the column.

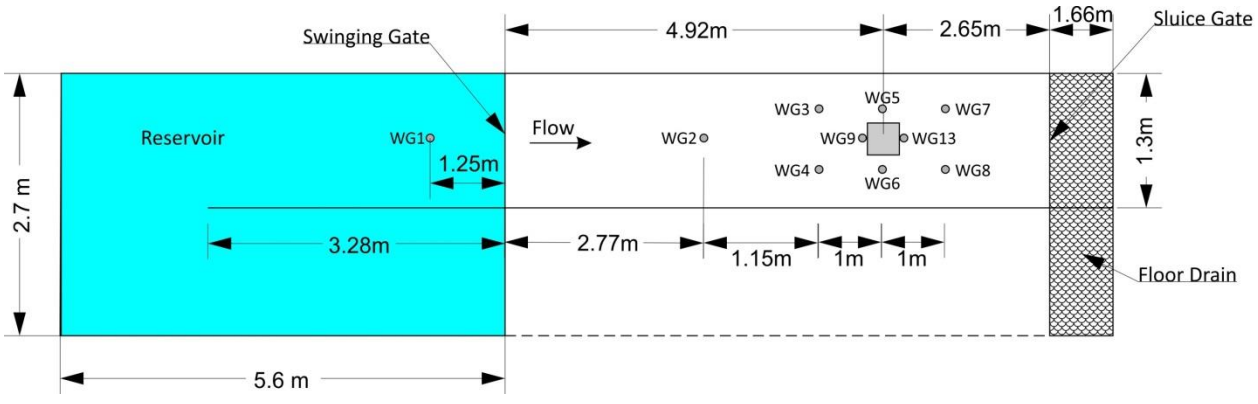

Figure 3.3 Plan view of the physical experiment

3.3.2 Numerical experiment

3.3.2.1 The Computational Domain

In this section, the numerical replication of the Al-Faesly et al. (2012) physical experiment is presented. The configuration of the experiment shown in Figure 3.4 is modeled. The downstream wall is not modeled to prevent any backflows. The initial configuration of the numerical simulation is shown in Figure 3.4.

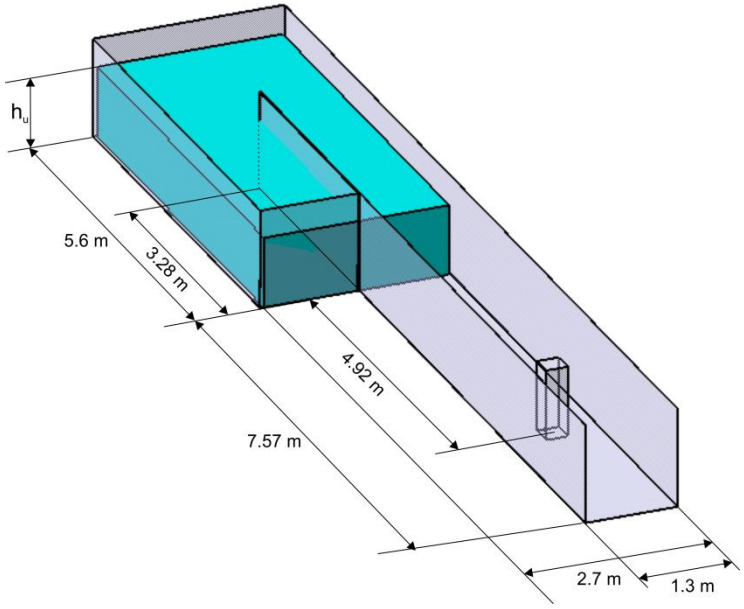

Figure 3.4: Computational Domain

Due to expensive computational cost of structured mesh, the domain is meshed by unstructured grid. Better resolution is chosen near the column because more accurate results are needed in these regions. Therefore, the mesh resolution is kept refined inside the region 1.5m away from the column to capture turbulence effects accurately. The mesh discretization is 1×1×2cm at the column location in x, y and z directions, respectively. In x direction along the flume length, the mesh resolution starts from 1cm near the column and ends at 4cm, 1.5m away from the column. Mesh cell size is also 1cm in y direction along flume width and gradually increases. As it reaches the flume walls, the mesh cell size becomes 3cm. The general mesh discretization size in the vertical direction is 2cm which allows for using the orthogonal mesh. All three impounded water depths (0.55m, 0.85m, 1.15m) are simulated for numerical runs.

3.3.2.2 Sensitivity Analysis

Sensitivity analyses have been performed to achieve a desirable combination of numerical parameters. Initially, the influence of mesh variation is tested using different mesh resolutions. Both unstructured and structured meshes are tested. Figure 3.5 compares bore force exerted on column for three different structured cell discretization sizes with unstructured mesh, refined near the column. As shown in Figure 3.5, the 1×1×2cm unstructured mesh gives good agreement with experimental results. The impulsive force is captured well using 1×1×2cm grid size. This supports the selected mesh resolution accuracy since the other grid sizes underestimate the impulsive force. Furthermore, the hydrodynamic peak occurred at 3.6sec after gate removal for 1×1×2cm grid size shows very good agreement with the experiment while 2×2×2.5cm grid shows almost 18 percent difference. It can be observed that moving from 2×2×2.5cm refined mesh to 1×1×2cm, there is a significant difference for hydrodynamic peak measurement. Although, 1×1×2cm refined structured mesh has no major difference with the same size unstructured mesh, using unstructured mesh saves computational cost since the number of mesh cells has been reduced substantially relative to the same refined structured mesh. Therefore, as mentioned earlier, the final grid size is considered 1×1×2cm.

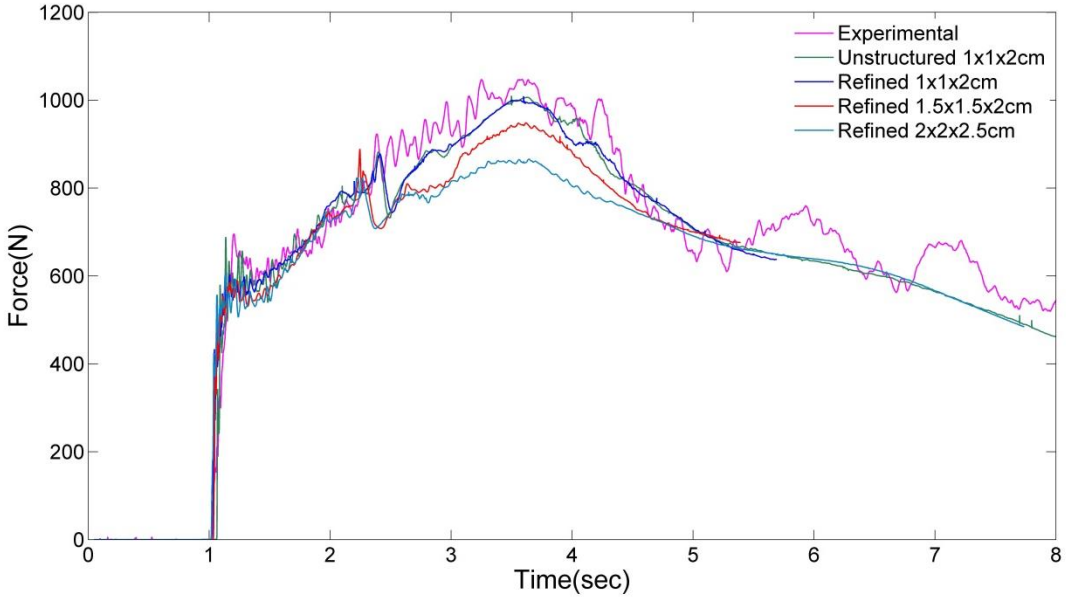

Figure 3.5: Sensitivity analysis for mesh resolution

Different turbulence models were used in numerical simulation in order to determine the best match with respect to physical experiment. Most importantly, turbulence effects on net force exerted on column as well as free surface elevation are investigated. Turbulence effects are tested using k-ε, k-ω SST (Wilcox et al., 1988), realizable k-ε , Re-Normalized group (RNG) k-ε (Yakhot et al., 1991) models. The illustration in Figure 3.6 shows the results of net force exerted on column for different turbulence models and their compatibility with respect to experimental data. No major difference is observed between these models however, Root mean square error (RSME) measurement shows slightly better agreement for realizable k-ε model. Moreover, the hydrodynamic pick obtained by realizable k-ε model occurred after 3.6sec from the gate removal which follows the same trend of experimental model. Besides, the actual impulsive force is only observed by realizable k-ε model. All numerical models show fairly good agreement during transient force except k-ε turbulence model which slightly overestimates the force. As a consequence, although all of these numerical simulations demonstrate good agreement relative to experimental results, the realizable k-ε models gives the best match. Therefore, all further cases have been tested using realizable k-ε turbulence model.

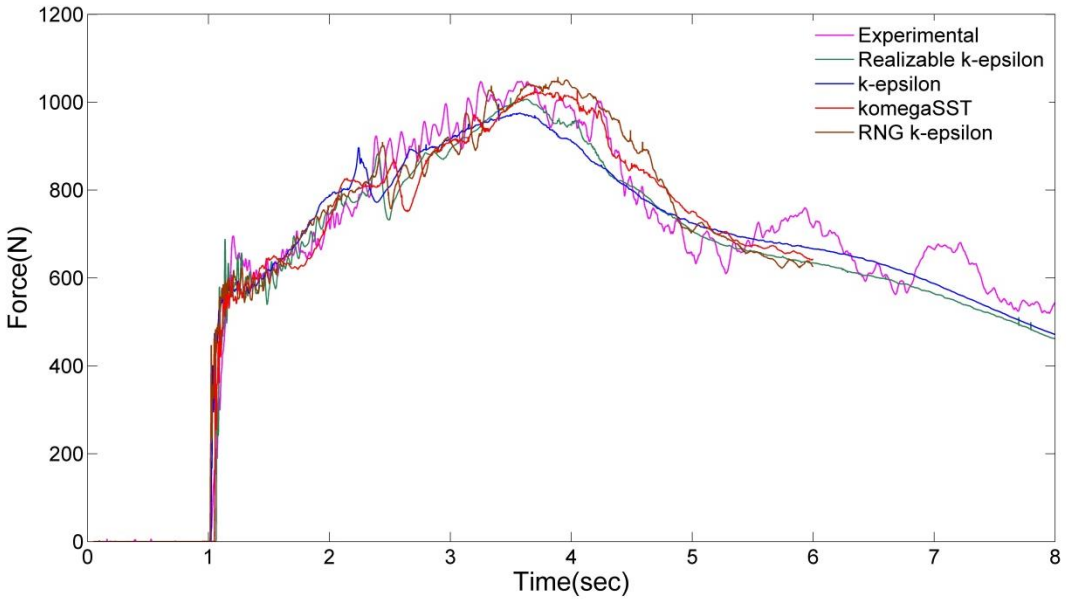

Figure 3.6: Sensitivity analysis for turbulence models

3.3.2.3 Comparison of numerical and experimental model results

3.3.2.1.1 Water surface elevation

The numerical simulations are compared with the experimental measurements qualitatively and quantitatively. In order to show the accuracy of the simulation results, net stream-wise force and bore surface elevation comparisons with corresponding experimental results are presented in this section. First, the temporal variations of free surface elevations are compared for several different wave gauges (WGs) as shown in Figure 3.3. Therefore, the flume is reproduced numerically in the absence of the column. As it can be observed from Figure 3.7, although numerical results agree fairly well with the experimental results, some discrepancies occur for WG1 inside the reservoir and WG2 located at the downstream side from the gate. Similar studies by St-Germain (2012) and Douglas and Nistor (2014) also reported the same trend at WG1. The discrepancy is more considerable after 5.0 sec which shows that the numerical model captured lower water surface levels. This is because the water is depleted quicker during the numerical model since the water supply was pumped and the pump remains open during the experiment.

Furthermore, the water level at WG2 for the experimental test exceeded that captured by the numerical model. This discrepancy was also reported by St-Germain et al. (2014). Based on the video analysis of the physical experiment, the formation of cross-waves was observed owing to the shock waves induced by gate's fixture at the location of the WG2 (St-Germain et al., 2014). After the bore propagated into the downstream, a good agreement in water level between the numerical simulation and experimental measurements are observed for WG3 and WG5.

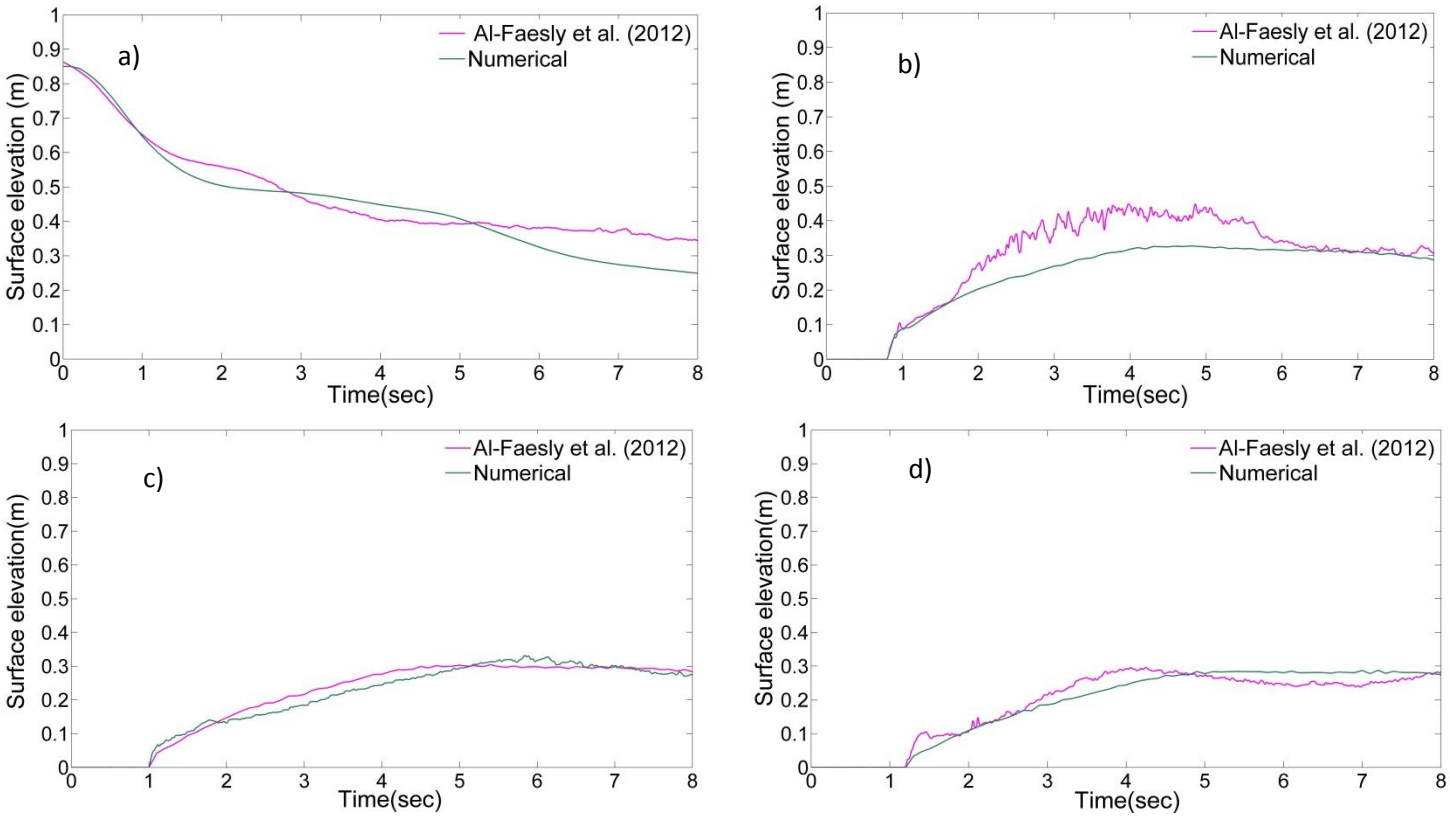

Figure 3.7: Water surface temporal variation for $h_u = 0.85m$ a) WG1; b) WG2; c) WG3; d) WG5

3.3.2.1.2 Net stream-wise bore force

The time histories of the net stream-wise bore force exerted on the column in the numerical simulation are shown in Figure 3.8. The net stream-wise bore force exerted on the column was obtained by integrating the pressure on all column faces. The time histories of the numerical simulation results of the net force demonstrate good agreements with the measured experimental forces. In the case of $h_u = 1150$mm, the simulated forces for both impulsive force and hydrodynamic force are in good agreement with the experimentally measured forces.

In the case of $h_u = 850$ mm from 3.0 sec to 4.0 sec, the values of the simulated force are relatively lower (8% error) than the measured forces. Despite this discrepancy, the overall trends of the numerical results and experimentally measured time histories of force show a good agreement. The impulsive force observation indicates that the numerical model was capable of reproducing the initial impact. Further, for both models after 5.0 sec some oscillations can be observed in the wake of the

column which is caused by significant turbulence and aeration. Interestingly, for $h_u = 1150$ mm, the transient force did not produce an excessive rise relative to the experiment. However, for the case $h_u = 850$ mm, a sudden spike appeared around 2.5 sec which corresponds to the transient force.

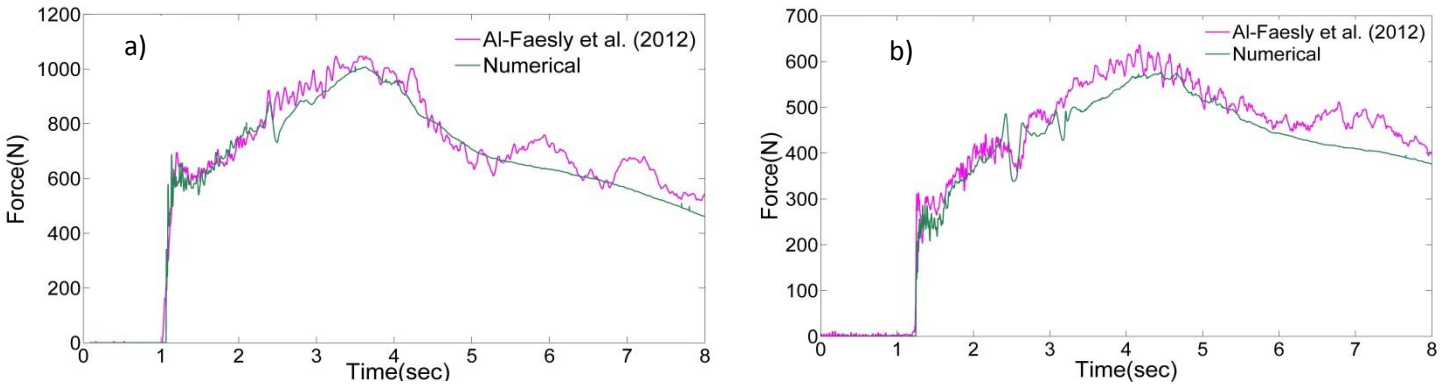

Figure 3.8: Time history of stream-wise force exerted on column a) $h_u = 1150$mm b) $h_u = 850$mm

3.4. Drag Coefficient

3.4.1 Methodology

Higher hydrodynamic force can cause higher level of damages on the structures. This force which is induced by tsunamis is also called the drag force in the fluid dynamics which consists of both pressure and friction drag forces. The friction drag force consists of shear forces caused by motion of the fluid around the structure, while the pressure drag force is generated by the flow pressure on the structure. However, the drag force of the free surface flows differs from the fully submerged bluff bodies, due to the fact that the hydrostatic pressure is different on the front side and leeside of the structural column. According to FEMA P646 (2012), the equation of the hydrodynamic force can be written as

$$F_D = \frac{1}{2} C_d \rho B h u^2 \tag{3-17}$$

where C_d, ρ, u, h and B are drag coefficient, fluid density, ambient flow velocity, bore depth and projected width of structure normal to the flow direction, respectively. Gupta and Goyal (1975) studied the flow around the bridge piers for steady flows. They suggested a term called resistance coefficient (C_R) instead of drag coefficient due to the contribution of the hydrostatic force for the free

surface flows. Due to the unsteady behavior of tsunami waves, the resistance coefficient is time history dependent rather than a constant coefficient (Arnason 2005).

In order to determine the hydrodynamic force, FEMA P646 (2012) suggests to calculate a term, $(hu^2)_{max}$, which represents the momentum flux using numerical simulation models. Since maximum value for both h and u might not happen at the same time, the temporal variation of the momentum flux value (hu^2) should be measured to calculate the hydrodynamic force accurately. In addition, the grid size at the run-up zones should be fine enough to ensure the accuracy of the simulations. Finally, the reverse process is implemented to compute the drag coefficient (C_d) using the numerical results such as net stream-wise bore force (F), bore depth (h) and the flow velocity (u). In order to measure the drag coefficient, both bore depth (h) and flow velocity (u) are taken from unobstructed flow condition (Yeh, 2007). Therefore, all numerical simulations are initially performed for no obstruction condition for different impounded water depth to measure the temporal variation of hu^2 term at the structure location.

It is worth mentioning that in the present work, the drag coefficient is equivalent to the resistance coefficient since the force obtained from numerical results contains both the hydrodynamic and hydrostatic force. Yeh (2006) determined the envelope of the momentum flux by employing the nonlinear shallow water wave theory for a uniform beach slope condition. In the absence of precise numerical simulations, Yeh (2007) approximated the value of $(hu^2)_{max}$ by the following equation:

$$\frac{(h\,u^2)\max}{g\,R^2} = 0.125 - 0.235\frac{z}{R} + 0.11\left(\frac{z}{R}\right)^2, \qquad (3\text{-}20)$$

where z, R and g are ground elevation, maximum run-up height and gravitational acceleration, respectively. The z and R terms can be obtained from tsunami inundation maps.

3.4.2 Effects of sidewalls

In order to assure the analogy between the scaled numerical model and the prototype, the Froude number equivalence for free surface flows is ensured. Effects of sidewalls, in the numerical and physical models, can cause significant discrepancies between the numerical simulations and the real-

world prototype. The effect of sidewalls can be investigated using the blockage ratio (*BR*= structure width/flume width). The numerical domain is scaled up using this ratio to eliminate the influence of sidewalls on the net stream-wise force and other bore characteristics. To assess how the sidewalls affect the bore-structure interaction, the flume width is increased and the time histories of the force exerted on the column are compared for different blockage ratios (Figure 3.9a). The flume width increases until no significant difference is observed in the measured forces exerted on the column in the numerical simulations.

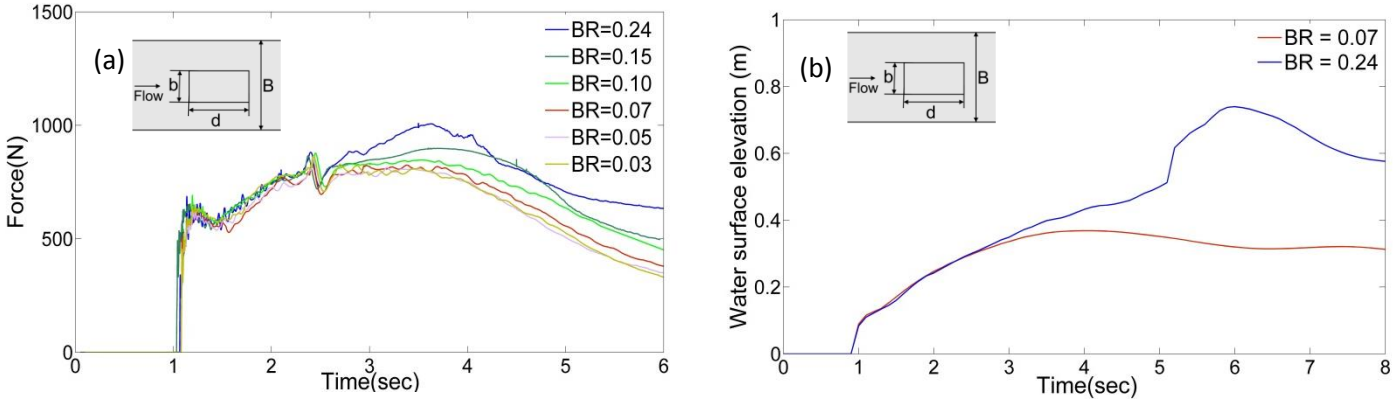

Figure 3.9: Influence of blockage ratio on a) Net stream-wise force b) Bore Surface elevation

As illustrated in Figure 3.9a, no major difference between blockage ratios less than 7 percent was observed. As the bore impinges the column, the run-up height increases and then it collapses back onto the incoming bore and consequently forms a surface-roller. This surface-roller then propagates into the upstream-side and toward the sidewalls. For a narrower flume (lower blockage ratio), the surface-roller is reflected by the side wall and causes a subsequent water level to build-up behind the upstream face. This difference between bore surface elevation for BR=0.07 can be observed clearly in Figure 3.9b after 2.7sec passed from the simulation when the wall effects occurred. Moreover, Figure 3.10 illustrates the quantitative and qualitative comparisons of water surface elevation on the upstream side of the flume. For the case of BR=0.07, the surface-roller dissipated before reaching the sidewalls, therefore no water accumulation occurred behind the upstream side. St-Germain et al. (2014) doubled the flume width to examine the sidewall effects and they also observed that the both bore net stream-wise force and run-up elevation reduced during the hydrodynamic (quasi-steady) phase. It should be noted that the occurrence of hydrodynamic force peak for higher blockage ratios occurs when the water surface elevation rise at the upstream side while for higher blockage ratios,

the quasi-steady phase is almost constant. Arnason (2009) also observed the formation of bow wave (surface-roller) during the maximum hydrodynamic force peak and presumed that both critical flow condition and sidewall effects caused the aforementioned phenomenon.

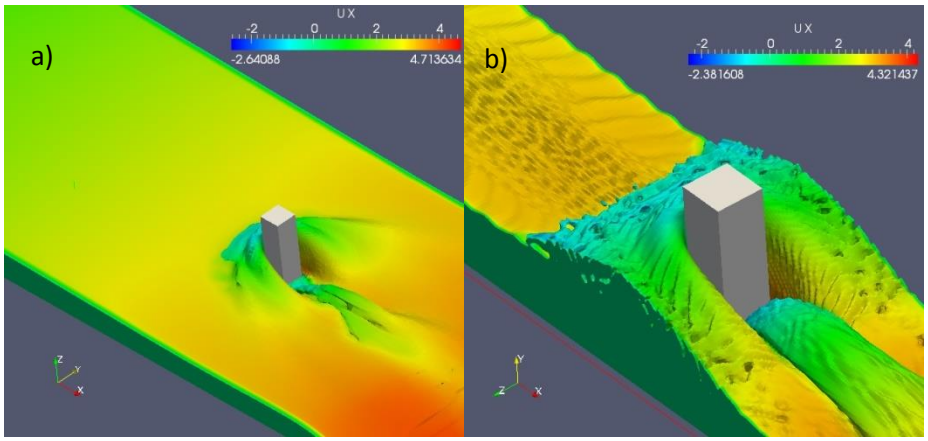

Figure 3.10: Qualitative comparison of the bore surface elevation a)BR=0.07 b)BR=0.24

3.5. Results and Discussion

3.5.1 Influence of structural geometry

In this section, the structure geometry effects on drag coefficients and other hydrodynamic characteristics are investigated. Different column geometries are modeled numerically such as square and rectangular-section columns and walls with different aspect ratios and orientations. For simplicity, the bending part of the flume is not modeled. The schematic view of the computational domain for aforementioned column is presented in Figure 3.11. The blockage ratio (BR) is kept 0.07 for all the simulations to eliminate the wall effects (Section 3.4.2). For the rectangular-section columns, the numerical simulations are performed for the selected aspect ratios, AR= 1,2,4,6,8 and for the rectangular-section walls, the aspect ratios, AR= 2,4 are chosen. The reference cross-section is a square column as 0.305m×0.305m. In order to investigate the column orientation (α) effects, the square column is rotated about its axial axis by 0°,22.5°, 45° and 67.5° with respect to the bore flow direction. Finally, the rectangular-section columns with AR=4 and the orientation angles 22.5°, 45° are simulated numerically.

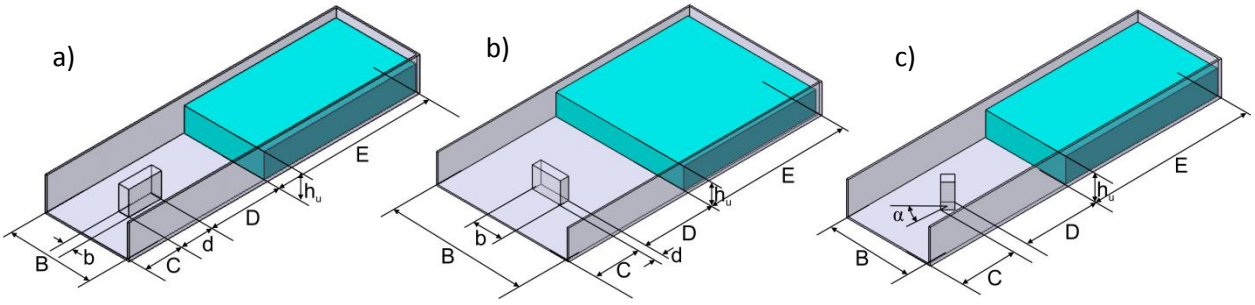

Figure 3.11: Structural geometry variation a) elongated column b) rectangular wall c) rotated square column, $E = 8.6m, D = 4.75m, C = 2.5m,$ AR=b/d, α=0°,22.5°, 45°.

3.5.2 Rectangular columns with different aspect ratios

3.5.2.1 Net stream-wise force

The hydrodynamic effects caused by the elongated column in the flow direction are presented in this section. The numerical simulations are performed for $1150mm, 1000mm, 850mm$ and $550mm$ impounded water depths (h_u). The time history net stream-wise force are presented in Figure 3.12 for $h_u = 1000$mm and $h_u = 550mm$. The initial impact force shows almost the same values for all aspect ratios. This trend is similar for all aspect ratios owing to the similar location from the gate and same geometry of the upstream face exposed to the hydraulic bore. As illustrated in Figure 3.12, the total force exerted on column slightly increases by elongating the column in the flow direction. On the other hand, for all impounded water depths, the hydrodynamic force occurring at the quasi-steady state phase shows a constant variation. According to Arnason (2009), the influence of flume sidewalls leads to additional water level built-up at the upstream face and subsequent higher bore level. This leads to a distinctive force peak during the quasi-steady force. This force is not observed in the current study which shows that the influence of wall is properly eliminated.

Moreover, for all adapted initial impounded water depths, the value of the transient and hydrodynamic quasi-steady forces overshoot the impulsive force. This supports Arnason's (2005) results which indicated that the initial impact force was less than the quasi-steady force for the impounded water depths higher than 200 mm. Although for impounded water depths less than 200mm, the initial impact force was higher, for the case of $h_u = 550mm$ the initial impulsive force is less than 50% of subsequent hydrodynamic force. In addition, only for this employed impounded

water, the transient force is slightly less than the later hydrodynamic force. It should be noted that for lower initial impounded depth, the transient and impulsive forces were not distinguishable in Arnason's (2005) study. As illustrated in Figure 3.12, around 2.3 sec, a momentarily distinct rise occurs for all simulations. This rise is attributed to the transient force occurring at the reflection phase. Moreover, it can be observed from Figure 3.12 that by increasing the aspect ratio of the column, the hydrodynamic force slightly increases.

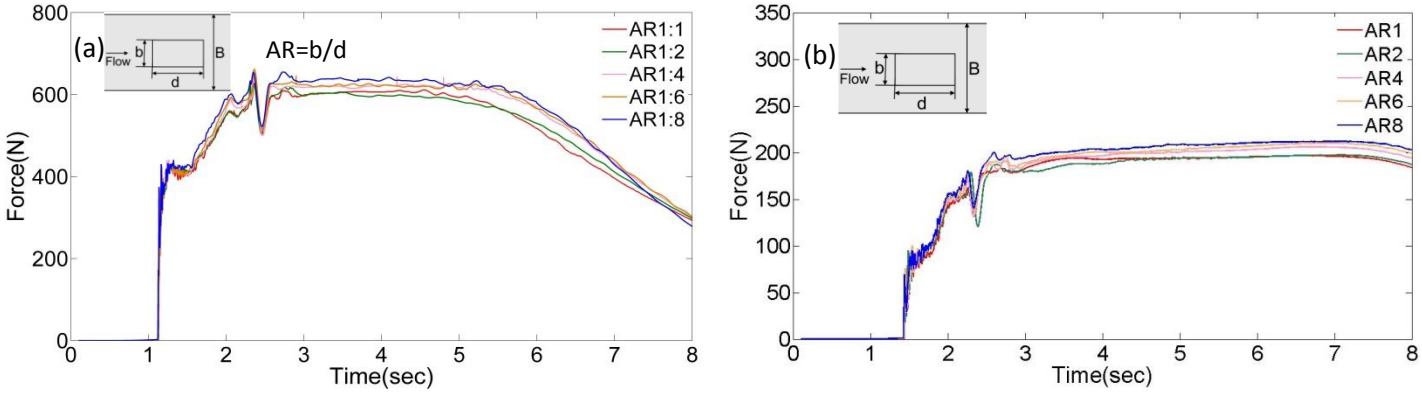

Figure 3.12: Time history of net stream-wise force for different impounded water for column with AR1, AR2,AR4, AR6 and AR8 a) $h_u = 1000mm$ b) $h_u = 550mm$

This rise is due to the increase in both shear force on column sides and pressure difference on upstream side and leeside of the column. The constant gradual increase in the total net stream-wise force appears shortly after the initial impact at 1.2 sec. This difference can be seen in Figure 3.13 which shows the friction force variation exerted on column sides. However, this increase in total stream-wise force is not a considerable amount when aspect ratios increase. As shown in Figure 3.13, the maximum difference in total stream-wise force between AR1:1 and AR1:8 is %8 during the hydrodynamic phase. The general trend indicates that the aspect ratio increase leads to increase in the shear stress on the side walls of the column. However, the friction force induced by shear stresses has a small contribution to the total stream-wise force. Comparing Figure 3.12 with Figure 3.13 shows that shear force (Figure 3.13) contributes less than 5% in total stream-wise force for the numerical simulation of AR1:8.

A similar low contribution of shear stress relative to pressure force is also reported in Wu, (2004) and Lin and Li (2003) work. Wu (2004) obtained the same results for the dam break wave problem hitting the square column by implementing both LES and k-ε turbulence models. He concluded that

the contribution of shear stress is less than 1% which is negligible. As shown in Figure 3.13a, a dip occurred at the first moments of the simulations. This is attributed to the recirculation regions occurred after the separation points which are located at the leading edge of the column. Shortly after the dip the positive force starts to grow due to the flow reattachment as shown in Figure 3.13b. Furthermore, as mentioned, the other factor which could contribute in resulting force for different aspect ratio is pressure difference between the upstream side and leeside of the column. The vortices were formed in the wake of the column and were extended as far as the column width. This causes a low pressure region at the leeside of the column and subsequent higher pressure difference. Eventually, these two increases in shear and pressure forces cooperate and result in an increase in total net stream-wise forces exerted on the column. The effects of pressure difference are presented in the next sections.

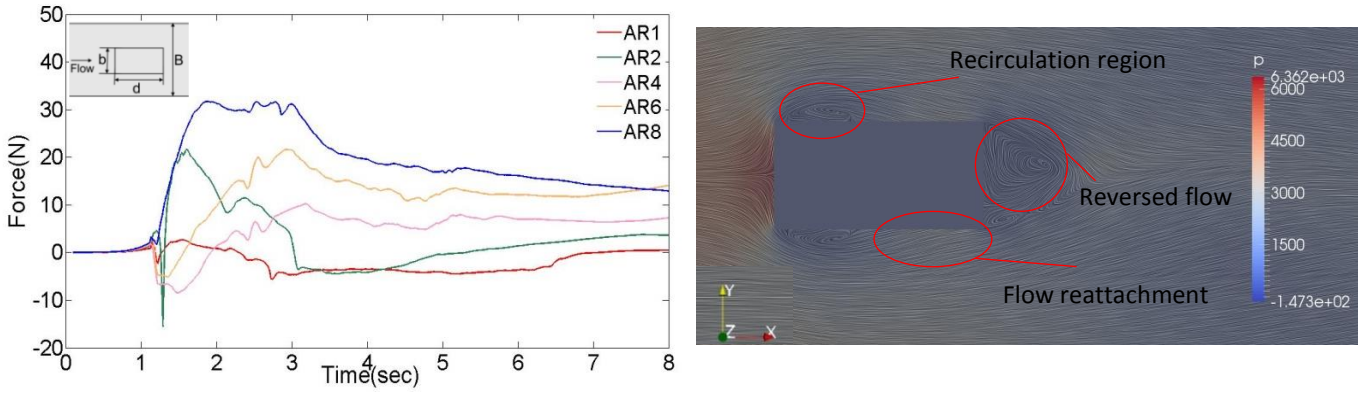

Figure 3.13: a) Time histories of friction drag forces for columns with AR1, AR2, AR4, AR6 and AR8 for $h_u = 1000mm$ b) Streamlines of flow around the column AR1:2 , 10 cm above the channel bottom at t=4.sec

3.5.2.2 Vertical pressure distribution

Since the pressure difference in the upstream side and leeside of the column contributes considerably in drag force, the vertical pressure distribution is important to be investigated in more depth. Figure 3.14 shows the vertical distribution of the pressure at the upstream side of the columns. For simplicity, AR1:1, AR1:4 and AR1:8 are presented and compared here because pressure distributions show similar trend for other aspect ratios. As the distance from the flume bottom increases, the pressure decreases. The pressure evolution demonstrates the transition from impulsive highly turbulent pressure at the impact moment to quasi-steady pressure at 6.0 sec. At 1.3sec, after the bore leading edge slammed on the column, the impulsive pressure occurred. At this time the bore height is

low while the bore velocity is high which leads to high impulsive pressure. As shown in Figure 3.14 a, the initial impact only affects the lower elevations of the column around 10cm. For upper elevations, the pressure is almost zero for all cases. At 2.3sec, when the bore collapsed back to the upstream onto the incoming bore, the pressure rapidly increases in the upper levels. This local rise which can be observed in Figure 3.12 is attributed to the reflection phase (transient force). After 2.3sec, the pressure distribution is gradually reaching to quasi-steady condition with the behavior analogous to the hydrostatic pressure, as it can be observed from Figure 3.14c and d. Therefore, the contribution of the dynamic pressure in the total pressure is considerable at the first moments of impact and after that, hydrostatic pressure is mostly dominant.

The observation of pressure distribution on the leeside of the column is presented in Figure 3.15. Until 3.2 sec almost no noticeable value for the pressure occurred at the leeside since the bore height is low and the region is almost dry. After 3.2 sec, the pressure slightly increased for AR1:1 at the lower elevations of the column, however, the pressure values for other cases are approximately zero. At 6.0 sec, the pressure value at the leeside of AR1:1 column is noticeable but it is still near stagnation pressure for AR1:8.

This is because as the bore impacts the column, separation occurs due to square column sharp edges; therefore, the bore splits to two streams reaching farther at the downstream side. After the bores converge in the wake of the structure, the so-called "rooster tail" with triangular shape forms. Figure 3.16 compares the bore evolution around the column at several key moments. Approximately around 2.0 sec, for both *AR*'s, the bore converged in the wake of the structure and formed the rooster tail. The bore at this area is highly turbulent and was also observed during experimental tests (Arnason et al. 2009, Nouri et al. 2010). However, as displayed in Figure 3.16, the bore in the wake of *AR*1:1 merged earlier than *AR*1:8. The width of the formed rooster tail is approximately equal to the structure width for both *AR*'s but its length is longer for *AR*1:8. After 6.0 sec the bore merged and filled the column leeside for *AR*1:1 but for *AR*1:8 the bore was not reached at the leeside yet and the stagnation area is distinct since the velocity is still low and the column leeside is almost dry. Therefore, as shown in Figure 3.15, the pressure at the leeside of the *AR*1:8 column is close to zero. However, the value of pressure at the *AR*1:1 leeside is 1.5kPa and is almost negligible with respect to the total pressure

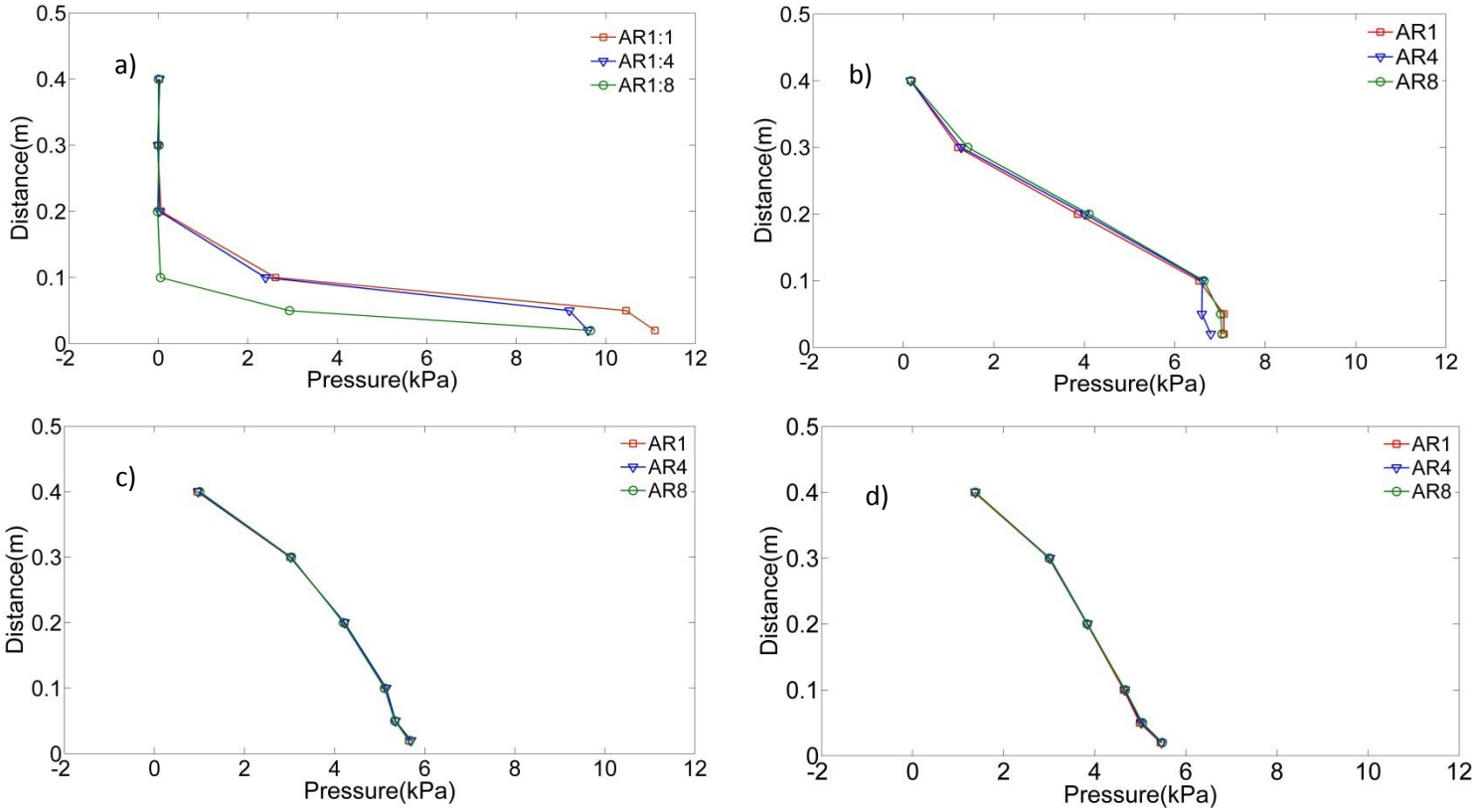

Figure 3.14: Vertical variation of pressure at front side of the column with AR1,AR4 and AR8 for 850mm impounded water after a) 1.3sec b) 2.3sec c) 4.0sec d) 6.0sec

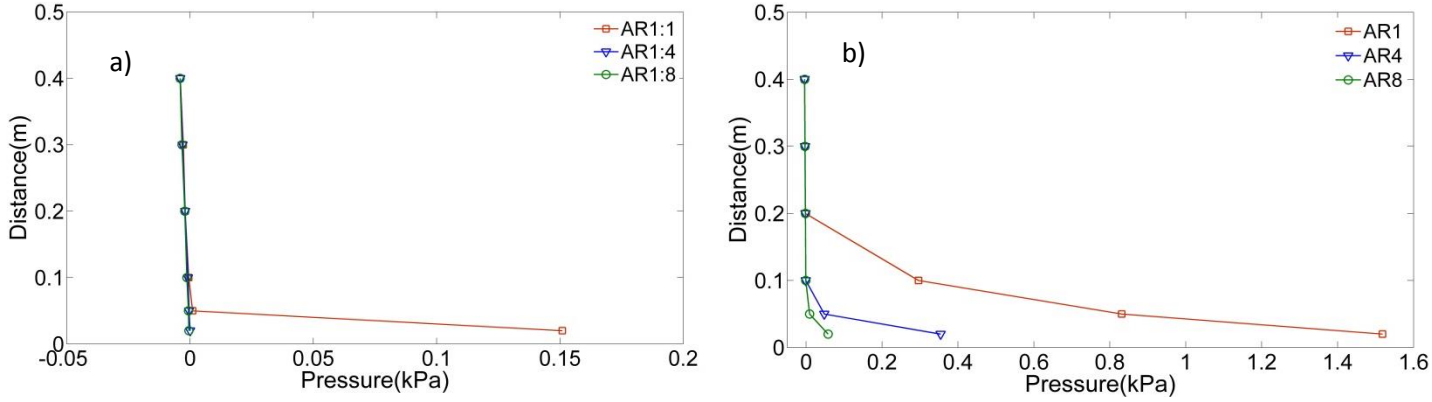

Figure 3.15: Vertical variation of pressure at leeside of the column with AR1, AR4 and AR8 for 850mm impounded water after a) 3.2 sec b) 6.0 sec

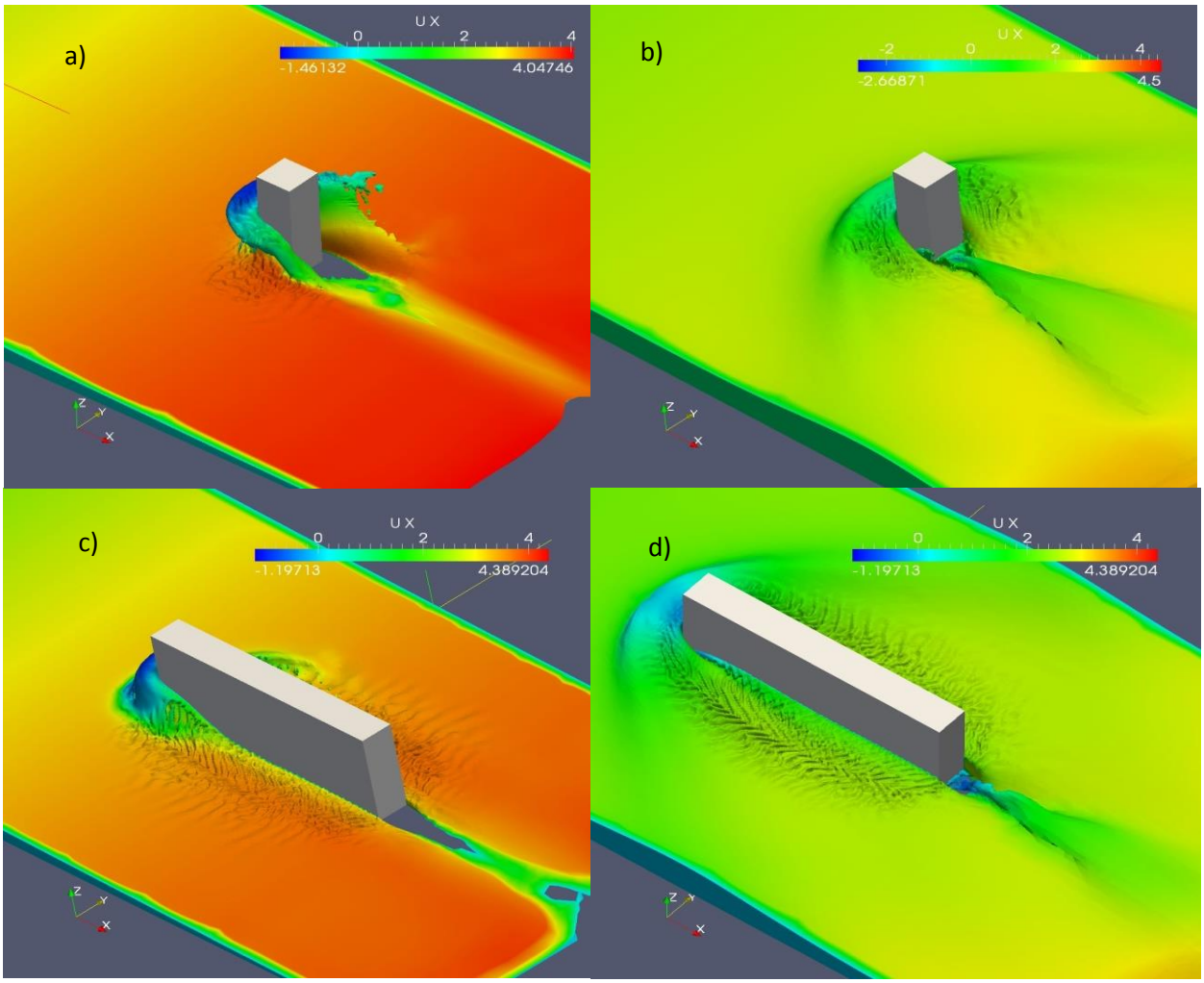

Figure 3.16: Formation of rooster tail for AR1:1 a) 2.1sec b) 6.0sec AR1:8 c) 2.1sec d) 6.0sec

Overall, based on these observations, neither contributing factors (pressure difference and friction drag) had substantial effects on increasing the bore stream-wise force by increasing AR. As a result, for the tested ARs ranging from AR1:1 to AR1:8, a slight rise in the net stream-wise force was obtained.

3.5.2.3 Drag Coefficient

The time history of drag coefficient can be observed in Figure 3.17 for elongated columns with different aspect ratios. The cases for $h_u = 550\text{mm}$ and $h_u = 1000\text{mm}$ are presented in Figure 3.17. For all aspect ratios, the time histories of drag coefficient follow the similar trend. For the cases $h_u = 550\text{mm}$ and $h_u = 850\text{mm}$, the spike was observed at the initial impact. The

corresponding drag coefficient for the initial impulsive force is estimated as C_d=2.75 and C_d=2.6 for $h_u = 550\text{mm}$ and $h_u = 850\text{mm}$, respectively. This spike during impulsive force has not occurred for the higher impounded water depths. Yeh (2007) suggested C_d=3.0 at the initial impact based on the observation in the literature which shows that the initial impact exceeds about 1.5 times the subsequent hydrodynamic force. After the initial impact, the trend is almost similar for all cases.

It is also evident that C_d gradually decreases by increasing the impounded water depth. The same trend was also reported by Arnason (2005). Furthermore, for the different cases of aspect ratios, since the hydrodynamic force increases, C_d also increases which results in marginally higher aspect ratio. The variation of C_d with respect to *AR* and h_u is presented in Table.1 ignoring the initial force spike. The comparison between *AR*1:1 to *AR*1:8 shows that C_d values increased about 0.1 by increasing impounded water depths. The mean drag coefficient is calculated between the impact time (t_i) and the time when the reservoir is starting to deplete (t'). The beginning of the depletion occurred usually after 6.0 sec but it may differ for each simulation. The mean C_d varies between 1.68 to 1.91 for all impounded water depths and aspect ratios.

These results are also compatible with C_d values obtained by Arnason's (2005). He reported average C_d ranging from 1.99 to 2.26 for the square column for h_u between 100mm to 300mm. The results also shows that the adopted value for C_d=2.0 by FEMA P646 (2012) for the square column and the elongated column at this examined range (AR1:1 to AR1:8) is reasonable.

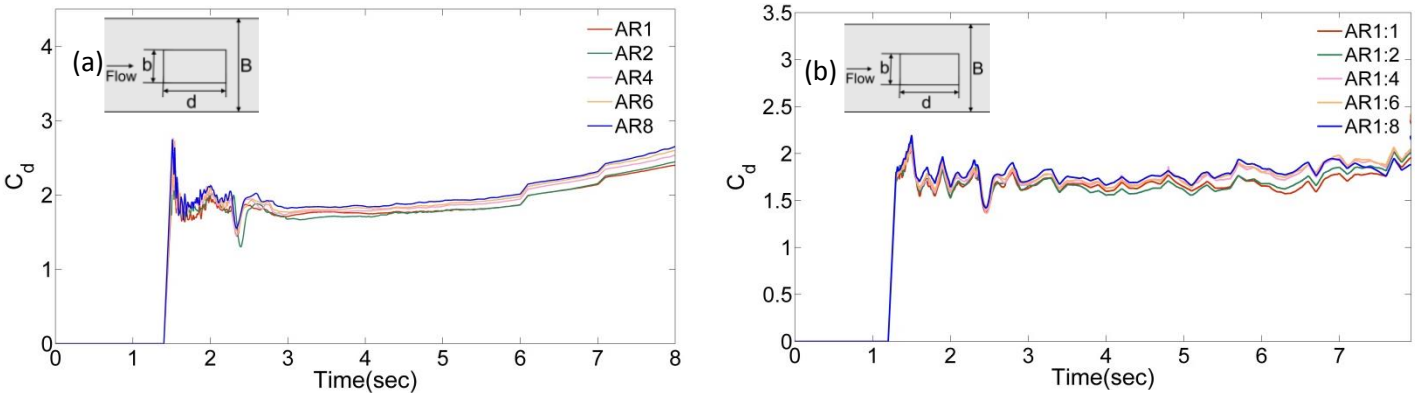

Figure 3.17: Time history of drag Coefficient for different impounded water a) $h_u = 550mm$ b) $h_u = 1000mm$

Table 3-1 Drag coefficient for different impounded water and rectangular column shapes.

Aspect ratio	Mean C_d ($h_u = 1.0$ m)	Mean C_d ($h_u = 0.85$ m)	Mean C_d ($h_u = 0.55$ m)
Square	1.68	1.74	1.80
Column AR2	1.67	1.72	1.78
Column AR4	1.72	1.80	1.84
Column AR6	1.74	1.83	1.87
Column AR8	1.77	1.87	1.91

3.5.3 Rectangular walls with different aspect ratios

The impact mechanism of the tsunami bore with a rectangular wall is clearly different from rectangular columns. Generally, they produce higher hydrodynamic force as the column width normal to the direction of flow increase. In addition, most research works, conducted on the impact of the tsunami bore with rectangular walls, measured significant values of transient force during the reflection phase (Kihara et al. 2015 , Linton et al.,2013). Therefore, the associating drag coefficient induced by a rectangular wall could be affected and should be taken into careful consideration. For this reason, rectangular walls with AR2:1 and AR4:1 were also examined and the results are presented in this section. Two impounded water depths, $h_u = 550$mm and $h_u = 1000$mm, were selected for these cases. The subsequent hydrodynamic force and drag coefficient are then estimated using the similar scaled up domain with $BR = 0.07$. Figure 3.18 displays the net stream-wise force and associating drag coefficient time histories for square and AR2:1 and AR4:1 for $h_u = 1000$mm.

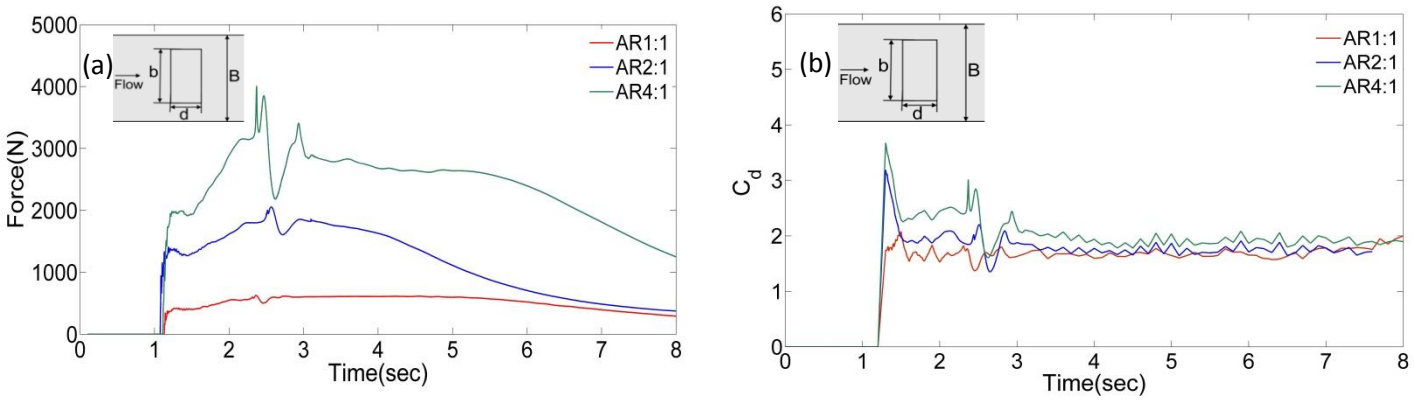

Figure 3.18: Rectangular-section walls with different aspect ratios a) Time history of net stream-wise force for $h_u = 1000$mm b) Time history of Drag Coefficient for $h_u = 1000$mm

The overall trend indicates that the hydrodynamic force is increased by 40% from AR2:1 to AR4:1. As shown in Figure 3.18a, four distinct zones are appeared in the resulting force time histories including impulsive force, transient force peak, reduction in transient force and hydrodynamic force. In addition, another significant reduction in hydrodynamic force can be seen after the transient force peak. This can be attributed to the corresponding low pressures which mostly occur when the entrapped air is expanded and compressed during the impact process (Bullock et al., 2007). The reduction in the transient force is less than 50% of the peak transient force. As displayed in Figure 3.18, the transient force occurred around 2.3 sec overshoots significantly the subsequent hydrodynamic force. This was also observed by Linton et al.'s (2013) experimental work. The authors reported that the value of transient force was 2.2 times the mean hydrodynamic force. In the current study, the ratio of peak transient force to subsequent mean hydrodynamic force was found to be less than 1.45.

The wall was extended through the whole width of the channel in Linton et al.'s (2013) work; therefore, the reflection process is more intense in terms of higher turbulence and hydrodynamic effects. However, in the present study, some parts of the flow were reflected and falling back onto the incoming bore after the impact while the remaining parts moved around the wall into the downstream. This difference during reflection phase leads to discrepancies in resulting transient forces. The associating drag coefficient is performed and the resulting values are estimated.

Table 3-2 presents the obtained mean drag coefficient (C_d) for rectangular-section walls. Unlike the rectangular-section columns, C_d increases by increasing h_u for rectangular walls.

Table 3-2 Drag coefficient values for different rectangular wall shapes

Aspect ratio	Mean C_d ($h_u = 1.0$ m)	Mean C_d ($h_u = 0.85$m)
Column AR2:1	1.80	1.70
Column AR4:1	2.05	1.92

3.5.4 Influence of orientation for square and rectangular columns

3.5.4.1 Net stream-wise force

In this section the effects of different structural orientation with respect to its original alignment (α) on the net stream-wise force is investigated. Further, the drag coefficient is computed for each orientation. The time history of net stream-wise force exerted on the square column with different orientation is presented in Figure 3.19 for the case of 1000mm impounded water depth. For $\alpha = 22.5°$ and $\alpha = 67.5°$ the resulting force time histories are almost the same. As it can be observed from Figure 3.19, the values of impulsive force and hydrodynamic force vary as the structure orientation changes with respect to its initial alignment ($\alpha = 0°$). The impulsive force, which occurred around 1.2 sec, had lower values by increasing the structure orientation. For the case of $\alpha = 0°$, the impulsive force increased about 36% relative to the case $\alpha = 45°$. This occurred due to the sharp edge of column for the case $\alpha = 0°$ facing the incoming bore. For the case of $\alpha = 45°$ the lowest impulsive force occurred since the corner edge of the square column faces the flows therefore, flow moved around the column more smoothly. The transient force occurred after 2.3 sec showing greater values for cases $\alpha = 0°$ because the higher water level rose behind upstream side of the column. This did not occur for $\alpha = 45°$ as bore passed around the column with no evidence of reflection and subsequent water build-up behind the upstream side of column was observed. On the other hand, the maximum hydrodynamic force occurred for $\alpha = 45°$ structure orientation. This is because by increasing the column orientation the projected width (b' in Figure 3.19) to the flow

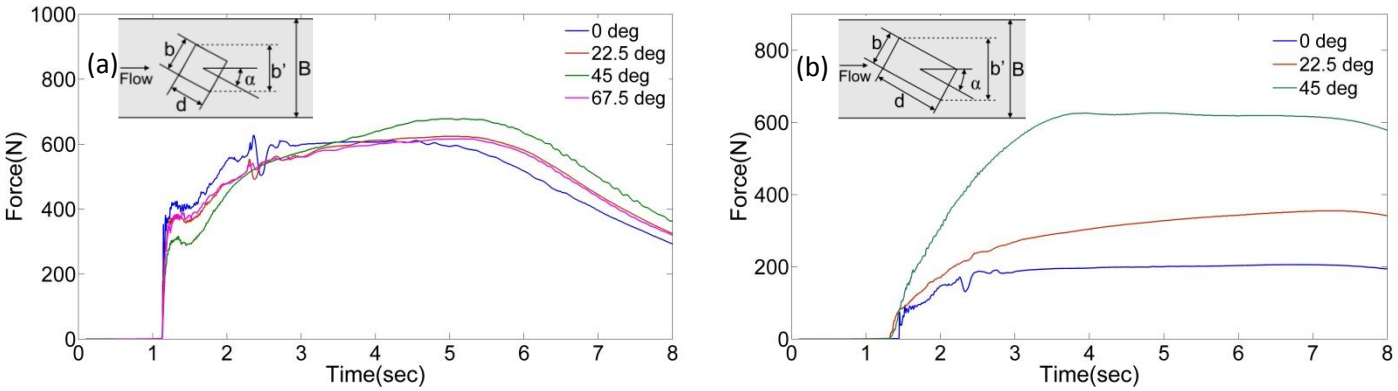

Figure 3.19: Time history of net stream-wise force for columns with different orientation a) Square h_u= 1000mm b) Rectangular h_u = 550mm

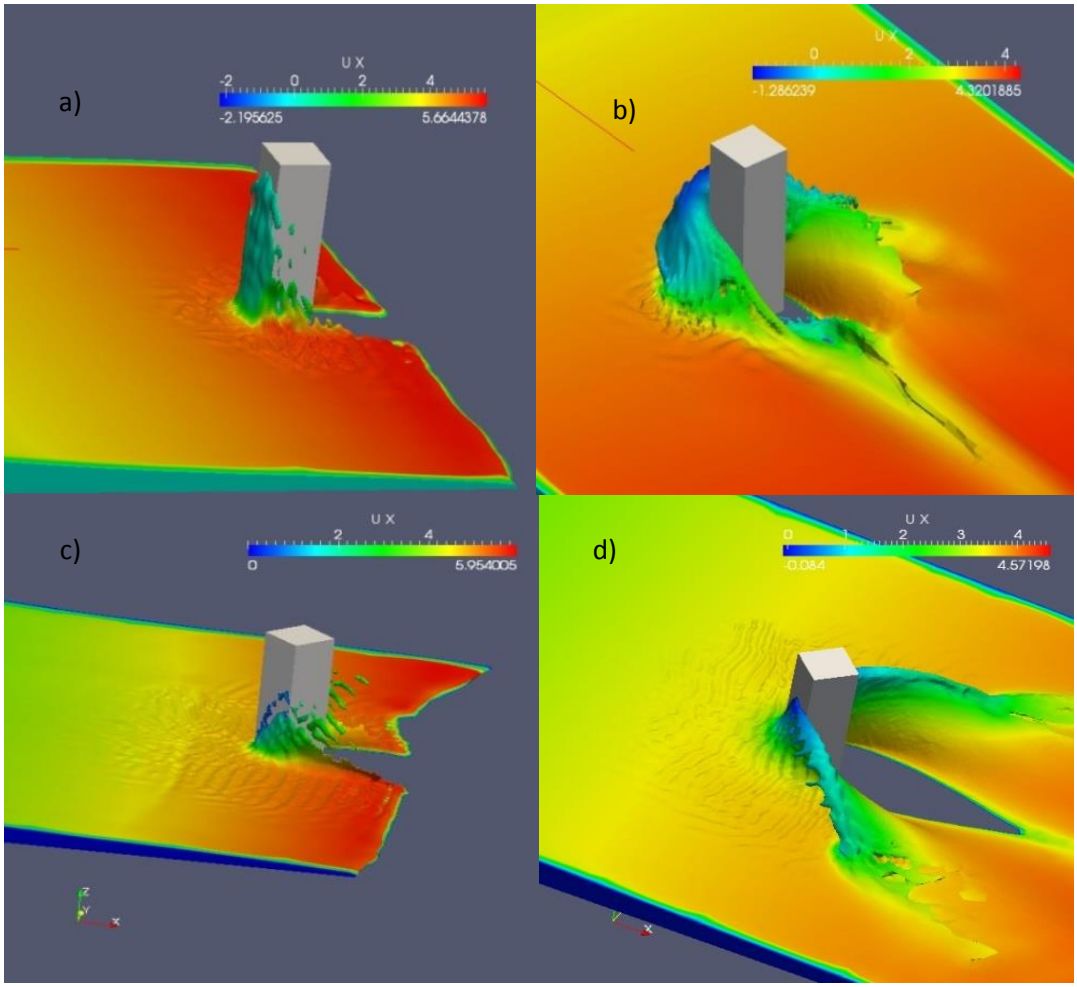

Figure 3.20: Snap shots of key moments during initial impact and transient phases of square with structure orientations of α= 0° at a) t=1.3sec b) t=2.3sec and α= 45° at c) t=1.3sec d) t=2.3sec

direction increases and consequently the hydrodynamic force increases. For cases $\alpha = 22.5°$ and α=67.5° the hydrodynamic force is slightly greater than $\alpha = 0°$ as b' is slightly higher.

For better understanding the variations of resulting force in Figure 3.19, the qualitative comparisons of water surface at some key moments are presented in Figure 3.20. In this figure, the water surface profiles are illustrated during the impact and transient phase for cases $\alpha = 0°$ and $\alpha = 45°$.

In Figure 3.20a, the bore run-up on the upstream face of the column can be clearly observed; however, in Figure 3.20b, no run-up can be observed as the flow is divided into two streams by the corner edge facing the incoming bore. Further, during transient phase (Figure 3.20c and d), the difference between the cases α= 0° and α=45° can be noticed. The surface-roller formed by the bore reflection from the upstream side of the column for the case α=0° which leads to growing of water surface level behind the upstream face and consequently higher hydrodynamic force relative to the case α=45°. Similar results were obtained by Shafiei et al.'s (2016) experimental work. They investigated the structure orientation influence on the resulting force exerted on the square column with orientations α=0°, α= 30° and α= 45°. The highest initial impact force and hydrodynamic force obtained by their experimental works for α=0° and α=45°, respectively. Arnason (2005) also reported higher hydrodynamic force for the case of α=45° with the ratio less than √2 comparing with the case α=0°.

3.5.4.2 Column drag coefficient

The time histories of drag coefficient for all structure orientations are presented in Figure 3.21. The estimated C_d for square and rectangular column with *AR*1:4 are presented for different values of α. No observation of initial impulsive force can be obtained.

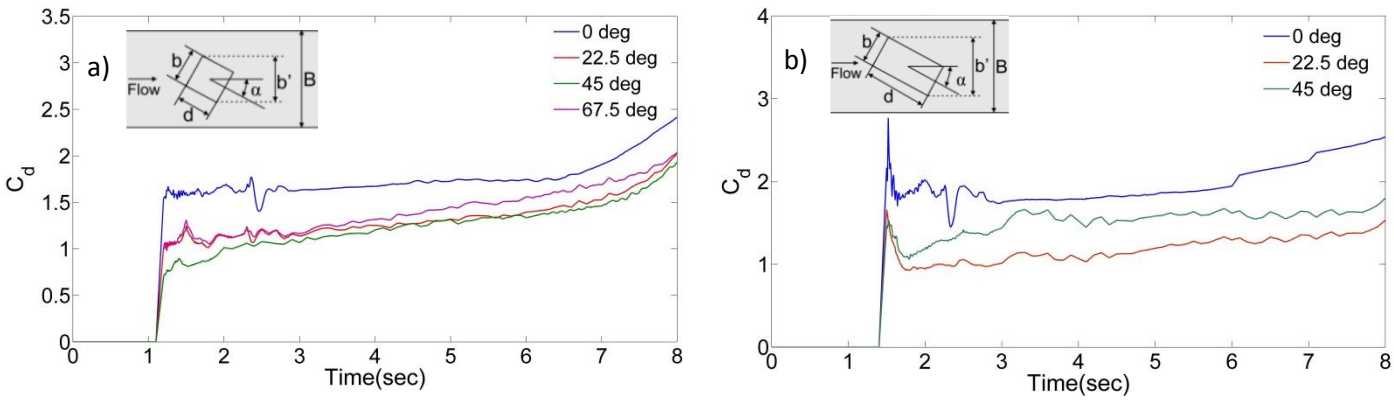

Figure 3.21: Time history of drag coefficient for square column with different orientations a) $h_u = 1000\text{mm}$ b)$h_u = 550\text{mm}$

The mean drag coefficient is presented in Table 3 for square columns with different orientations. The value of C_d decreased as α increased, therefore, the lowest value of C_d was obtained for α=45°.

Table 3-3 Drag coefficient for different structure orientations

Square	Mean C_d ($h_u = 1.0$ m)	Mean C_d ($h_u = 0.85$ m)
$\alpha = 0°$	1.68	1.74
$\alpha = 22.5°$	1.37	1.30
$\alpha = 45°$	1.32	1.24
α=67.5°	1.41	-

Similar to rectangular section columns with varying *AR*, higher value of C_d was obtained by increasing h_u. Shafiei et al. (2016) observed the same trend based on their experimental results. The authors reported the C_d with values 1.15, 1.40 and 1.65 for $\alpha = 0°, \alpha = 30°$ and $\alpha = 45°$, respectively. However, for the obtained C_d values, the contribution of the hydrostatic force was excluded. Moreover, the drag coefficients were obtained for the bore depth of 210mm at the location of the structure which differs from examined impounded water depth at the present study.

Furthermore, Arnason (2005) reported C_d values ranging from 1.72 to 2.22 for the case of $\alpha = 45°$. These aforementioned values for C_d is consistent with the present work as higher values of C_d is expected by increasing h_u. On the other hand, the drag coefficient obtained for the case of the rotated column with AR1:4 are presented in Table 3-4. The value of C_d is increased by increasing the structure orientation. The obtained C_d for this case does not follow a general rule. The estimated mean drag coefficient is almost the same for different h_u.

Table 3-4 Drag coefficient for different structure orientations

*AR*1:4	Mean C_d ($h_u = 1.0$ m)	Mean C_d ($h_u = 0.55$ m)
$\alpha = 22.5°$	1.14	1.12
α=45°	1.47	1.49

3.5.5 Comparison of drag coefficients with respect to Reynolds number

In this section, the relation between C_d and Reynolds numbers (Re_f ,flow Reynolds number and Re_o , object Reynolds number) are presented for all cases. The flow Reynolds number (Re_f) is defined as

$$Re_f = \frac{uh}{\nu} \tag{3-21}$$

where h and ν are bore velocity, bore depth and kinematic viscosity, respectively. The values of u and h are taken from the unobstructed flow condition at the time that maximum hydrodynamic force occurred.

The object Reynolds number is defined as

$$Re_o = \frac{ub}{\nu} \tag{3-22}$$

where b or (b' for rotated cases) is the projected width to the flow direction. The comparison of the variation of C_d with respect to flow Reynolds number (Re_f) is illustrated in Figure 3.22a for different orientations of *AR*1:4 rectangular-section column. The results show that the value of C_d is almost independent of Re_f increase; however, a slight decrease of C_d can be observed as Re_f increased for the case of AR1:4. In contrast, for the rectangular-section wall (*AR*4:1) the value of C_d is increasing

by increasing Re_f . The lowest C_d occurred for $22.5°$ rotated column with *AR*1:4, while the highest C_d occurred for the rectangular wall. In Figure 3.22b the Reynolds numbers of different object (Re_o) with various shapes are compared versus drag coefficients.

The obtained drag coefficients vary between 1.12 to 2.05. The general trend shows almost independency of the drag coefficient from the Object Reynolds number. The maximum increase (0.12) in the value of C_d occurred for the rectangular wall with *AR*4:1 as the bore depth increased. A slight decrease in C_d for a stronger bore is evident in Figure 3.22b for the rectangular-section columns with *AR*1:1 and *AR*1:4 as well as rotated square columns. Based on these observations, C_d values increased for rectangular-section walls as the bore depths increased. On the other hand, for rectangular-section columns, C_d values decreased as the bore depth increased.

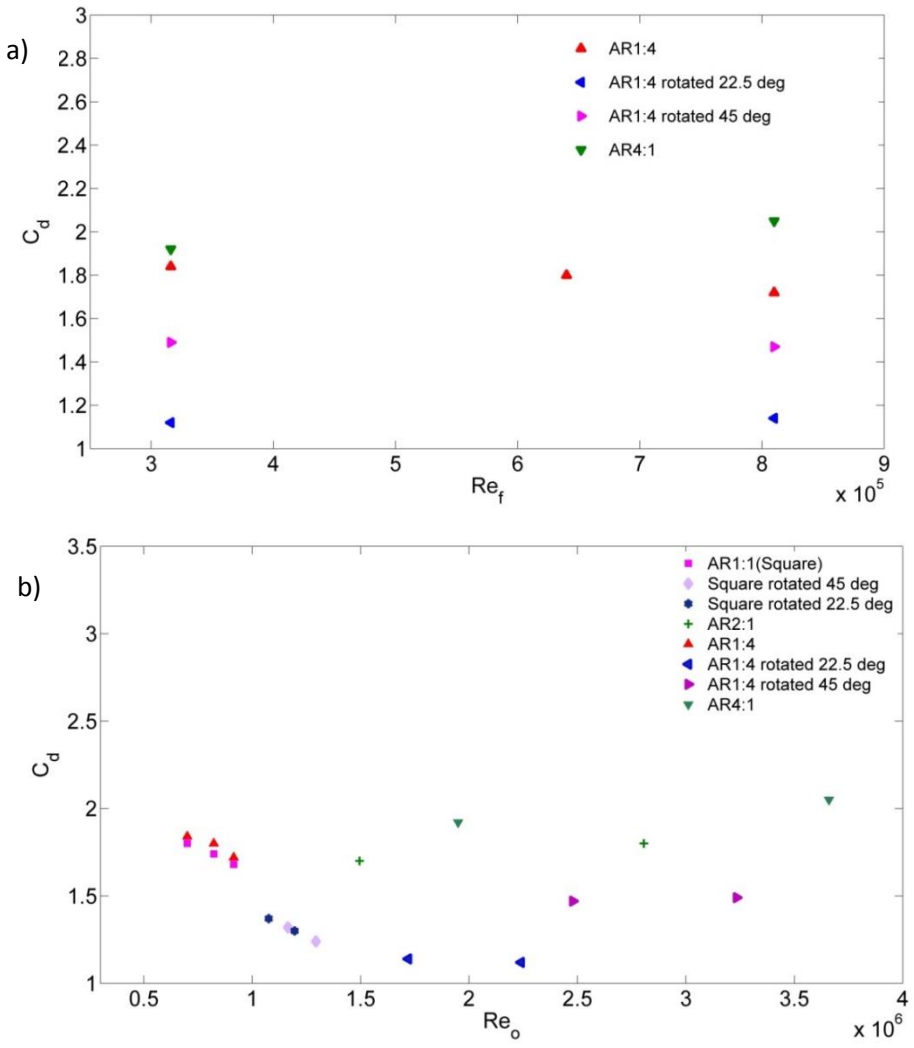

Figure 3.22: a) Flow Reynolds number (Re_o) vs. C_d b) Object Reynolds number (Re_f) vs. C_d

3.6. Conclusion

In the present work, the interactions between rectangular-section structures (different aspect ratios and orientations) with tsunami-like bores were investigated and associated drag coefficients were determined. The dam-break analogy with tsunami like bores was employed using three-dimensional numerical models implemented in OpenFOAM. First, the numerical model (using RANS equations with realizable k-ε turbulence model) was validated by experimental results of physical experiments conducted in NRC-CHC in Ottawa. In order to eliminate the side wall effects of the numerical simulations on the results, a scaled-up domain was selected using a proper blockage ratio. Then,

several dam-break simulations for different column aspect ratios of rectangular-section column (*AR*= 1,2,4,6 and 8) and walls (*AR*=2 and 4) were conducted. The effects of structural orientations (α= 0◦, 22.5◦ and 45◦) were also investigated for the square column (AR1:1) and AR1:4. The drag coefficient for each case study was derived using obtained stream-wise forces, water surface elevations and flow velocity.

FEMA P646 (2012) only suggests a drag coefficient value for the square column (Cd=2) and does not provide any information for elongated or rotated columns. The present works provided thorough investigations on drag coefficients for elongated and rotated structures. The obtained mean drag coefficient range for rectangular-section column with (*AR*= 1,2,4,6 and 8) varies from 1.68 to 1.91. As the aspect ratio increases, the resulting mean drag coefficients increase. Lower value of drag coefficients are obtained for higher bore depth. For rectangular section walls (*AR*=2 and 4), the obtained drag coefficients are from 1.7 to 2.05. In addition to the wall geometry contribution (aspect ratio of the wall) in drag coefficients, the simulations showed that higher bore depths resulted in higher drag coefficients for walls. Among rotated square columns, the 45° rotated column resulted in lowest drag coefficient.

In the present study, only rectangular-section columns and walls have been investigated; however, more complex structure geometries like circular and elliptical structures and their orientations can be the subjects of further studies. Moreover, a wider range of the bore depths and their effects on the drag coefficient need to be examined.

Chapter 4. Numerical modeling of circular structures impacted by Tsunami forces and the effects of bed condition using OpenFOAM

4.1 Introduction

Recent tsunami events showed that these phenomena can be devastating and cause catastrophic human loss as well as vast damage in coastal infrastructures. The 2011 Tohoku tsunami induced by subduction earthquake (M_W 9.0) resulted in around 20,000 fatalities and 264,468 partially collapsed or fully collapsed buildings. It was reported by the government of Japan as one of the most expensive natural hazards with the damage cost over $217 billion. The inundation height ranging from 10m to 38m while a maximum run-up height of around 41 m was reported (EERI, 2011). Mikami et al. (2012) conducted a field survey after 2011 Japan Tsunami and reported extensive reinforced concrete building damage in coastal areas. The tsunami intruded several kilometers inland where not enough high ground sites in the region for evacuation. Yeh (2013) reported that the major reasons of extensive structural damage during 2011 Japan Tsunami were unexpected inundation depth, scouring effects , high bore velocities and buoyancy forces.

Based on these evidences, the essence of revising and developing a building guidelines for designing against tsunami loading was revealed. The present paper is a part of an ongoing interdisciplinary research program which was started at the University of Ottawa in order to improve the design guidelines for estimating tsunami-induced forces. One of the major factors on bore propagation characteristics is the effects of bed conditions. As tsunami waves are generated by abrupt vertical motion of the seabed in the deep water, one or series of waves form. These waves advance towards the coastal areas and once they reach the shallow water areas, owing to shoaling effects, break into series of turbulent bores and eventually intrude the inland regions as a hydraulic bore. Generally, the first tsunami wave propagates over dry lands (dry bed condition) while the subsequent waves may

intrude the flooded coastline before full recession of the first wave (wet bed condition). Pervious research showed that the water layer presence on the bed could affect the tsunami bore characteristics. In addition, the bed condition (smooth versus rough) also affects the bore propagation and resulting forces acting on the coastal structures.

In the present study, a three-dimensional multiphase numerical model is applied to study the tsunami bore impact on surface-piercing structures. Chanson (2006) demonstrated that the tsunami induced wave and dam break waves are similar in characteristics. The experimental setup performed by Nouri et al. (2010) is used to validate the efficiency of numerical model. Dam-break approach is used in order to generate hydraulic bore. In this approach the still water behind the gate is released suddenly. The main objective of this study is to investigate and analyze the effects of bed conditions (wet, dry, smooth and rough) on velocity fields, bore depths and resulting pressure and forces exerted on structures. The flow around circular and elliptical columns are studied and analyzed. Moreover, in order to respect the similarity between the model and the real world prototype, the numerical model is scaled up. To do so, the model sidewalls are moved away so that they no longer affect the resulting force due to blockage effects.

In Section 4.2, a brief literature review on similar studies of bore and structure interaction is presented. In Section 4.3, the governing equations and numerical model are introduced. The comparison between numerical results and laboratory measurements is performed for force, pressure and bore surface elevation in Section 4.4. In Section 4.5, the scaled up computational domain is used to simulate the bore structure interaction and the obtaining force, pressure, velocity fields and bore surface elevation is presented. Finally, in Section 4.6, conclusions and suggested future works are presented.

4.2 Literature review

Since the current paper scope is the tsunami-like bore-structure interaction, some relevant numerical and experimental works in the literature are presented here. Numerous studies have been done on both submerged and free surface flows around circular columns for steady and unsteady flows. A laboratory experiment was performed by Dargahi (1989) to investigate the turbulent flow around a vertical circular column. A numerical study using the large eddy simulation (LES) was performed by Kawamura et al. (2002) to study the flow moving around a free surface piercing circular column in

order to investigate the effects of different values of Froude number (Fr = 0.2, 0.5 and 0.8). Yu et al. (2008) later examined the different range of Froude number between (Fr=1 to 3) and Reynolds numbers using the two-phase LES numerical approach. The authors reported that the drag force increased by increasing Reynolds number and decreased slightly by increasing Froude number. Sadeque et al. (2008) studied the hydraulic of flow around a circular structure in an open channel experimentally. The authors examined the effects of different level of submergence as well as a surface-piercing structure on the resulting bed shear stress and vortex shedding formation in the wake of the structure.

Extensive studies have been performed to investigate the dam-break wave interactions with the surface-piercing structures on both dry and wet bed conditions. A laboratory experiment conducted by Ramsden (1996) at two separate wave tanks to study the turbulent bore interaction with a vertical wall. Bores and surges on dry and wet bed were generated by releasing a water volume using a pneumatic gate with the downstream depth of $h_d = 0$ and $h_d = 0.0028$ m, respectively. A comparison between a dry and wet bed conditions demonstrated that the bore depths, run-ups and forces acting on vertical walls for the wet bed condition exceeded the dry bed. The author also reported that the Cross (1967) theory underestimated the force exerted on the wall by approximately 20-50%. Arnason (2005) studied the broken tsunami bore interaction with different cross-section structures. The initial downstream depth was considered ($h_d = 0.02$ m) for all examined cases. For circular columns, three different diameters were examined as 29 mm, 60.6 mm and 140 mm for small, intermediate and large, respectively. These columns were used to study the effects of blockage on this experimental setup. Based on the author's results, the obtained forces are lower for the column with smaller diameter. Moreover, the wake effects and run-up heights are minimal for the smaller circular columns. For the case of large circular column, the author reported that the hydrodynamic force overshoots significantly the initial impulsive force especially for higher bore depths. This is attributable to the higher water surface build up behind the larger circular column.

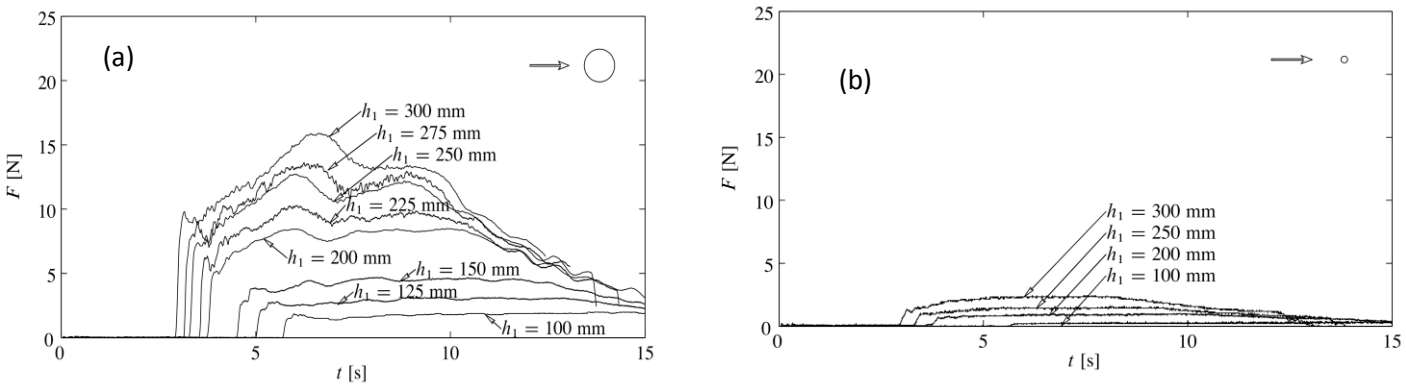

Figure 4.1 Net stream-wise force histories for the circular columns a) Large b) Small [Arnason (2005)]

Many numerical studies have also investigated the influence of the bed conditions for tsunami bore impacts on structures. Gomez-Gesteira and Dalrymple (2004) studied the dam break wave interaction with a tall vertical structure using smooth particle hydrodynamics (SPH) method. The resulting force and velocities were validated successfully with experimental measurements. The effects of downstream wet and dry bed conditions on the bore propagation were analyzed. As it can be observed in Figure 4.2, for the dry bed condition, the maximum force exerted on the column occurred at the elevations less than 10cm. On the other hand, for the wet bed condition the maximum force occurred at the elevations between 10cm and 20cm.

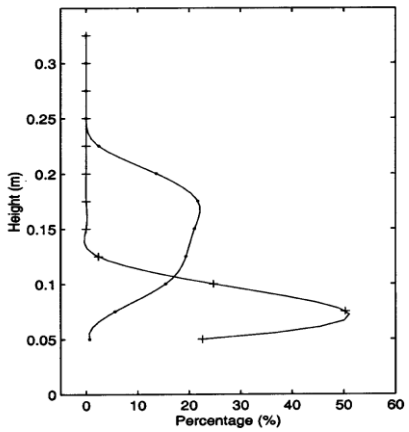

Figure 4.2: Vertical distribution of force acting on the upstream side of the structure. Wet bed (crosses) and dry bed (circles). [Gomez-Gesteira and Dalrymple (2004)]

Leal et al. (2006) performed series of experimental tests to investigate the magnitude of dam-break bore front celerity for different bottom frictions and downstream bed conditions (wet or dry). The

authors argued that the bore front celerity decreases as the ratio of h_d/h_u increases until the bore front celerity no longer changes with the increase in h_d. The results also demonstrated good agreement with the Stoker's (1957) analytical solution. Crespo et al. (2008) investigated the dam-break bore evolution over wet and dry beds using two-dimensional SPH method. The authors introduced two dissipation mechanisms including wave breaking and bottom friction as major factors causing dissipation over wet and dry bed conditions, respectively.

St-Germain et al. (2012) studied the tsunami-like bore structure interactions advancing on the wet and dry bed conditions using the SPH method. The authors aimed to investigate the bore propagation characteristics and understand the resulting hydrodynamic force, velocity field and bore depth for dry ($h_d \cong 0$) and wet bed ($h_d = 0.008\text{m}$) conditions. Based on their results, the bore front celerity was remarkably smaller for the wet bed case due to the resistance imposed by the water layer in downstream. However, the resulting force acting on the column was larger for the wet bed condition.

Douglas and Nistor (2014) studied the effect of bed conditions (dry ($h_d \cong 0$) and wet ($h_d = 0.005\text{m}, h_d = 0.02\text{m}$ and $h_d = 0.05\text{m}$) during the interaction of tsunami-like bore with square structure using a three-dimensional multiphase numerical model. The results showed a substantial change in bore characteristics as the downstream bore depth (h_d) increased. The authors observed deeper and steeper bore front for wet bed conditions; however, the shape of the bore front was not changed substantially as the downstream depth increased.

Wei et al. (2015) studied the dynamic interaction of bore with bridge piers using SPH method. The results showed that the dimensionless width of the flume is proportional to the hydrodynamic force and bed shear stress.

4.3 Numerical method

4.3.1 Description of OpenFOAM

In order to solve three-dimensional Reynolds Averaged Navier-stokes equations (RANS), OpenFOAM (Open Field Operation and Manipulation) includes a solver called *interFoam* for incompressible two-phase flow. Solvers represent solution algorithms and Partial Differential Equations (PDEs) developed to deal with the relevant continuum mechanics problems. The RANS equations can be applied to a variety of coastal problems. The Finite Volume Method (FVM) is

implemented in order to discretize the governing equations. The *interFoam* solver tracks the water surface elevation using the Volume of Fluid (VOF) method. Since the program language, C++, is object orientated and the code and mathematical syntax are mostly similar, it provides a user friendly environment for modification and development of the source code.

4.3.2 Governing equations

The RANS equations which contain mass conservation and momentum equations for incompressible fluids is used by OpenFOAM and expressed by (Rusche, 2002)

$$\nabla \cdot \mathrm{U} = 0, \tag{4-1}$$

$$\frac{\partial \rho \mathrm{U}}{\partial \mathrm{t}} + \nabla \cdot (\rho \mathrm{UU}) - \nabla . (\mu_{\mathrm{eff}} \nabla \mathrm{U}) = -\nabla \mathrm{p} + \nabla \mathrm{U} . \nabla \mu_{\mathrm{eff}} - \mathrm{g} . \mathrm{X} \nabla \rho + \sigma \kappa \nabla \alpha \tag{4-2}$$

where ρ, U, p ,g , X, σ, κ and α are the density, the velocity vector, the pseudo-dynamic pressure, the gravity acceleration, the position vector, the surface tension coefficient and the interface curvature and indicator function respectively. The bolded components represent vector field and κ is defined as

$$\kappa = \nabla \frac{\nabla \alpha}{|\nabla \alpha|} \tag{4-3}$$

The effective dynamic viscosity μ_{eff} is defined as

$$\mu_{\mathrm{eff}} = \mu + \rho \upsilon_{\mathrm{turb}} \tag{4-4}$$

where υ_{turb} and μ are the turbulent kinetic viscosity and molecular dynamic viscosity, respectively.

The terms in Eq.4-2 are specified in a feature that the terms on the left hand side of Eq.4-2 are considered to build the coefficient matrix and those on the right hand side are used as an independent terms of equations. (Higuera et al. 2013)

In order to capture the free surface elevation, the volume of fluid technique is implemented in OpenFOAM. This method simplifies measuring complex free surfaces and is computationally less expensive. An indicator phase function (α) is defined to measure the occupied volume per unit of

each mesh cell (Berberovic et al. 2009). At the present study, a two-phase flow (water and air) is presented; therefore, $\alpha = 1$ indicates that the cell is filled with water and $\alpha = 0$ indicates that the cell is empty and finally the values between 0 and 1 represent the interface. Each property of the fluid ($\emptyset$) can be measured by weighting them using the VOF method.

$$\emptyset = \alpha\, \emptyset_{\text{water}} + (1 - \alpha)\emptyset_{\text{air}} \tag{4-5}$$

An additional advection equation should be solved in order to track the water surface movement which is described by

$$\frac{\partial \alpha}{\partial t} + \nabla.(U\alpha) + \nabla.U_c\, \alpha(1 - \alpha) = 0 \tag{4-6}$$

where U_c denotes the compression velocity. The value of α must be limited between 0 to 1 to maintain the sharp interface and avoid numerical diffusion in Eq.4-6 and in order to do so, an artificial compression term $\nabla.U_c\, \alpha(1 - \alpha)$ is used in OpenFOAM (Weller, 2002).

4.3.3 Turbulence modelling

In the turbulent flow governed by Navier-Stokes equations, each quantity of flow can be decomposed into the mean and fluctuating part. The RANS equations (Section 4.3.2) are basically obtained through mean flow variables of the governing equations. New term (Reynolds stresses) which represent the nonlinearity (turbulent fluctuations) are introduced in the RANS equations. The turbulent stress may be estimated based on Boussinesq eddy viscosity concept. To predict the effects of turbulence, different turbulence models are used in OpenFOAM. The variable turbulent kinetic viscosity (υ_{turb}) introduced in Eq.4-2 is obtained by choosing the turbulence model. The turbulent dissipation is then simulated using the turbulent viscosity added to the molecular viscosity (Eq.4-4).

In the current work, the k–ω SST (Shear Stress Transport) turbulence model is used to model the turbulence. Menter (1994) blended the k-ε (Launder and Spaulding, 1974) and k-ω (Wilcox, 1998) models to obtain a new model with the best characteristics of each model. To do so, the transformation from the k-ε model into the k-ω is performed. The k-ε model gives accurate results for free shear layers far from surface; however, this model does not performed well within the boundary regions and simulation of the flow separation. This can be compensated using the k-ω in the inner regions. Some significant deficiencies of the k-ω model are its weak performance in the wake of the boundary layer and its inaccurate prediction of asymptotic behavior of the turbulence

near the wall regions. del Jesus et al. (2012) were amongst the first who implemented k–ω SST turbulence model in wave-structure interaction problems. For more information about the basic equations of k–ω SST model, the reader is referred to Menter (1994).

4.3.4 Initial and boundary conditions

The initial and boundary conditions (BC) of the numerical domain are specified to achieve the actual physical interpretation. Generally, two types of boundary conditions are prescribed including Fixed Value Boundary Condition (Dirichlet) and Fixed Gradient Boundary Condition (Von Neumann). The Fixed Gradient Boundary Condition defines the gradient of the field variable normal to the boundary while the Fixed Value Boundary Condition defines the value of an independent field variable at the boundary. No-slip boundary condition for velocity (u) is adopted and zero gradient pressure (p) and phase fraction (α) are assigned for at the flume's walls and bed.

The physical behavior of the near-wall areas is different from the other parts of the flow region. Launder and Spalding (1974) introduced a new term in momentum equations which compensates the increased turbulent viscosity at the transitional and wall regions. The law of the wall is used to treat other turbulence components (k, ω, ...). In this way, the turbulence transport equations are not solved near the wall region. The wall boundary condition in the OpenFOAM can be specified for each patch. Two types of Wall Functions, nutWallFunction and nutRoughWallFunction, are used in the present work for hydraulically smooth and rough bed conditions, respectively, to specify the turbulent viscosity effects. The roughness characteristics can be easily adapted in the OpenFOAM turbulent eddy viscosity directory. The velocity and the phase fraction at the flume's outlet are assigned to zero-gradients and the pressure is set to be a fixed value. The atmospheric boundary condition at the flume's top face is adopted similar to the flume's outlet (Rusche, 2002).

The phase fraction (α) is set to 1 in parts of flume filled with water at the reservoir during the initial time before releasing the impounded water depth (h_u). For the wet bed condition cases at the flume downstream, the same phase fraction $(\alpha = 1)$ is applied up to the downstream water depth (h_d). For the remaining parts of the flume, $\alpha = 0$ is assigned since it is filled with the air. Furthermore, the initial velocity and pressure are set to zero and the turbulence parameters are assigned to small initial values for the sake of convergence of the initial iteration.

4.4 Validation of the model

4.4.1 Physical experiments of Nouri et al. (2010)

The physical experiments were conducted in a 10.6 m length, 2.7 m width and 1.4 m height flume at the Canadian Hydraulic Center of the National Research Council (NRC-CHC) flume, located in Ottawa. The schematic plan view of the flume is shown in Figure 4.3. A variable pitch pump is used in order to adapt the discharge amount (0 to 1.7m^3/s) inside the flume. The flume was fabricated from stainless steel flume and has two glass side windows at the location of the structure providing video capturing of the flow. The still water behind the swinging gate was suddenly released based on the dam-break mechanism and highly turbulent bores were advanced into the downstream. The gate removal duration based on the video recording was estimated about 0.25sec to 0.3sec. The experimental test had been performed for several impounded water depths h_u=0.50m, h_u=0.75m, h_u=0.85m and h_u=1.0m. To avoid water leakage into the downstream, some rubber water-stops were positioned on the upstream side of the swinging gate.

Different structural cross-sections were used in the experiments; however, the circular structure is of interest in the present study. The circular column was fabricated of polyvinyl chloride (PVC) with a 320mm outer diameter, 9mm thickness and 700mm height. Seven wave gauges (WG, capacitance type) with the sampling rate of 1 kHz were positioned inside the flume at the desired location in order to measure the water surface elevation. The vertical distance of the WGs were approximately 10 to 20mm from the flume bottom. In order to measure the stream-wise force exerted on the circular column, a multi-component dynamometer (AMTI MC6 series) was utilized. The column was attached to the upper plate of the dynamometer and the applied forces and moments were converted to voltage and recorded using the data acquisition system. Steel mounts were attached and bolted to both the circular column and the dynamometer. The sampling rate was set to 1 kHz. The pressure exerted on the column was captured using the differential pressure transducers (Honeywell model PK 80083) with a coated water proofing sensor of the capacity of 15.1kPa. Ten 5mm diameter holes were mounted on the upstream side of the circular column with the distance of 50mm.

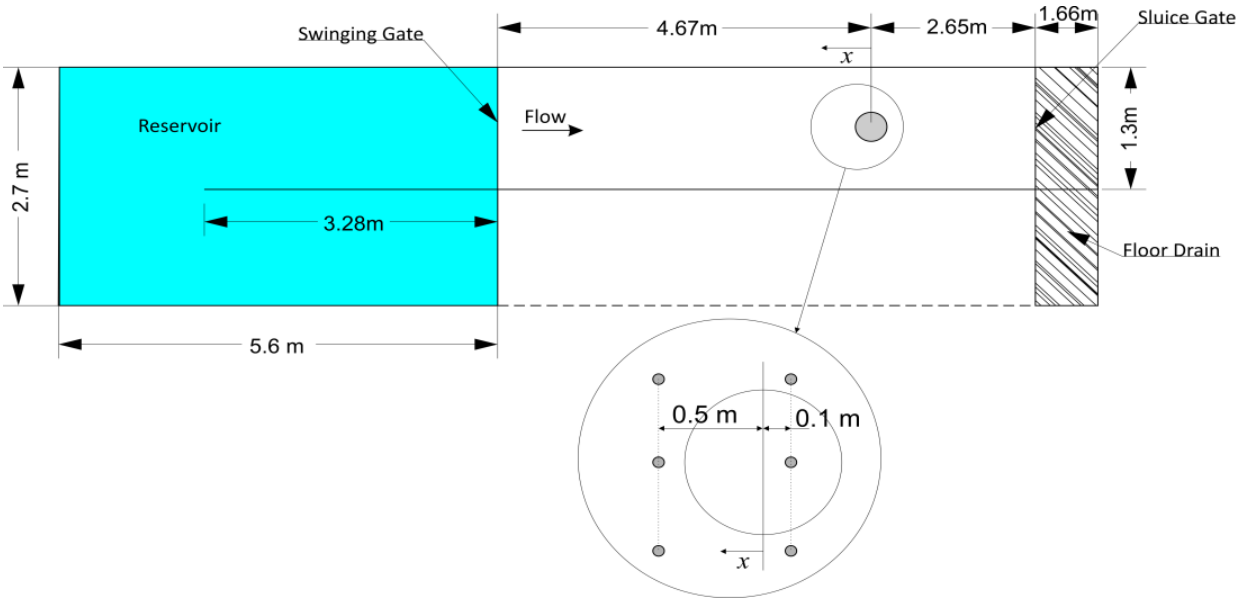

Figure 4.3 Plan view of the physical experiment

4.4.2 Validation of the numerical experiment

4.4.2.1 The Computational Domain

The precise geometry of the Nouri et al.'s (2010) physical experiment was replicated here. The general configuration of the numerical domain is shown in Figure 5.1. The flume drain is simulated numerically to avoid formation of backflow. The impounded water depths of h_u=0.50m and h_u=0.85m are chosen to examine the capability of the numerical simulations. After releasing the impounded water, the bore advances into the flume downstream and impacts the column. The net stream-wise force exerted on column, water surface elevation and pressure time histories are measured at every time step. An unstructured mesh discretization was used for each simulation using ABAQUS to save computational cost. The total number of mesh cell was 1.6 million cells. Computational time needed to simulate 8sec of the physical experiment was approximately 5.5 days using 2 processors (3.60GHz). In order to achieve accurate results, finer mesh sizes were adapted in vicinity of the structural column. The mesh resolution near the circular column was chosen to be 1x1x1.5 cm in x, y and z directions, respectively. This discretization grows gradually moving away from the column. In order to capture turbulence effects around the structure, the mesh resolution is tried to be kept fine at the radius of 1.2 m around the circular column.

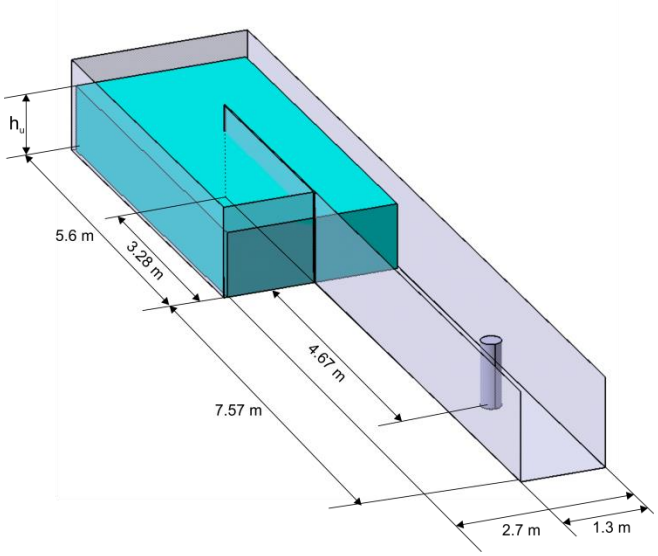

Figure 5.1 Computational Domain

4.4.2.2 Sensitivity Analysis

Results of sensitivity analyses on the turbulence model are presented in Figure 5.2. First, a sensitivity analysis of turbulence model was performed using three different RANS turbulence models: k–ω SST, realizable k-ε and k-ε . The time histories of stream-wise forces exerted on circular column are compared for these aforementioned models. As shown in Figure 5.2, the resulting forces obtained from the k–ω SST turbulence models give the best match to the Nouri et al.'s (2010) experimentally captured forces. A slight discrepancy can be observed between 2.0 sec to 3.0 sec in the time history of the force obtained by k–ω SST turbulence model; however, the overall agreement between the numerical simulation and experimental results of the stream-wise forces is reasonable. On the other hand, for the two other turbulence models, the captured stream-wise forces from the numerical simulation over predict the stream-wise forces.

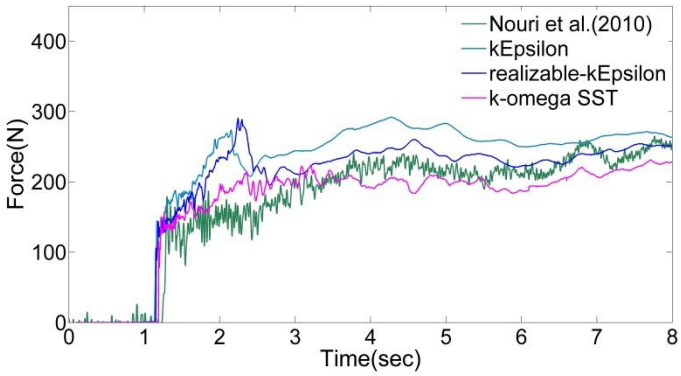

Figure 5.2: Sensitivity analysis of turbulence model

4.4.2.3 Validation results

The comparisons of the numerical time histories of stream-wise forces with the experimentally captured forces are displayed in Figure 5.3. Two different impounded water depths were numerically tested. Both impounded water depths show good level of agreement between obtained time histories of stream-wise forces for numerical and experimental measurements.

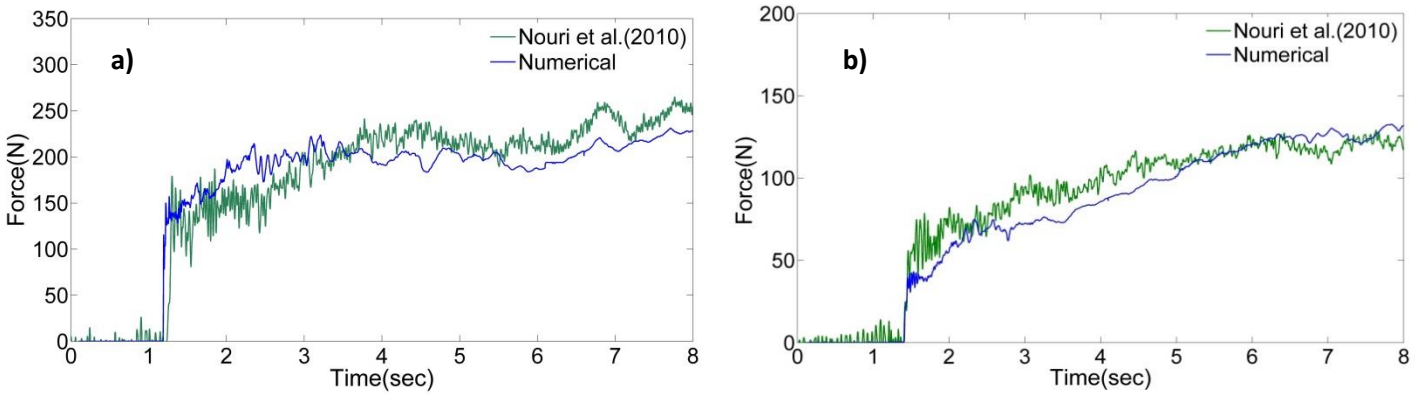

Figure 5.3: Time histories of stream-wise force for impounded water depths a) h_u=0.85m b) h_u=0.50m

In the case of impounded water depth h_u=0.85m the numerical model reproduced the impulsive force with a reasonable level of accuracy; however, the impulsive force for impounded water depth h_u=0.55m was undetermined. In general, the overall trends of stream-wise force for the numerical simulation of the case h_u=0.55m show a reasonable agreement. In the St-Germain et al.'s (2012) numerical study, the single phase smoothed particle hydrodynamics (SPH) numerical model is implemented. The resulting stream-wise force exerted on the circular column shows significantly

higher values compared to the experimental force. Generally, the validation results for the force show that the model is able to accurately compute the stream-wise force acting on the structural column.

Moreover, the time histories of pressure are also presented in Figure 5.4 for different vertical elevations at the upstream side of the column. The numerical simulations of pressure are compared with experimental measurements obtained from pressure transducers (PT) located at 5cm (PT5) and 25cm (PT25) above the channel bottom. During the initial impact, the model fails to predict the measured impulsive shock pressure for PT5; however, later at the quasi-steady state, fair level of agreement can be observed. As the vertical distance above the flume channel increases, the magnitude of the impulsive pressure is reduced. This can be seen in Figure 5.4b for PT25. Although a slight drop in the numerical time history of pressure can be observed after 5.5sec, the overall trend follows the experimental measurements.

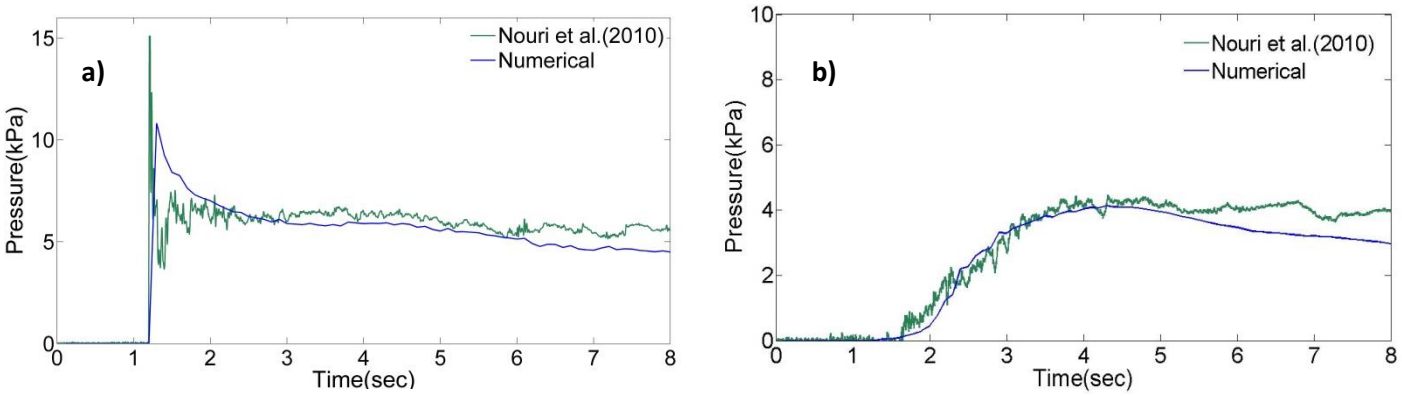

Figure 5.4: Time histories of pressure for PT for impounded water depths h_u=0.85m a) PT5 b) PT25

On the other hand, the quantitative comparison of the temporal variations of water surface elevation for the unobstructed flow condition is presented in Figure 5.5 for WG1, WG2, WG3, WG4, WG5 and WG6. As shown in Figure 4.3, the WG's are located in two rows at the $x = +0.1$ (WG1, WG2, WG3) and $x = -0.5$ (WG4, WG5, WG6) in the absence of structure. Although the numerical model fails to predict the water surface elevation at the moment the bore reached the location of WG ($t = 1.5$sec), for the rest of the simulation, the numerical model fairly replicates the experimentally captured water surface elevation. For numerical WGs, since the results of all WGs are the same, only one of them are displayed here.

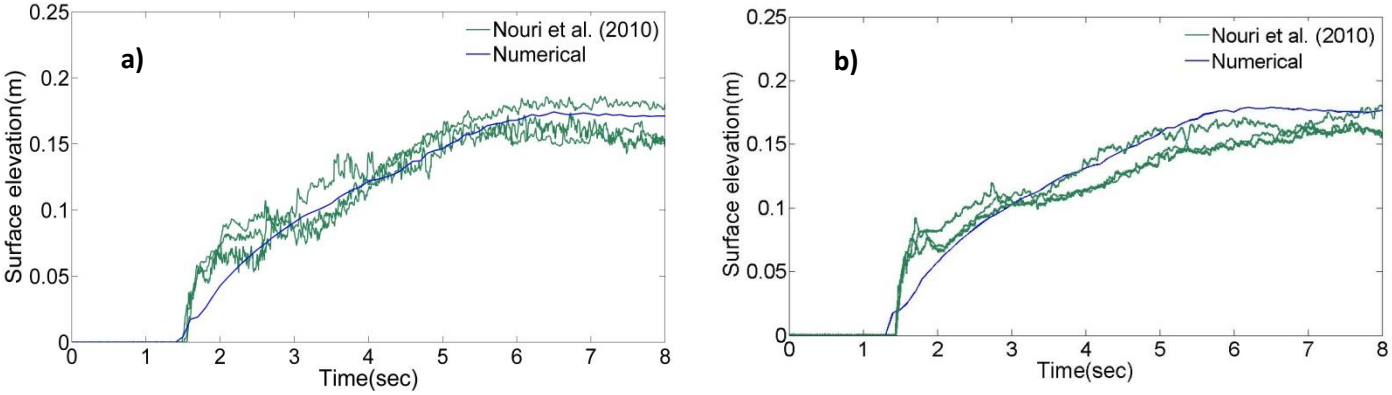

Figure 5.5: Comparison of numerical and experimental temporal variations of water surface elevation for h_u=0.50m a) $x = +0.1$ b) $x = -0.5$

4.5 Results and discussions

4.5.1 Computational domain

Two computational domains were simulated for better understanding of bore-structure interaction on dry bed condition: (i) circular column (ii) elliptical column. The minor axis of the elliptical column is kept the same as the circular column's diameter and the major axis is considered twice of the minor axis in the direction of the flow. Moreover, the influence of bed condition on flow propagation characteristics and the resulting force exerting on the circular column is investigated here. For this reason, numerical simulations are performed for dry and wet bed conditions as well as considering bottom friction. For the case of dry bed, smooth and sand and asphalt beds are examined. In order to assign the bottom friction, the roughness height (k_s) can be easily defined as discussed in section 3.4. For the wet bed conditions three cases are modeled which include h_d=0.050h_u, h_d=0.30h_u and h_d=0.50h_u. All cases are examined for h_u= 550mm and h_u= 850mm. In order to avoid the flow blockage affect the resulting forces exerted on the column, the flume width is increased. The blockage effect of sidewalls forms a subcritical wave which is propagating upstream. Arnason et al. (2009) argued that the formation of bow waves is caused by bore run up on sidewalls at the column's upstream. This resulted in water build up behind the structural column in narrow channel and may affect the resulting force. The blockage ratio is defined as the ratio of the column width to the flume width. Wei et al. (2015) conducted the numerical replication of Arnason et al.'s (2009) experimental work. For example for the case of circular column, the authors performed additional simulations by increasing the flume width 50% (BR=16%) and 100% (BR=12%) wider and compared the resulting

hydrodynamic force with the value obtained in the original setup (BR=23%). Based on their results, the wider the flume was, the lower values of hydrodynamic force were obtained. This was also observed by St-Germain et al. (2014). In the present study, the BR=7% is considered conservatively. In order to achieve this ratio, the computational domain is expanded. The general configurations for both dry and wet bed condition are shown in Figure 5.6. The drain was simulated thereby the water could easily leave the computational domain. For the cases of wet bed, in order to simulate the motionless water at downstream side of the channel's floor, a partition equal to the height of water layer in the downstream (h_d) is modeled preventing the downstream water from leaving the computational domain. The circular structural column is positioned at 4.92m from the reservoir downstream to ensure that the bore will be fully developed. The circular column's diameter and height are taken as 0.32 m and 1.0 m, respectively. The number of grid cells is approximately 2.3 million. The same mesh resolution and quantities are considered in the vicinity of the structure as described in section 4.2.1.

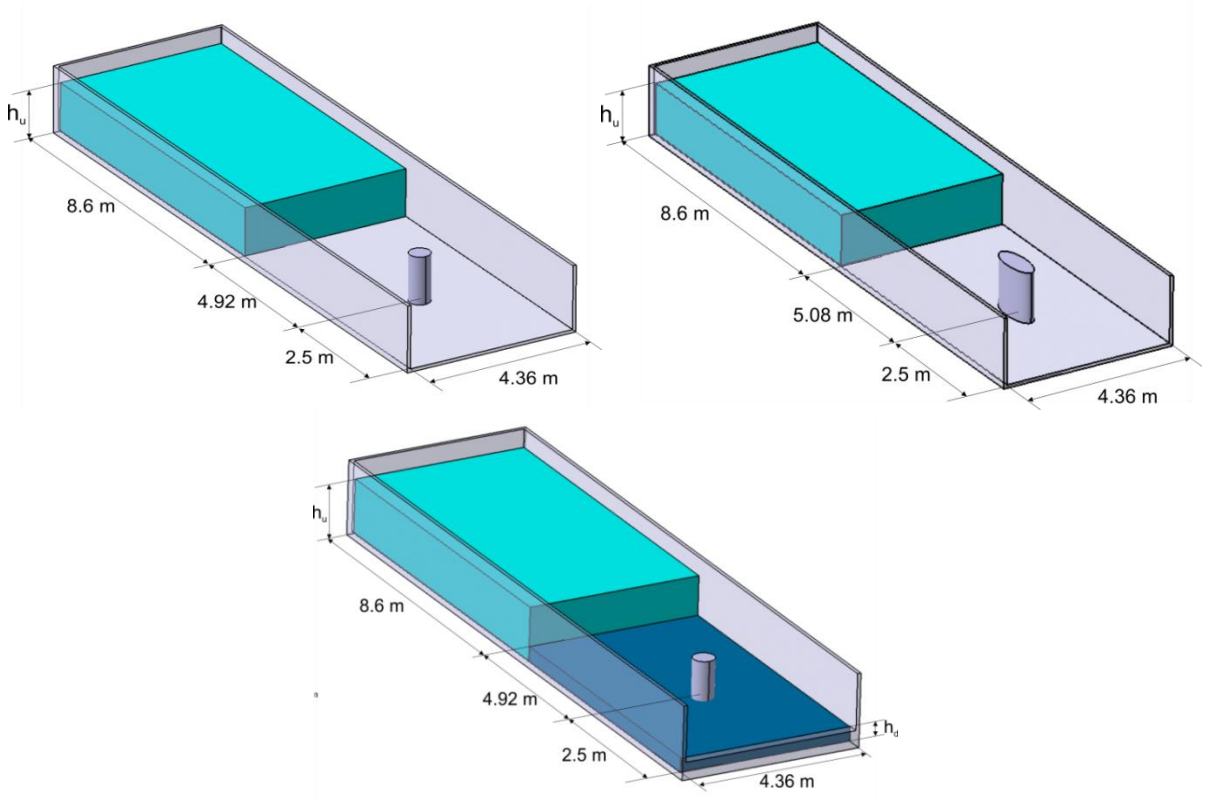

Figure 5.6: Computational domain a)circular column over dry bed b) elliptical column over dry bed c)circular column over wet bed

4.5.2 Comparison of force action on circular vs. elliptical columns

The time histories of stream-wise force for impounded water depth h_u= 550mm are presented in Figure 5.7 for both circular and elliptical structures. As it can be observed, the hydrodynamic forces exerted on elliptical columns are drastically lower with respect to the circular column. Although the projected width subjected to the flow is equal for both columns (diameter of the circle), it appears that the shape of the curvature at the upstream side of the elliptical column smoothly splits the flow and redirected it around the column. The bore run-up on columns upstream is almost negligible at this case. The overall comparison between the run-up elevations indicates that higher elevation for the circular column was captured relative to elliptical column especially at the initial moments after impact (Figure 5.7). Further, after around 6.0 sec, the resulting force converged for both structural columns.

Moreover, the evolution of the bore around the columns and measured exerted force on columns are studied at some key moments. The impulsive force occurred momentarily after the impact at t=1.6sec (red points, A, in Figure 5.7). Comparing the bore run-up on upstream face of both structural columns at this time shows lower elevation for the elliptical column and as a result, less impulsive force occurred. Afterwards, the bore splashed back after the initial run-up (purple points, B) and formed the surface-roller around the column. These moments can be observed after t=2.1sec in Figure 5.8 and after t=2.6sec in Figure 5.9 for the circular and elliptical columns, respectively. Unlike Arnason et al. (2009) experimental study, the maximum force (heap) did not occurred at the moment of run-up collapse which was referred to bow wave in the their study.

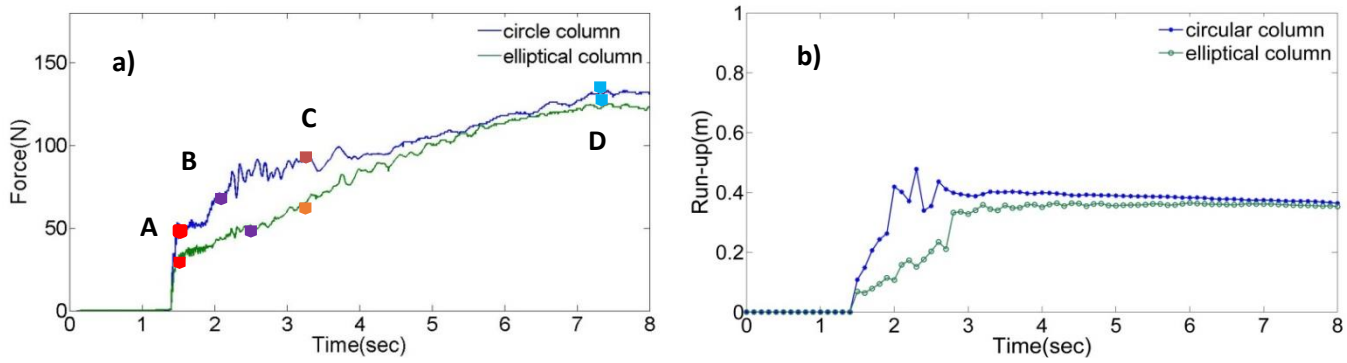

Figure 5.7: Time histories of circular vs. elliptical columns for h_u=550mm a) Stream-wise force acting on the columns b) bore run-up on upstream side of the columns

The quasi-steady state begins approximetly after 3.2sec for both columns. It appears that the combination of high velocity and bore depth leads to maximum hydrodynamic force (orange points, C). The resulting force grew until 7.0sec when finally remained constant. By this time, the wave induced by obstructrion advancing upstream can be clearly observed. The surface-roller is almost disappeared at this time (blue points, D).

The formation of the wake and its structure is also highlighted in order to better analyze the resulting force exerted on the column. The wake is formed after 2.1 sec at the positon about two times the diameter of the column in the downstream direction. For the elliptical column, the bore rejoined after 2.2 sec at the positon about one and half times of the ellipse major axis in the downstream of the leeside of the flume and lead to formation of wake. The formation of rooster tail in the wake of the structure was evident at the centerline of the flume.

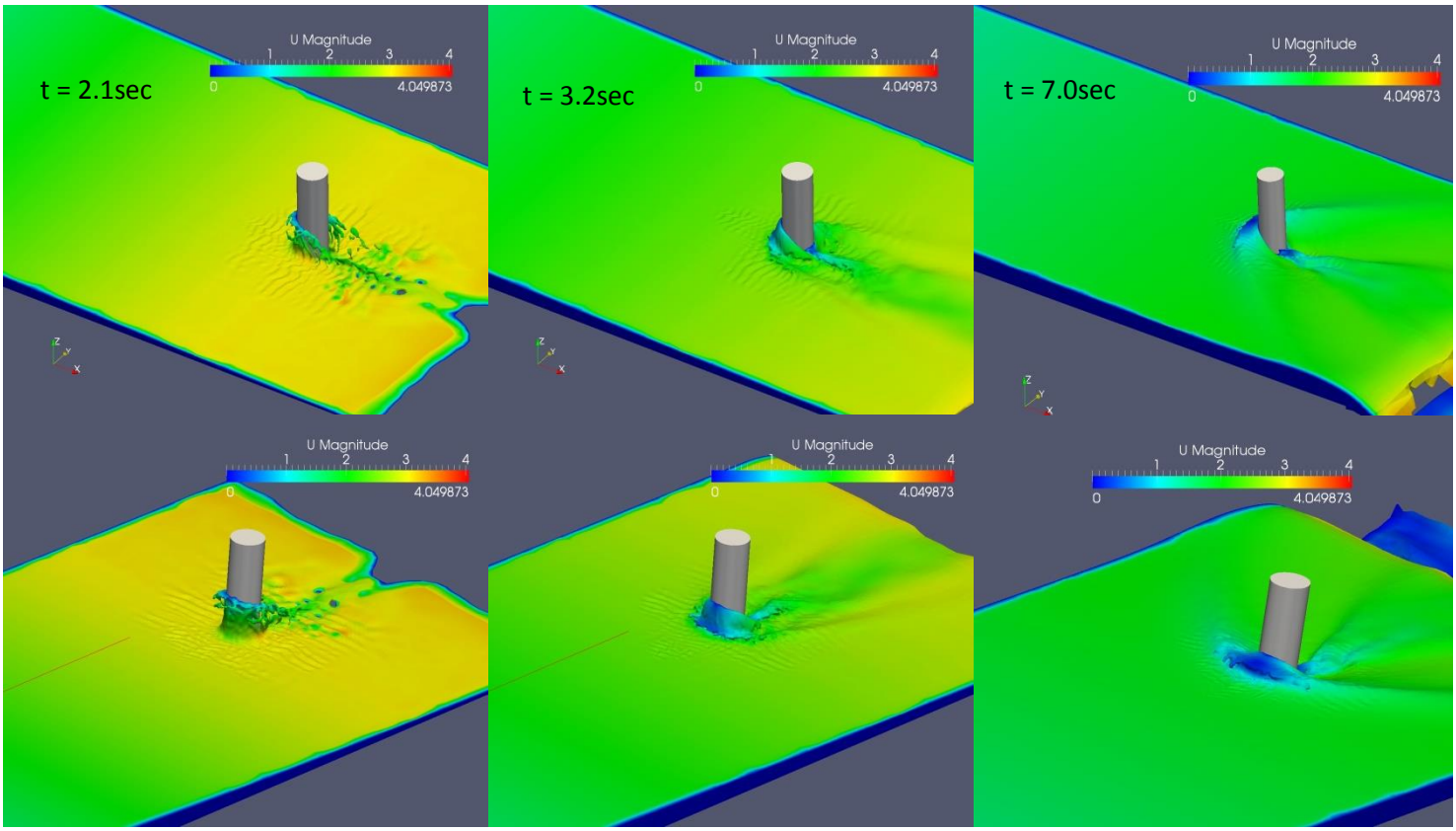

Figure 5.8: Snapshots of bore impinging on the column at some key moments for circular column

As shown in Figure 5.8 and Figure 5.9 after 3.2sec, the bore in the wake of columns is completely developed as the surface-roller redirected around the column and filled the leeside of the flume. This was resulted in establishing a vortex at the leeside of the column. At this time, the wake is highly turbulent and contained high amount of air entrainment.

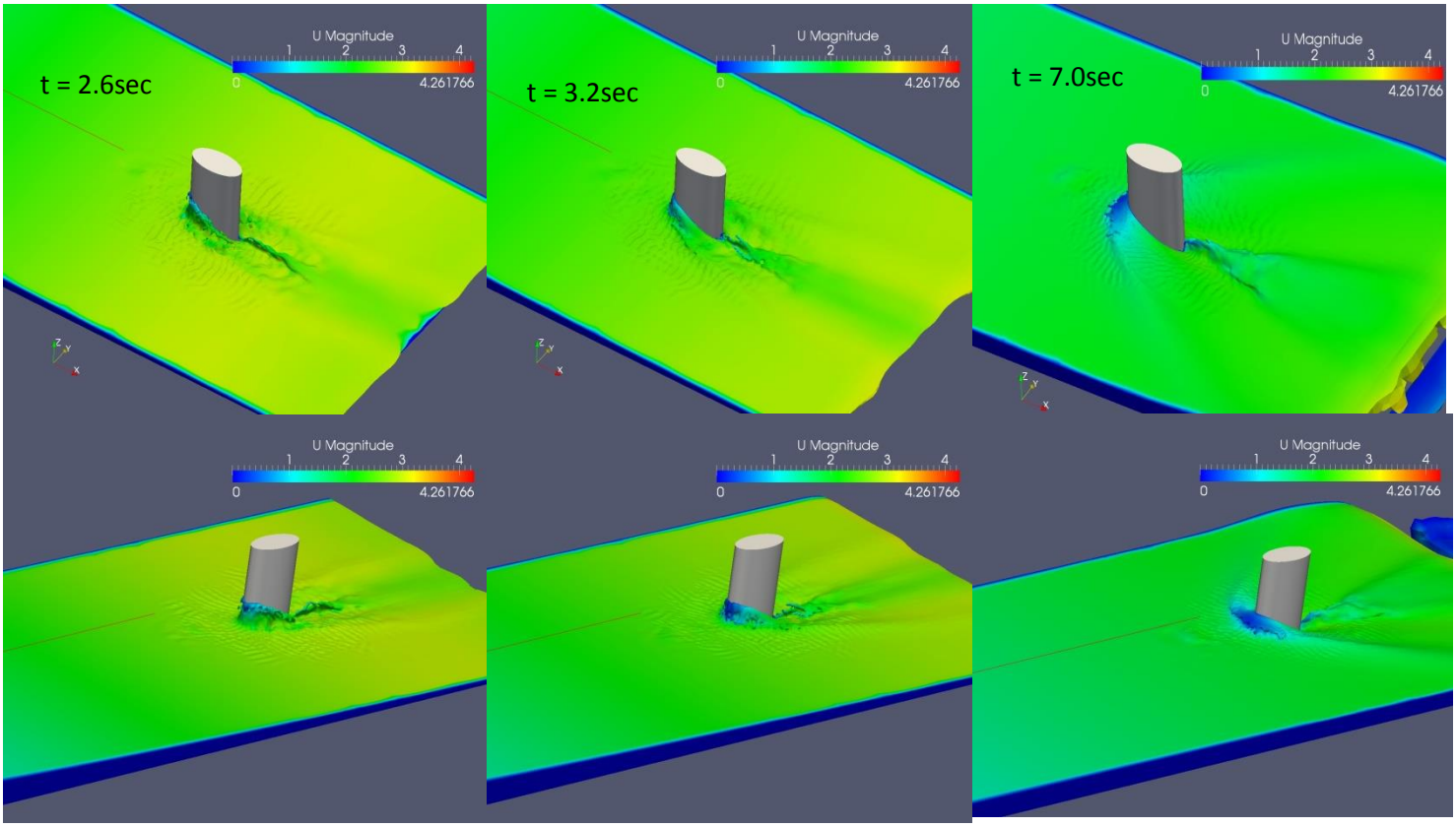

Figure 5.9: Snapshots of bore impinging on the column at some key moments for elliptical column

4.5.3 Effects of the bed condition

Generally, tsunami waves intrude inland areas in the form of highly turbulent hydraulic bore. The first tsunami wave usually inundates the inland areas over a dry bottom referred to "dry bed condition" while the second or third waves of tsunami may advance into the inland area before the first wave flood receding. This scenario is referred to as "wet bed condition". As reported in the literature, the presence of still water layer (h_d) on the flume bottom can drastically influence the propagation development. In this section, the bore propagation characteristics on both wet and dry bed conditions are compared and discussed. Moreover, the resulting forces and pressures are presented for the all tested downstream water depths. In this section, the influence of bed conditions for downstream to upstream water depth (h_d/h_u) are investigated for h_d/h_u as 0.05, 0.3 and 0.5.

4.5.3.1 Bore characteristics

The comparison between dam-break analytical solution and the numerically obtained bore profile is presented here. Chanson (2009) developed a simple analytical solution for dam-break waves in the resistance-dominated wave tip region for both dry horizontal and slope beds using shallow water equations. The bed friction was considered using Darcy-Weisbach friction factor (ƒ). In Figure 5.10, the X axis corresponds to the direction along the flume length and h represents the water surface elevation. As shown in Figure 5.10, a good agreement can be observed between the numerical model and Chanson's (2009) analytical solution for the dry bed condition.

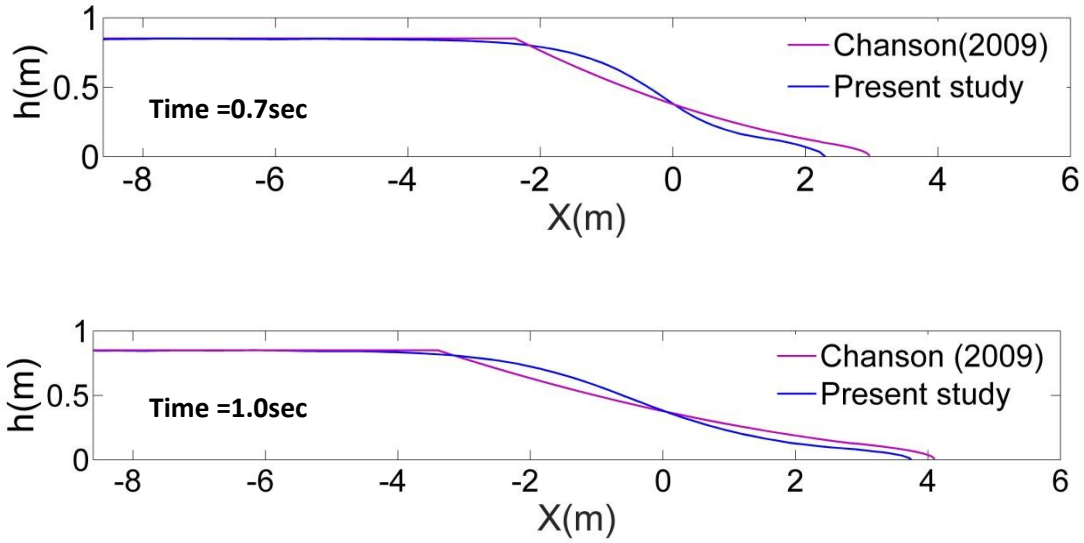

Figure 5.10: Comparison of bore profile for numerical model and Chanson's (2009) analytical solution

Furthermore, the comparison between the depth-averaged velocity for all tested downstream depths as well as dry bed is presented in Figure 5.11a. The velocities are measured at the upstream side of the column further from the stagnation region. The presence of the water layer in the downstream side causes a resistance to the propagation of the incoming bore. Therefore, as expected, the bore front velocity decreases as the downstream depth increases owing to energy dissipation. Moreover, a delay in arrival of the bore front is observed as the downstream depth increases. As the downstream depth increases, a significant drop in bore front velocity is occurred; however, for the cases of dry bed and wet bed condition with h_d/h_u as 0.05 (h_d=2.75cm), the depth-averaged velocity converge

further after 3.0sec at the quasi-steady state. For the case of higher downstream water depths (h_d/h_u as 0.3, (h_d=16.5cm) and h_d/h_u as 0.5 (h_d=27.5cm), a considerable reduction in depth-averaged velocity is occurred. The significant change in velocity is observable even in the quasi-steady state. According to Douglas and Nistor (2014) numerical study, for the downstream to upstream ratio (h_d/h_u) ranging from 0.0043 to 0.043, the same reduction on bore front velocity is observed. However, at the quasi-steady state, the velocities converged eventually. This trend is not observed in this study for higher downstream depths (h_d/h_u more than 0.3). It seems that after a specific downstream depth (here h_d/h_u more than 0.3), the bore propagations characteristics will change remarkably due to higher turbulence and energy dissipation.

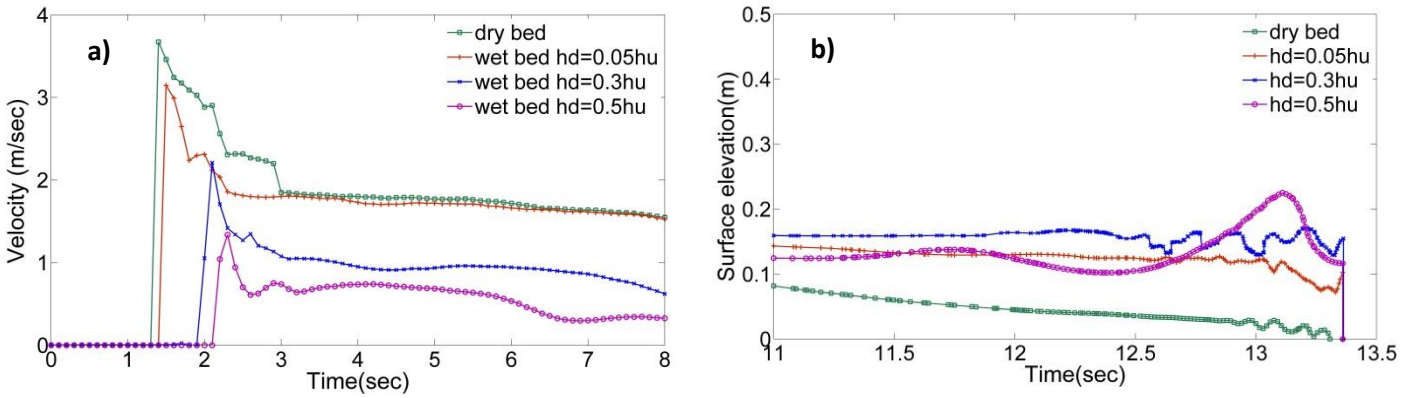

Figure 5.11: Comparison between dry and wet bed conditions a) depth-averaged stream-wise velocity of bore b) bore front profile momentarily before impact

Figure 5.11b shows the comparison between bore profiles for all examined bed conditions momentarily before impact. All the bore profiles are measured and presented relative to the reference elevation of the still downstream water depth since only these moving surface profiles may contribute in initial impact forces. For the case with h_d/h_u = 0.5, a distinctive difference in the bore front profile is appeared. At the very front of the bore, an undulation at the bore surface is formed prior to the impact followed by a less perceptible undulation surface behind it. Interestingly, a lower water surface elevation is measured for the case of h_d/h_u as 0.5 with respect to the case of h_d/h_u as 0.3. This can be attributed to significantly lower total head for the case of h_d/h_u as 0.5 and subsequent lower velocity. This lower head induces less kinetic energy. Moreover, it seems that higher bed resistance will be provided by higher still water at downstream depth. For the other wet bed conditions (h_d/h_u = 0.05 and 0.3), relatively vertical bore front is measured with respect to the dry

bed condition. The general trend shows steeper and deeper bore front as the downstream water depth increases. The overall deeper and steeper slope for the downstream to upstream depth ratio of h_d/h_u = 0.5 may lead to the higher impulsive force at the initial impact which will be discussed in the next section. The same trend of bore front was reported by Janosi et al. (2004) and Crespo et al. (2008). Janosi et al. (2004) observed higher air entrained bore front, unstable jets and breaking of wave for dam-break flow moving over wet bed channel during their experimental study.

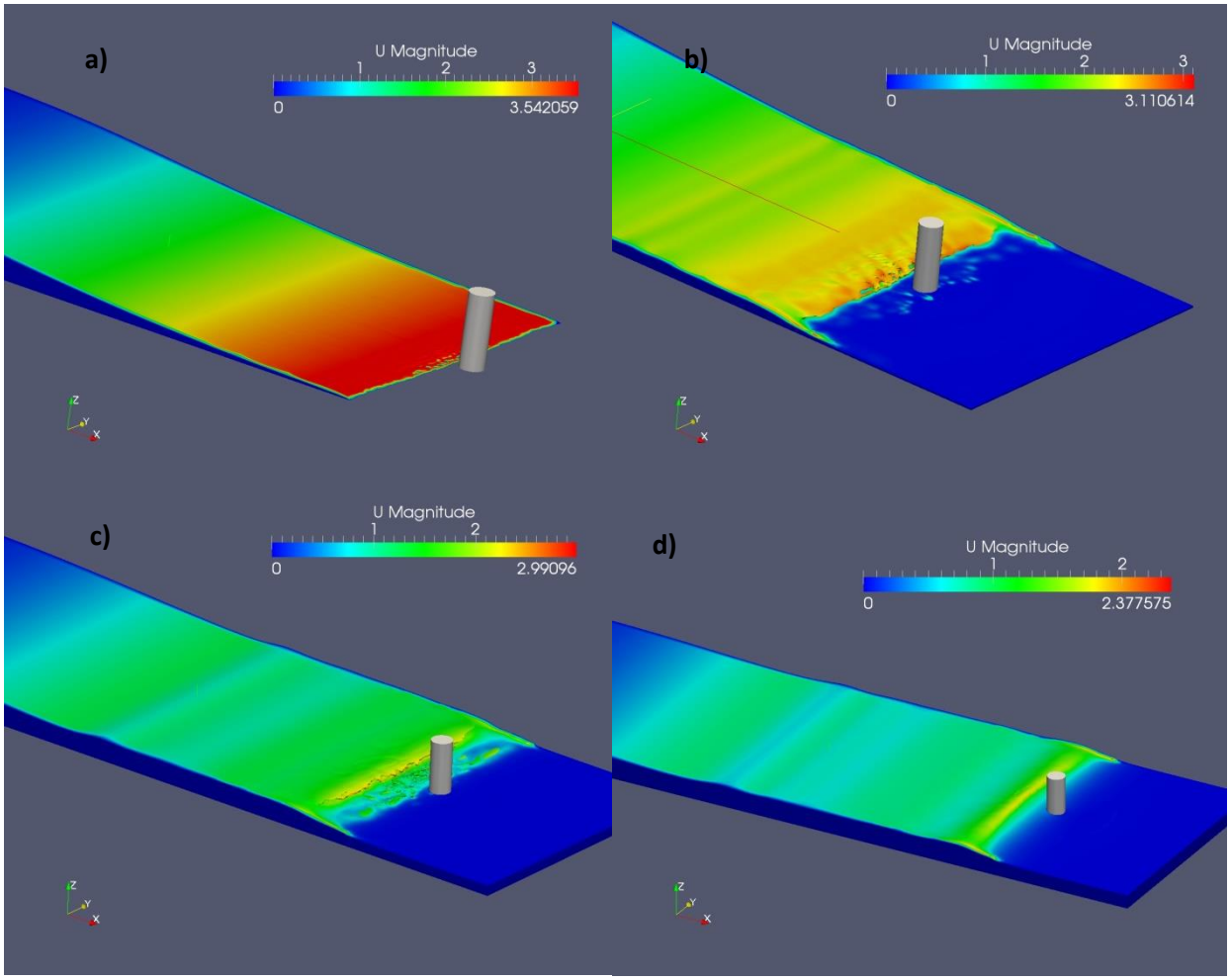

Figure 5.12: Snapshots of bore impinging on the column during the impact time a) dry bed b) wet bed h_d=0.05h_u c)wet bed h_d= 0.3h_u d)wet bed h_d=0.5h_u

The bore development over different bed conditions before impact is displayed in Figure 5.12. The undulation surface at the bore front is clearly observable for the case of depth ratio h_d/h_u equal to 0.5. Furthermore, the steeper bore front approaches the column for the cases of the wet bed conditions relative to the dry bed condition. Comparing the overall features of bore front for wet and dry bed

conditions indicates the difference between the shapes of the bore front alongside of the width of the flume. The wave train is appeared in the case with h_d/h_u equal to 0.3 and 0.5.

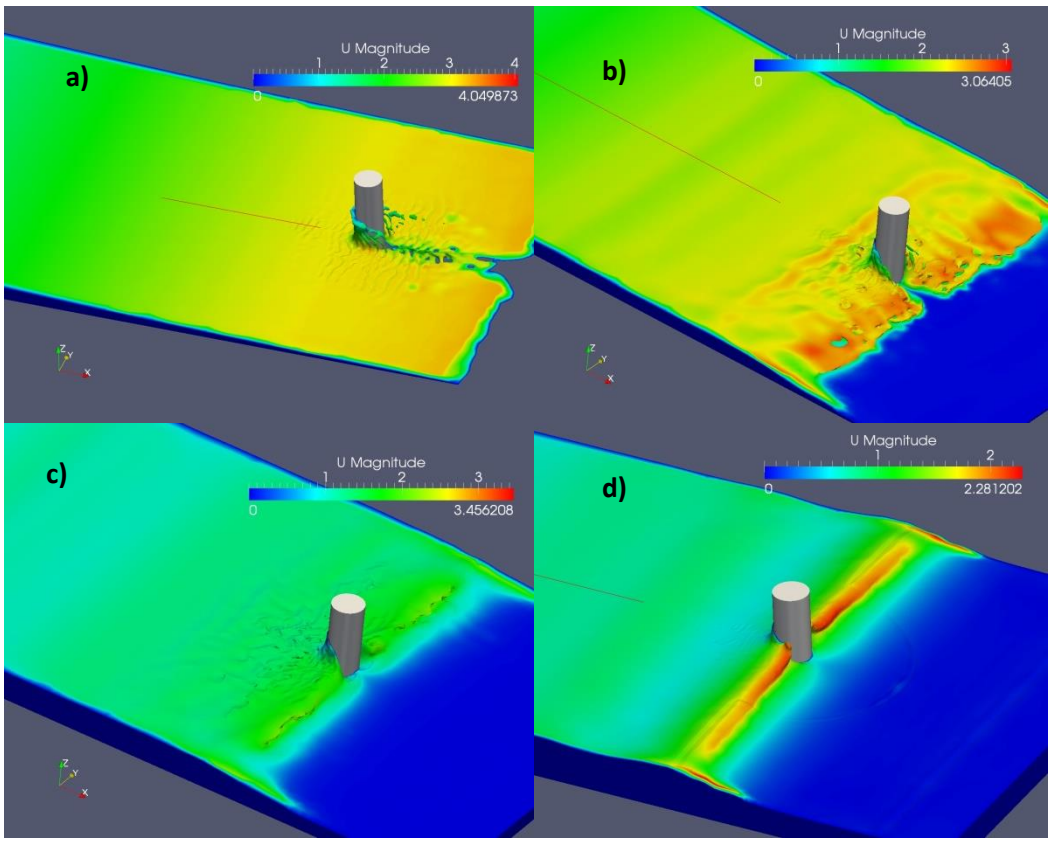

Figure 5.13: Formation of wake at the leeside of the column for different bed conditions a) dry bed b) wet bed h_d=0.05h_u c)wet bed h_d= 0.3h_u d)wet bed h_d=0.5h_u

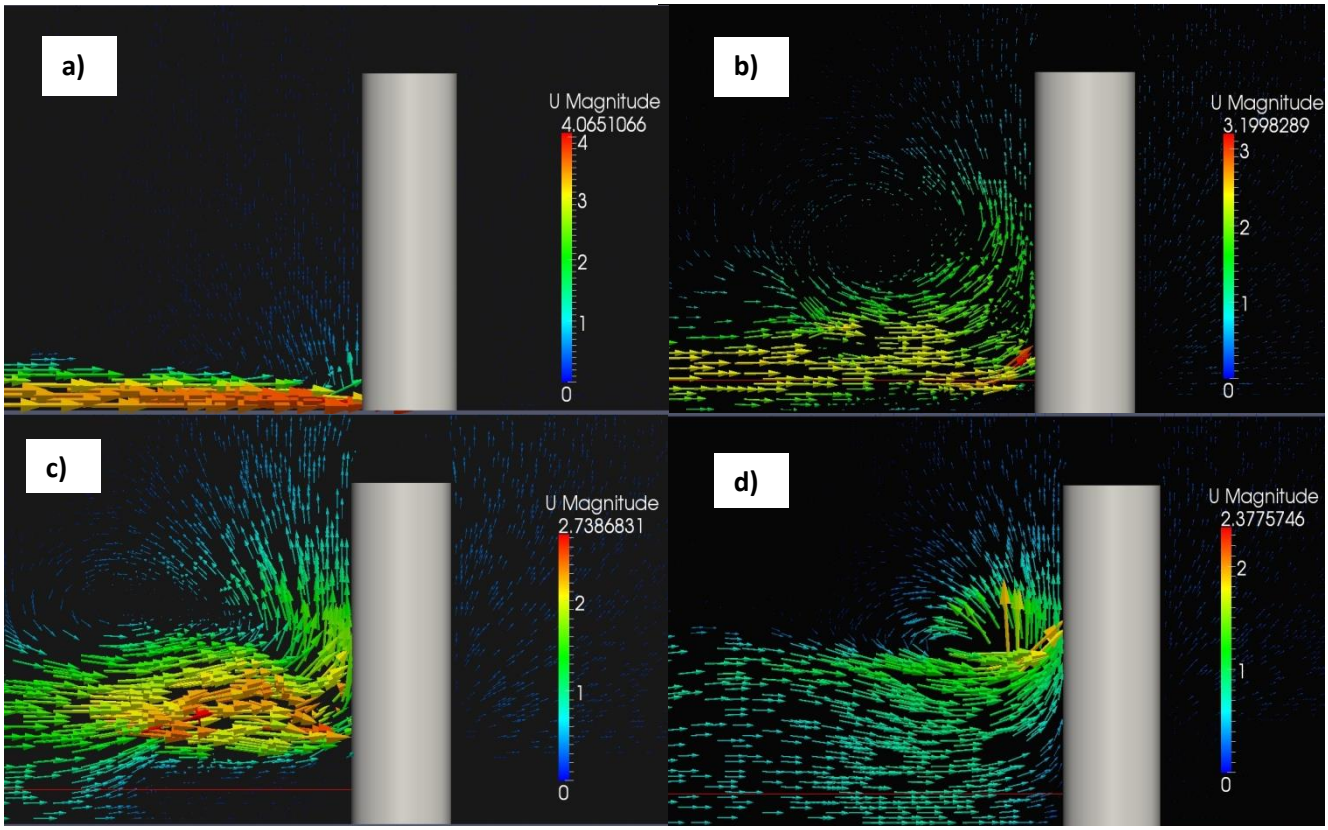

Figure 5.14: Side view of velocity field upstream of column at the flume centerline a) dry bed b) wet bed h_d=0.05h_u c)wet bed h_d= 0.3h_u d)wet bed h_d=0.5h_u

Furthermore, the comparison of the bore-front velocity vectors at the moment of impact is presented in Figure 5.14. A distinct difference between velocity vectors can be observed. Although the bore front velocity is reduced as the depth ratio (h_d/h_u) increased, higher depth and steepness of the bore front (as shown in Figure 5.14) resulted in higher impulsive forces.

4.5.3.2 Resulting forces and pressures

For all tested bed conditions, the time history of stream-wise forces exerting on the column are displayed in Figure 5.15. The comparison between the wet bed cases with higher downstream depth of h_d/h_u as 0.3 and 0.5 with the dry bed condition and (lower downstream depth) wet bed of h_d/h_u=0.05, shows that a clear difference of general trend for resultant stream-wise force is observable. The comparison between the cases of dry bed and (lower downstream depth) wet bed conditions with the

h_d/h_u=0.05 shows that the impulsive force increased for the wet bed condition. Moreover, the subsequent run-up force is also higher for the case of the wet bed condition with the h_d/h_u ratio as 0.05. The similar higher impulsive force for the wet bed condition was also obtained by Ramsden (1993) who compared the dry and bed conditions with the initial impounded water h_u=0.5m and h_d=0.028m.

Furthermore, after around 8 sec, the bed condition has influenced the resulting stream-wise force. The maximum run-up was captured after 2.3 sec in the case of dry bed condition. Despite the wet bed with water depth ratio h_d/h_u=0.5 which shows a run-up higher than 60 cm, for the other tested cases, a run-up height around 45cm is captured. Ramsden (1993) observed higher run-up elevations for the case of the wet bed condition compared with the dry bed. Owing to the circular shape of the column, more amount of flow was redirected around the column rather than splashing up the upstream side. Similar results are also obtained for the bore run-up over the dry and wet bed conditions with the h_d/h_u ratio as 0.05. The run-up elevation for the wet bed condition reaches higher elevation relative to the dry bed condition due to steeper and deeper bore front; however, after 2.5 sec the run-up elevations converges for the aforementioned cases.

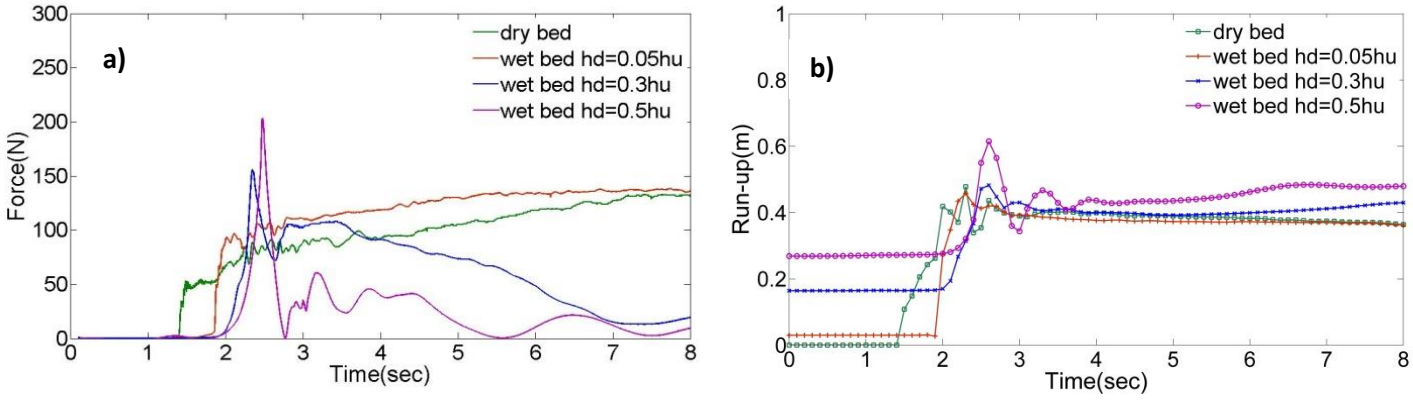

Figure 5.15: Time histories of a) Stream-wise force acting on the column for h_u=550mm b) bore run-up on the upstream side of the column for h_u=550mm

The comparison between the impulsive forces for wet bed conditions with (h_d/h_u) ratios equal to 0.3 and 0.5 show higher impulsive force with depth ratio a (h_d/h_u) equal to 0.5. This can be explained by difference bore front slope and depth for these aforementioned cases at the moment of the impact

(Figure 5.15). For the cases of wet bed with downstream to upstream ratio (h_d/h_u) equal to 0.3 and 0.5, a significant reduction in resulting force can be observed at the quasi-steady state. This could be explained by very slow flow velocity as well as presence of still water depth around the column which leads to same level of hydrostatic pressure at the upstream side and leeside of the column. In the case with $h_d=0.5h_u$, a drop occurred immediately after impact (2.8sec) and the resultant force acting on the column was obtained close to zero. For analyzing the reason of this reduction, the time history of pressure at the upstream side and leeside of the column is measured at 20cm and 30cm above the channel and displayed in Figure 5.16. Interestingly, the same value of pressure was obtained at this moment (2.8sec) at the upstream side and leeside of the column. Afterwards, in the quasi-steady state the pressure difference in upstream side and leeside are negligible. This can explain the reduction in force values which is substantial comparing with the case with a h_d/h_u equal to 0.3. The other reason for the reduction in measured force (also it can be seen in pressure) may be attributable the high amount of air entrainment in the bore front for the case of with depth ratio (h_d/h_u) equal to 0.5.

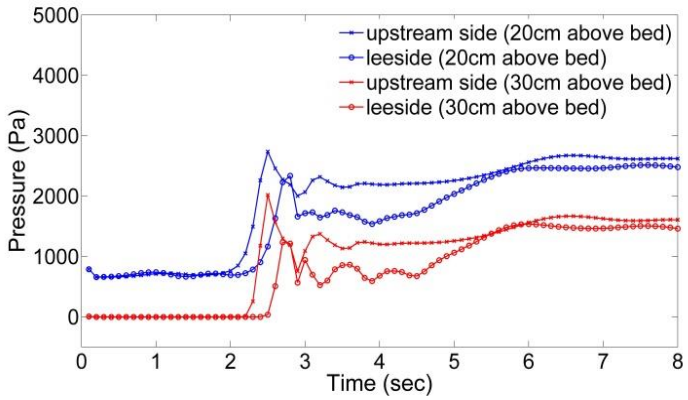

Figure 5.16: Time history of pressure exerted on column: upstream side (cross) and leeside (circle) of the column 20cm(blue) and 30cm(red) above channel bed

Moreover, Figure 5.17 compares the time history of pressure at the upstream side of column. In the case of h_d/h_u = 0.5, the value of impulsive pressure exceeded all other cases. This pressure may contribute in high level of impulsive force for higher depth ratios; a higher portion of the pressure contributed on higher levels for the wet bed condition. At the elevation 30 cm above the bed, still high values of pressure (more than 2000 Pa) were measured in the case of h_d/h_u = 0.5. A significant

pressure drop at 2.8 sec, at the same moment corresponding to the time history of force, can be observed in pressure time history due to high amount of air entrainment.

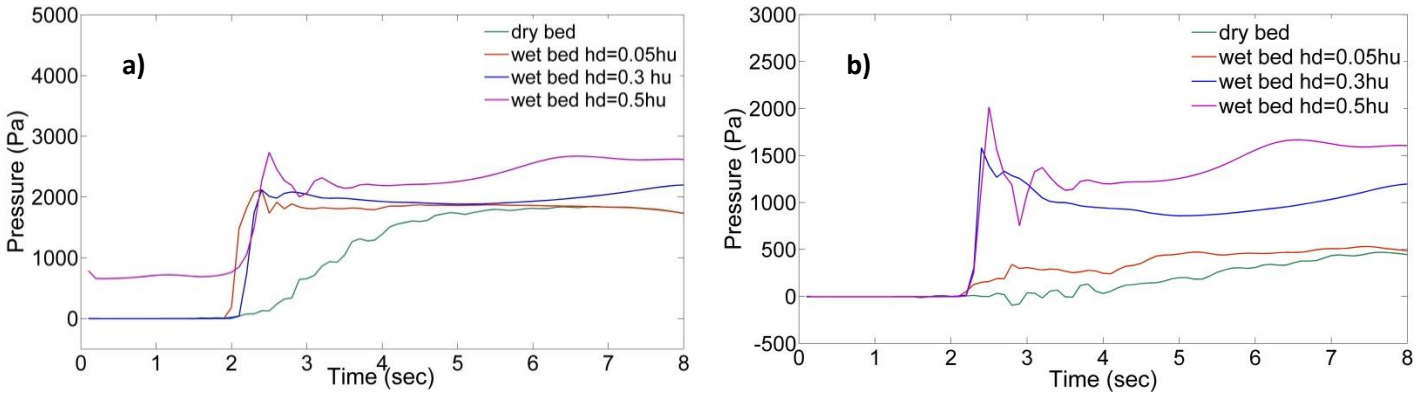

Figure 5.17: The time history of pressure exerted on column upstream side above the channel's bed a) 20cm b) 30cm

4.5.4 Effects of bottom friction

The time histories of stream-wise force exerting on the column is presented in this section. The simulations are performed for both smooth and rough bed and the resulting force and bore depth-averaged velocity are shown in Figure 5.18. In the case of rough bed condition, the impulsive force is reduced substantially. After approximately 6.0 sec, the force converged for smooth and rough beds. The depth-averaged velocity is also displayed in Figure 5.18b. The bore front velocity and the subsequent bore velocity are reduced due to energy dissipation induced by the bottom friction in the case of the rough bed. There is a marginal difference in resulting force in the case of asphalt and sand beds. Owing to lower velocities near the bed, a lower depth-averaged velocity was obtained at the quasi-steady state in the rough bed case.

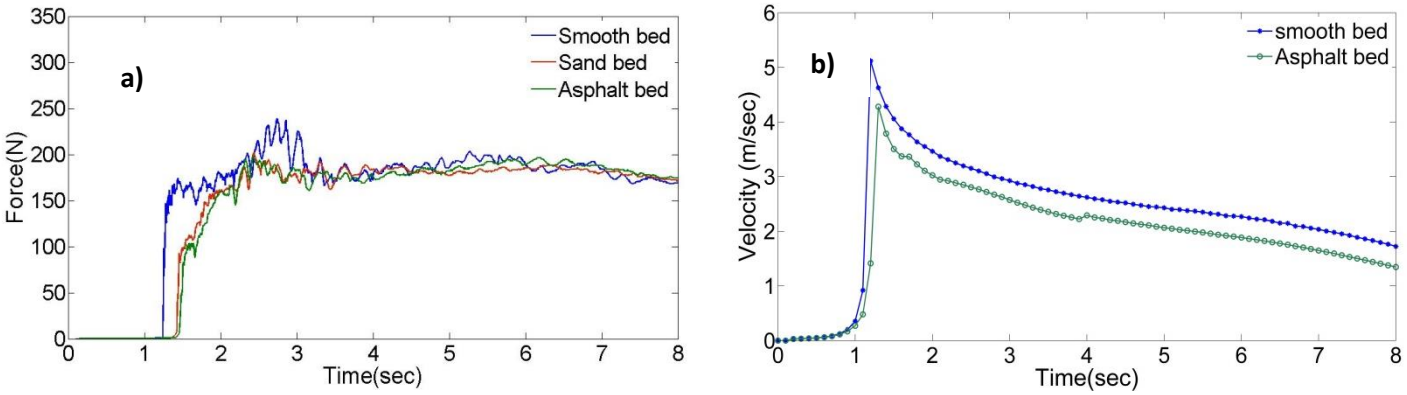

Figure 5.18: Smooth vs. rough bed conditions for h_u=850mm, time histories of a) Stream-wise force acting on the column b) Depth-averaged velocity

4.6 Conclusion

A two-phase three-dimensional numerical model based on RANS equations (interFoam) was used to investigate tsunami-like bore-structure interaction over different bed conditions (wet, dry and rough). The validation of the numerical model was performed by Nouri et al. (2010) experimental data. The resulting force and pressure exerted on the column as well as the bore surface elevation were compared between numerical simulation and experimental measurements for the purpose of validation.

The major objective of the present study is to investigate the bore characteristics and forces exerted on structures over dry, wet and rough bed conditions. For this reason, a scaled-up model is used based on validated numerical model for further simulation in order to eliminate the effects of sidewalls on resulting forces. The numerical simulations for dry bed were performed for circular and elliptical structures. The bore evolution and the resulting force exerted on these columns are compared and analyzed. Moreover, the resulting force exerted on circular column over dry and wet beds with downstream to upstream water depth ratios of 0.05,0.3 and 0.5 are compared and bore propagation characteristics are investigated.

Based on the results, the bore front becomes steeper as the downstream depth is increased. This trend was also obtained for the impulsive force which could be attributed to corresponding steeper bore front as the downstream depth increased. Further, during the quasi-steady state, a significant drop was obtained for the hydrodynamic force in the case of higher downstream to upstream depth

ratio (h_d/h_u as 0.3 and 0.5). The reason for this can be described by the high level of hydrostatic pressure at the leeside of the column. Moreover, the depth-averaged velocity was measured for all bed conditions and significant reduction was observed as the depth ratio increased owing to additional resistance induced by downstream water depth. The establishment of the horseshoe vortex in the wake of the structures differs with the varying downstream bed condition. The higher the depth ratio was, the faster and closer the wake rejoined behind the column. The comparison of the circular column and the elliptical column over dry bed demonstrated that the obtained impulsive force was substantially lower for elliptical column. This could be described by the shape of the curvature at the very front side of the elliptical column that redirected the flow around the column rather than creating splash. The subsequent hydrodynamic force was later converged for both columns.

In the present study the significance of the downstream depth on bore development and its propagation characteristics is revealed. The major factor in this difference can be attributed to bore front steepness. The results support similar studies available in the literature.

5 Conclusion and Future Works

5.1 Conclusion

In the present work, the interactions between rectangular-section structures and walls (different aspect ratios and orientations) with tsunami-like bores were investigated to determine the associating drag coefficients. The dam-break method was used in order to generate tsunami-like bore using 3D numerical models in OpenFOAM. First, the numerical model (using RANS equations with realizable k-ε turbulence model) was validated by experimental results of physical experiments conducted in NRC-CHC in Ottawa. A scaled-up domain was selected using a proper blockage ratio, in order to eliminate the sidewall effects of the numerical simulations on the results.

A slight increase in hydrodynamic force was observed by elongating rectangular-section columns in the flow direction (increasing the AR). In this case, the contributions of friction drag and the pressure difference at the upstream side and the leeside of the column found to be negligible. In the case of rectangular-section walls, the hydrodynamic force is increased by 40% from AR2:1 to AR4:1. In this case, the transient force was substantially higher than subsequent hydrodynamic force. In the case of the rotated square column, higher hydrodynamic force was obtained for structure orientation $\alpha=45°$; however, the initial impulsive force was lower for the aforementioned orientation comparing with the structure orientation $\alpha=0°$.

FEMA P646 (2012) only suggests $C_d=2.0$ for the drag coefficient of structures subjected to tsunami. This code does not provide any information for elongated or rotated or any other geometries of square columns. The present work provided thorough investigations on drag coefficients for elongated and rotated structures with rectangular. The obtained mean drag coefficient range for rectangular-section column with (*AR*= 1,2,4,6 and 8) varies between 1.68 to 1.91. Lower value of drag coefficients are obtained for higher bore depth. This trend is consistent with experimental results performed by Arnason (2005). The resulting mean drag coefficients also increase slightly when the aspect ratio increases. For rectangular section walls (*AR*=2 and 4), the obtained drag coefficients are 1.7 to 2.05. In addition to the wall geometry contribution (aspect ratio of the wall) in

drag coefficients, the simulations showed that higher bore depths resulted in higher drag coefficients for walls. Among rotated square columns, the 45◦ rotated column showed the lowest drag coefficient. The values of drag coefficient were highly sensitive to bore depth rather than aspect ratio. Although, the obtained drag coefficients in the present study was not exceeded the suggested value by FEMA P646 (2012); however, it seems that for lower bore depths the recommended value would be insufficient.

A two-phase three-dimensional numerical model based on RANS equations (interFoam) was used to investigate tsunami-like bore-structure interaction for wet, dry and rough bed. The numerical model was tested by Nouri et al.'s (2010) experimental model. The resulting force and pressure exerted on the column as well as the bore surface elevation were used for the validation. A scaled-up model is used based on validated numerical model for further simulation in order to eliminate the effects of sidewalls on resulting forces.

Another aspect of the present study is to investigate the bore characteristics and forces exerted on structures over different bed conditions. The numerical simulations for dry bed were performed for circular and elliptical structures. Based on the results, a steeper bore front was created as the downstream depth increased. This behavior was also observed for the impulsive force which could be attributed to the corresponding steeper bore front as the downstream depth increased.

Further, during the quasi-steady state, a significant force drop was obtained for hydrodynamic force in higher downstream to upstream depth ratios (h_d/h_u=0.3m and h_d/h_u=0.5m). Moreover, a significant reduction was observed for the depth averaged velocity as the depth ratio increased owing to additional resistance induced by downstream water depth and high amount of air entrainment due to turbulent bore front. The establishment of the horseshoe vortex in the wake of the structures differs with the varying downstream bed condition. The higher the depth ratio was, the faster and closer the wake rejoined behind the column. The impulsive force for elliptical column is substantially lower than the force of circular column. The subsequent hydrodynamic forces were later converged for both columns.

5.2 Future works

1. The present research opens new horizons for bore-structure interaction investigation and also revising the current design guidelines. The proposed future trends are described as follows:
2. More complicated geometries, rather than rectangular-section columns presented in this study, can be investigated to obtain more reliable data for drag coefficients. Moreover a wider range of contributing factors on drag coefficient of structures such as column width, aspect ratio and bore depth can be studied.
3. A series of studies are needed to investigate the effect of pattern characteristics (shapes, sizes and orientations of the multiple structures standing near each other known as effects of macro-roughness) on the hydrodynamic force of each structure.
4. The current work studies the effect of single structure in the tsunami bore. However, in reality, a pattern of multiple structures is exposed to the bore. The effect of the macro-roughness (surrounding structures) on hydrodynamic force exerted on structures exposed to the tsunami bores over different bed conditions can be investigated.
5. Opening in the offshore structures can have a significant effect on the hydrodynamic force and consequent damage on the structures. Quantitative study is recommended on how these opening (their proper locations on the structure) can help to reduce the damage to the structure.
6. In this study, the influence of downstream water depth “known as wet bed condition” was analyzed for circular columns. However; more investigations on the influence of varying bed conditions (considering wider range of downstream to upstream depth ratio) on hydrodynamic forces exerted on different geometries such as square, walls and rectangular are needed.

References

[1] Al-Faesly, T., Palermo, D., Nistor, I., and Cornett, A. (2012). Experimental modeling of extreme hydrodynamic forces on structural models, *Int. J. Protective Structures*, 3(4), 477–505.

[2] Al-Faesly, T. (2016). Extreme Hydrodynamic Loading on Near-Shore Structures *Doctoral dissertation, University of Ottawa,* Canada.

[3] Árnason H. (2005). Interactions between an incident bore and a free-standing coastal structure. *Doctoral dissertation, University of Washington*, Seattle.

[4] Árnason, H., Petroff, C., and Yeh, H. (2009). Tsunami bore impingement onto a vertical column. *J. Disaster Research*, 4(6), 391–403.

[5] Asakura, R., Iwase, K., Ikeya, T., Kaneto, T., Fujii, N., and Omori, M. (2000) An experiment study on wave force acting on on-shore structures due to overflowing tsunamis. *Proc. Coastal Engineering, JSCE*, 47, 911-915 (in Japanese).

[6] Berberovic, E., van Hinsberg, N.P., Jakirlic, S., Roisman, I.V., Tropea, C. (2009). Drop impact onto a liquid layer of finite thickness: dynamics of the cavity evolution. *Physical Review* E 79.

[7] Briggs, M. J., Synolakis, C. E., Harkins, G. S. and Green, D. R. (1995). Laboratory experiments of tsunami runup on a circular island, *Pure Applied Geophysics*, 144, 569-593.

[8] Bruno. L., Fransos. D., Coste. N., Bosco. A. (2010). 3D flow around a rectangular cylinder: A computational study. *J. Wind Eng. Ind. Aerodyn.* 98 (10) 263–276

[9] Bullock, G., Obhrai, C., Peregrine, D., Bredmose, H., 2007. Violent breaking wave impacts. Part 1: results from large-scale regular wave tests on vertical and sloping walls, *Coast. Eng.* 54 (8), 602-617

[10] Chan, I. and Liu, P.L. (2012). On the runup of long waves on a plane beach, *Journal of Geophysical Research*, 117, 1-17.

[11] Chanson, H. (2006). Tsunami surges on dry coastal plains: application of dam break wave equations. *Coast. Eng. J*. 48 (04), 355–370.

[12] Chanson, H., (2009). Application of the method of characteristics to the dam break wave problem, J. *Hydraul. Res*. 47 (1), 41–49.

[13] Chock G., S.E.1; Robertson I., S.E.2; Kriebel D., P.E.3; Francis M., P.E.4;and Nistor I., P.E.5. (2013). Tohoku, Japan, Earthquake and Tsunami of 2011: Performance of Structures under Tsunami Loads. *ASCE*.

[14] Chock, G., Robertson, I., Kriebel, D., Nistor, I., Francis, M., Cox, D. and Yim, S. (2011) Learning from Earthquakes The Tohoku, Japan, Tsunami of March 11, 2011: Effects on Structures. *EERI Special Earthquake Report.*

[15] Crespo, A. J. C., Gómez-Gesteira, M., and Dalrymple, R. A. (2008) Modeling dam break behavior over a wet bed by a SPH technique. *J. Waterway, Port, Coastal, Ocean Eng*., 134(6), 313–320.

[16] Cross, R.H. (1967). Tsunami Surge Forces, *J. Waterways Harbor Div*. 93, 201–231.

[17] Dargahi. B. (1989), The turbulent flow field around a circular cylinder. *Experiments in Fluids*, 8 , pp1-12.

[18]del Jesus, M., Lara, J.L., Losada, I.J. (2012). Three-dimensional interaction of waves and porous coastal structures. Part I: Numerical model formulation. *Coastal Engineering* 64, pp. 57-72.

[19] Douglas, S., Nistor, I. (2015). On the effect of bed condition on the development of tsunami-induced loading on structures using OpenFOAM. *Natural Hazards*, 76(2), 1335-1356.

[20] Earthquake Engineering Research Institute (EERI) [2011]. The Tohoku, Japan, tsunami of March 11, 2011: effects on structures, *Special Earthquake Report*.

[21] FEMA P646. (2012). Guidelines for design of structures for vertical evacuation from tsunamis, *Federal Emergency Management Agency*, Washington, D.C.

[22]Fox, R.W., McDonald, A.T., Pritchard, P.J. (2004). Introduction to Fluid Mechanics, Eighth Edition. JohnWiley & Sons, Inc.

[23] Fujima, K, Achmad, F., Shigihara, Y., and Mizutani, N. (2009) Estimation of Tsunami Force Acting on Rectangular Structures, *Journal of Disaster Research*, Vol. 4, No. 6, pp. 404–409.

[24] Gómez-Gesteira M. and Dalrymple R.A. (2004). Using a three-dimensional smoothed particle hydrodynamic method for wave impact on a tall structure. *Journal of Waterway, Port, Coastal and Ocean Engineering*, 130(2),63–69.

[25] Gupta, V. P. and Goyal, S. C. (1975). Hydrodynamic forces on bridge piers, *Journal of the Institution of Engineers (India)*, Civil Engineering Division 56:12–16.

[26] Hirt, C. W. and Nichols, B. D. (1981). Volume of fluid (VOF) method for the dynamics of free boundaries. *Journal of Computational Physics*, 39:201–225.

[27] Higuera, P., Lara, J.L., Losada, I.J. (2013). Realistic wave generation and active wave absorption for Navier–Stokes models: application to OpenFOAM. *Coast. Eng.*71, 102–118.

[28] Janosi, I. M., Jan, D., Szabo, K. G., and Tel, T.(2004). "Turbulent drag reduction in dam-break flows."Exp. Fluids, 37, 219–229.

[29] Kawamura, T., Mayer, S., Garapon, A., and Sorensen, L. (2002). Large Eddy Simulation of a Flow Past a Free Surface Piercing Circular Cylinder. *ASME J. Fluids Eng*., 124 , pp. 91–101.

[30] Kihara, N.,et al., 2015. Large-scale experiments on tsunami-induced pressure on a vertical tide wall, *Coast. Eng*. 99, 46-63.

[31] Lauber, G. and Hager, W. H. (1998). Experiments to dam-break wave: horizontal channel. *Journal of Hydraulic Research*, 36(3), 291-307.

[32] Launder, B.E. and Spalding, D.B. (1974). The numerical computation of turbulent flows. *Computer Methods in Applied Mechanics and Engineering*, 3(2), 269–289.

[33] Leal, J. G. A. B., Ferreira, R. M. L., and Cardoso, A. H. (2006). Dam-break wave-front celerity. *J. Hydraul. Eng.*, 132(1), 69–76.

[34] Linton, D., Gupta, R., Cox, D., Lindt, J., Oshnack, M. and Clauson, M. (2013). Evaluation of tsunami loads on wood-frame walls at full scale, *J. Structural Engineering*, 139 (8), 1318-1325.

[35] Liu, P. L.-F., Y.-S. Cho, M. J. Briggs, U. Kanoglu, and C. E. Synolakis (1995), Runup of solitary waves on a circular island, *J. Fluid Mech.*, 302, 259 – 285.

[36] Lukkunaprasit, P., Thanasisathit, N., Yeh, H. (2009). Experimental verification of FEMA P646 tsunami loading, *J. Disaster Res.* 4 (6), 410–418.

[37] Madsen P, Fuhrman D, Schaffer H. (2008). On the solitary wave paradigm for tsunamis, *J Geophys Res*. 113(12):1–22.

[38]Madsen, P. A. and H. A. Schäffer (2010), Analytical solutions for tsunami runup on a plane beach: Single waves, N-waves and transient waves, *J. Fluid Mech*., 645,27–57.

[39] Menter, F. R. (1994). Two-equation eddy-viscosity turbulence models for engineering applications. *AIAA Journal* 32(8), 1598-1605.

[40] Mikami, T., Shibayama. T., Esteban. M., and Matsumaru, R. (2012). Field survey of the 2011 Tohoku Earthquake and Tsunami in Miyagi and Fukushima Prefectures, *Coastal Engineering Journal*, 54(1), Special Issue of 2011 Tohoku Tsunami.

[41] Mori, N., Takahashi, T. The 2011 Tohoku Earthquake Tsunami Joint Survey Group, 2012.Nationwide post event survey and analysis of the 2011 Tohoku earthquake tsunami. *Coast. Eng. J*. 54 (01), 1–27.

[42] Nistor I, Palermo D, Nouri Y, Murty T, Saatcioglu M (2009). Tsunami forces on structures. In: Kim YC (ed) Handbook of coastal and ocean engineering, *World Scientific, Singapore*. 261–286.

[43] Nouri, Y., Nistor, I., Palermo, D., 2010. Experimental investigation of tsunami impact on free standing structures. *Coast Eng.J.* 52 (1), 43-70.

[44] Palermo, D., Nistor, I., Al-Faesly, T., Cornett, A., (2013). Impact of tsunami forces on structures. *Int. J. Tsunami Soc.* 32 (2), 58–76

[45] Ramsden, J. D. (1993). Tsunamis: Forces on a vertical wall caused by long waves, bores, and surges on a dry bed, *Ph.D. thesis, California Institute of Technology*, Pasadena, CA.

[46] Ramsden , J.D. (1996). Forces on a vertical wall due to long waves, bores, and dry bed surges. *J.Waterways,Port Coasts and Ocean Eng.*,122(3),134-141.

[47] Reynolds, W.C., 1987, "Fundamentals of turbulence for turbulence modeling and simulation," Lecture Notes for Von Karman Institute, Agard Report No. 755.

[48] Ritter, A. (1892). Die fortpflanzung de wasserwellen. *Z. Ver. Dtsch. Ing*. 36 (33), 947–954.

[49] Robertson, I.N., Riggs, H.R., Paczkowski, K. and Mohamed, A. (2011). Tsunami bore forces on walls. *30th International Conference on Ocean, Offshore and Arctic Engineering*, Rotterdam, the Netherlands, June 19-24, 2011.

[50] Rusche, H. (2002). Computational fluid dynamics of dispersed two-phase flows at high phase fractions. *PhD thesis, Imperial College*, London, UK.

[51] Sadeque. M. A. F., Rajaratnam. N., and Loewen. M. R. (2008). Flow around Cylinders in Open Channels. *ASCE J. Eng. Mech.*, (08), 134(1): 60-71.

[52] Shafiei, S., Melville, B. W., Shamseldin, A. Y., (2016). Experimental investigation of tsunami bore impact force and pressure on a square prism. *Coastal Engineering* 110, 1-16.

[53] Shih, T.-H., Zhu, J., and Lumley, J. L., (1994). A new Reynolds stress algebraic equation model. NASA. TM.

[54] Shih, T.H., Liou, W.W., Shabbir, A., Yang, Z.,and J. Zhu. (1995). A new $k-\epsilon$ eddy viscosity model for high Reynolds number turbulent flows - Model development and validation. *Computers Fluids*, 24(3), 227-238.

[55] Sohankar. A. (2008). Large eddy simulation of flow past rectangular-section cylinders: Side ratio effects. *J. Wind Eng. Ind. Aerodyn.* 96 (08) 640–655.

[56] St-Germain, P. (2012). Numerical modeling of tsunami-induced hydrodynamic forces on free-standing structures using the SPH method. *M.A.Sc. thesis, University of Ottawa*, Ottawa, Canada.

[57] St-Germain P, Nistor I, Townsend R (2012) Numerical modeling of the impact with structures of tsunami bores propagating on dry and beds using the SPH method. *International Journal of Protective Structures* 3(2), 221–255.

[58] St-Germain, P., Nistor, I., Townsend, R., and Shibayama, T. (2014). Smoothed particle hydrodynamics numerical modeling of structures impacted by tsunami bores. *J. Waterway, Port, Coastal, Ocean Eng.*, 140 (1), 66-81.

[59] Stansby, P. K., Chegini, A., and Barnes, T. C. D.(1998). The initial stages of dam break flow. *J. Fluid Mech.*, 374, 407–424

[60] Stoker, J. J.(1957). Water waves: The mathematical theory with applications, *Wiley-Interscience*, New York.

[61] Synolakis, C. E., (1987). The runup of solitary waves, *J. Fluid Mech.*, 185, 523 – 545.

[62] Tian. X.,Ong. M.K., Yang. J., Myrhaug. D.,(2013) Unsteady RANS simulations of flow around rectangular cylinders with different aspect ratios. *Ocean Engineering* 58 (13) 208–216.

[63] Vengatesan. V., Varyani K. S., Barltrop N.(2000). An experimental investigation of hydrodynamic coefficients for a vertical truncated rectangular cylinder due to regular and random waves. *Ocean Engineering*, 27(2000), 291–313.

[64] Wei, Z., Dalrymple, R. A., Hérault, A., Bilotta, G., Rustico, E. and Yeh, H. (2015). SPH modeling of dynamic impact of tsunami bore on bridge piers. *J. Coastal Eng.* 104, 26–42.

[65] Weller, H.G. (2008). A new approach to VOF-based interface capturing methods for incompressible and compressible flow. *Technical Report TR/HGW/04*, OpenCFD Ltd., 2008.

[66] Wilcox, D.C. (1988). Re-assessment of the scale-determining equation for advanced turbulence models. *AIAA Journal*, 26(11), 1299-1310.

[67] Yakhot, V., Orszag, S.A., Thangam, S., Gatski,T.B. and Speziale, C.G. (1991). Development of turbulence models for shear flows by a double expansion technique. *Physics of Fluids A*, 4(7), 1510-1520.

[68] Yeh, H., Sato, S. and Tajima., Y. (2013). The 11 March 2011 East Japan Earthquake and Tsunami: Tsunami Effects on Coastal Infrastructure and Buildings. *Pure Appl. Geophys*., 170, 1019-1031.

[69] Yeh, H. (2006). Maximum Fluid Forces in the Tsunami Runup Zone. *Journal of Waterway*, Port, Coastal, and Ocean Engineering, 132(6), 496-500.

[70] Yeh, H. (2007). Design tsunami forces for onshore structures. *Journal of Disaster Research*, 2(6), 531-536.

[71] Yeh, H., Francis, M., Peterson, C., Katada, T., Latha, G., Chadha, R.K., Singh, J.P., Rahghuraman, G., (2007). Effects of the 2004 Great Sumatra Tsunami: Southeast Indian Coast. *Journal of Waterway, Port, Coastal, and Ocean Engineering*, 133, pp. 382-400.

[72] Yu G., Avital E. J., and Williams J. J. R. (2008). Large Eddy Simulation of Flow Past Free Surface Piercing Circular Cylinders. *ASME J Fluids Eng Trans* , 130, 10, pp. 41-49.